SYNTHESIS AND APPLICATION OF IONIC MOLECULAR AND POLYMERIC MATERIALS

BY

KE YANG

DISSERTATION

Submitted in partial fulfillment of requirements
for the degree of Doctor of Philosophy in Materials Science and Engineering
in the Graduate College of the
University of Illinois at Urbana-Champaign, 2016

Urbana, Illinois

Doctoral Committee:

Professor Jeffrey S. Moore, Chair
Professor Kenneth S. Schweizer
Assistant Professor Yang Zhang
Assistant Professor Qian Chen
Assistant Professor Kristopher A. Kilian

ABSTRACT

Materials are built from atoms and molecules through different interactions. Few artificial material is built primarily with ionic interaction despite its ubiquitous existence in living systems. My research has focused on filling this void by developing novel ionic molecular and polymeric materials for both fundamental understandings of the systems and various applications such as self-healing. With one theme of ionic functional materials, my research has broadly evolved into three areas: Chapters 2-3 focus on the development of structure-property relationship of network-forming ionic glasses and liquids; Chapter 4 focus on the application of network-forming ionic liquids for the cause of shockwave absorption; Chapter 5 extends the exploration into the realm of polymeric ionic rubber and its application as self-healing materials.

The network-forming ionic glass is a stable glassy organic network that is primarily connected by ionic interaction. It was found that the glass transition temperature of ionic glass series with increasing alkyl backbone length showed an intriguing odd-even effect. The mechanism was revealed by inelastic neutron scattering as different dynamics of odd- and even-numbered cations in liquid state. Structurally, thanks to the nano-segregation, the network-forming ionic liquid proved to be an excellent shockwave absorption material. Further investigation indicated that a shock-induced ordering in network-forming ionic liquids contributed to its overall shockwave absorption performance. Similar to the small molecule ionic glass and liquids, an oligomeric anion, a carboxylate-terminated copolymer of polybutadiene(PBD) and polyacrylonitrile(PAN), was chosen as the counterion for multivalent cations to build a polymeric amorphous ionic network. An ionic rubber that combines competitive mechanical properties and full reprocessibiltiy was successfully prepared where ionic interaction plays the key role of the dynamic crosslink. The reversible ionic crosslink renders excellent properties including high plateau modulus, rate-dependent stress releasing and super-fast self-healing at room temperature. These studies on the ionic glass and ionic rubber have advanced the development of artificial ionic materials in the aspect of both fundamental knowledges on structure-property relationship and practical application including shockwave absorption and self-healing.

ACKNOWLEDGEMENT

I know this will be the most read part of my thesis. I have a long list of people to thank for helping me pursue my Ph.D. degree. After all, obtaining this degree is not as easy as I thought when I accepted the offer as a senior undergrad. Most importantly, it will not happen if I haven't received the help and support from the people in the list. The five years at UIUC have definitely changed my life and shaped myself into who I am now in a lot of ways.

First, I want to thank my advisor, Prof. Jeff Moore, for taking me in his group and cultivating me with his advising philosophy. Even though I did not realize this at first, eventually I come to this conclusion that he is the best advisor in the world. I appreciate all his advice to me, whether it is about research, work or life. He is critical in the world of science but supportive for his students. We have a lot of stories with our individual meetings such as Jeff's brother's mushroom farm, Jeff's mandatory working hours during his graduate time by his wife, and so on. Jeff always wants me to figure out the question by myself even though he may know the answer (or not), and I have to admit that helps me a lot not only in academia but also in life. Likewise, I would like to thank my coadvisor, Prof. Yang Zhang for his support along the way. We started as collaborators on the project of ionic glass. I really admired his intelligence and diligence as a scientist. I cherished the time when we drove to national labs to do neutron scattering experiments and chatted along the way. I am really glad to hear that the proposal we wrote together got funded.

I would also like to thank my prelim and thesis committee, Prof. Ken Schweizer, Prof. Qian Chen, Prof. Kris Kilian, Prof. Paul Braun, and Prof. Nancy Sottos. We had a lot of fruitful discussions during subgroup meetings and my prelim test. I have taken classes from them as a student and taken great suggestions from them as a young researcher. They really made me feel choosing UIUC as my graduate school is a great choice.

As an AMS group member, I would like to thank Prof. Nancy Sottos and Prof. Scott White. They are amazing scientists and engineers. I learned a lot from them during AMS group meetings. They gave me guidance on my research both directly and indirectly.

instruments to every screw. Thanks to the Zhang group member: Abhishek Jaiswal, Zhikun Cai, and Nathan Walter. We did several national lab experiments together and had a lot of fun.

Thank you to my undergraduates: Isac Lim, Andrew Chancellor, Yangyang Zhou, Aileen Nolan and Matthew Wong. You are great people to work with and I have also learned a lot from you as your mentor. I am very proud of everything you have accomplished during your time in Moore group and I wish you the very best in your future career.

The life in Champaign-Urbana becomes colorful with all my friends. We went out eating, playing sports, partying, and traveling together. We shared our memory in UIUC and became lifetime friends. Thank you for all your company and encouragement: Junjie Wang, Sichao Ma, Helin Zhu, Lu Xu, Yifei Meng, Kanuo Chen, Weili Chen, Zihe Gao, Liang Ma, Dr. Sen Kang, Dr. Chunjie Zhang, Jie Zhang, Dr. Sizhu You, Dr. Zhi Su and Mian Duan.

I want to thank my family, especially to my mom and dad. You always give me the best of everything. Your love and support make me who I am today. I know you are always proud of me.

Finally, I would like to thank my wife, Ruiwen Sun. You are the best thing that ever happened to me. We've attended the same high school, same university, and same graduate school. Whenever I am happy or sad, you are always by my side and support me without any condition. You have the courage to start your new career in order to solve our two-body problem. You have a beautiful heart to help other people as a social worker. I cherish every memory we have together. I am looking forward to exploring the rest of my life with you by my side. I love you.

TABLE OF CONTENTS

CHAPTER 1

IONIC MOLECULAR/POLYMERIC MATERIALS: AN OVERVIEW

1.1 Ionic interaction

Why do molecules bond with each other? How do they form a macroscopic piece of materials? These are the questions we ask when we first learned about chemistry. According to a common classification, chemical bond includes covalent bond, ionic bond, and metallic bond. The covalent bond is a shared-electron-pair bond, ionic bond is a definite electrostatic bond, and metallic bond is a fractional bond. [1,2] Besides primary interactions, secondary interactions refer to relatively weaker attractions between nearby atoms or molecules such as ion-dipole attractions or dipole-dipole attractions. As a brief summary of different bonds in materials, table 1.1 shows the typical bond energy of each bond type. The melting point of the formed material and directionality of the bond is also provided as a reference. The bond energy of ionic interaction is very versatile: it can be as strong as a primary interaction as in the case of ionic crystals while it can be also as weak as a secondary interaction as in the case of the salt bridge in proteins.[3,4] It's also very tunable depends on the actual condition and environment: the distance between the ions, the size of the ions, the solvent, pH value and so on. All these properties make ionic interaction a very unique and motivate us to explore the possibility to use it in novel artificial materials.

Table 1.1 Chemical bonds and some secondary bonds.

Material bonding	Bond Energy (kcal/mol)	Melting Point	Directionality
Covalent bonds	30-170	Variable	Directional
Metallic bonds	27-83	Low to high	Non-directional
Ionic bonds	10-250	Very high	Non-directional
Hydrogen bonds	1-12	Low to moderate	Directional
van der Waals	1-10	Low to moderate	Directional

Calculating the ionic interaction strength renders the possibilities to predict the properties of novel ionic materials. The ionic interaction strength has intrinsic relation with most of their physicochemical properties such as melting point, density, vapor pressure and viscosity. For ionic crystals, the calculation is simply by calculating the lattice energy, U, which equals to the energy (dissociation heat) to separate one mole of ionic crystal into cations and anions. [5]

$$U = A\frac{Ne^2\eta_1\eta_2}{r}\left(1 - \frac{1}{m}\right) \qquad (1.1)$$

where η_1, η_2, and e are the ionic and electronic charges, r is the distance between ions, m is electronic shells repulsion exponent, N is Avogadro constant, and A is the Madelung constant.

For complex ionic systems such as ionic liquids, in principle, the evaluation of cation-anion interaction strength is very straightforward. Ab initio and density functional theory based quantum chemical calculations can be applied to compute the binding energies of cations and anions. [6] Examples of several common

Table 1.2 BSSE uncorrected and corrected dissociation energies for the ionic species [cation][anion], [(cation)2anion]$^+$, and [(anion)2cation]$^-$,calculated at the B3LYP/6-31+G(d) level of theory.(Reproduced with permission from Reference [6]. Copyright © 2011 American Chemical Society)

Ionic liquids	E_{diss} /kJ·mol^{-1}	E_{diss}(BSSE) /kJ·mol^{-1}
[C$_4$mim]Cl	372	371
[C$_4$mim][BF$_4$]	341	341
[C$_4$mim][PF$_6$]	320	316
[C$_4$mim][TfO]	334	330
[C$_4$mim][NTf$_2$]	313	305
[C$_4$C$_1$mim][NTf$_2$]	293	285

1.2 Examples of ionic interactions in living system

Most artificial materials we use especially structural materials are built from covalent bonds and metallic bonds. [7] Ionic solids are often referred as salts. Because of

their brittle nature and low resistance to polar solvents such as water, they are rarely used as a material but rather in the form of ions/electrolyte in solution.

Despite rare application in artificial materials, ionic bond is one of the most common interactions in biological systems. Its ubiquitous existence is because of its reversibility and versatile bond energy compared with other supramolecular forces. [8] For example, it has been shown that salt bridges play an important role in stabilizing proteins or limiting the number of allowable conformation in protein. [3,9] As shown in Figure 1.1, The $\Delta\Delta G_{assoc}$ (in the order of 75 kcal/mol) is the full association energy of the ionic interaction in protein chains. However, the role that salt bridge play in stabilizing protein structure is $\Delta\Delta G_{bridge}$. Most salt bridges have the stabilization energy roughly in the range of 2-10 kcal/mol.
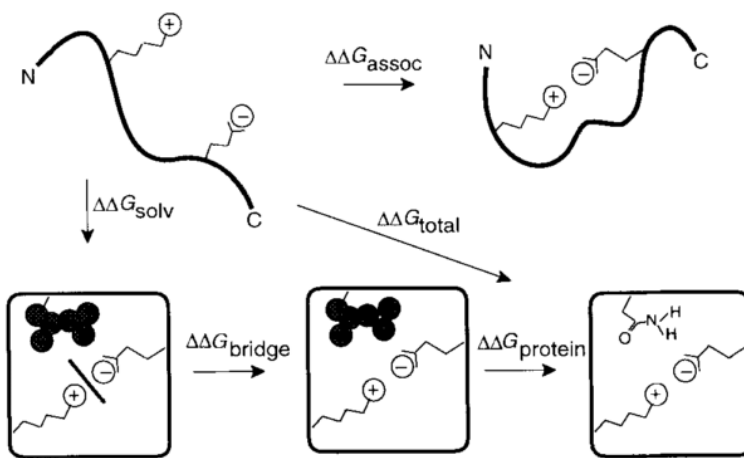
Figure 1.1 Thermodynamic cycle used to analyze salt bridges. The unfolded protein and folded protein is in the upper left and right. Lower left is folded molecule where partial charges and polar groups are turned off. In lower center, the charged side chains is restored. In the lower right, the interaction with other c charged and polar groups are also restored. (Reproduced with permission from Reference [9]. Copyright © 1994 The Protein Society)

Ionic interaction also plays a role in structural materials in the living system. It was found that in the organic matrix of bone, the calcium-mediated sacrificial ionic bonds increased the stiffness and enhanced energy dissipation. [10,11] A non-fibrillar organic matrix acts as a glue that holds the mineralized fibrils together. The multivalent calcium cations form an ionic interaction with anionic polymeric chains in the matrix. It acts like ionic crosslink between polymer chains or within different sites on one polymer chain. Upon

damage, the sacrificial ionic bonds are going to be broken first. The hidden lengths which are a result of crosslink and entanglement are going to be release first to dissipate the damage. It was also shown that the sacrificial ionic bonds increase the stiffness and toughness of bone at the same time.
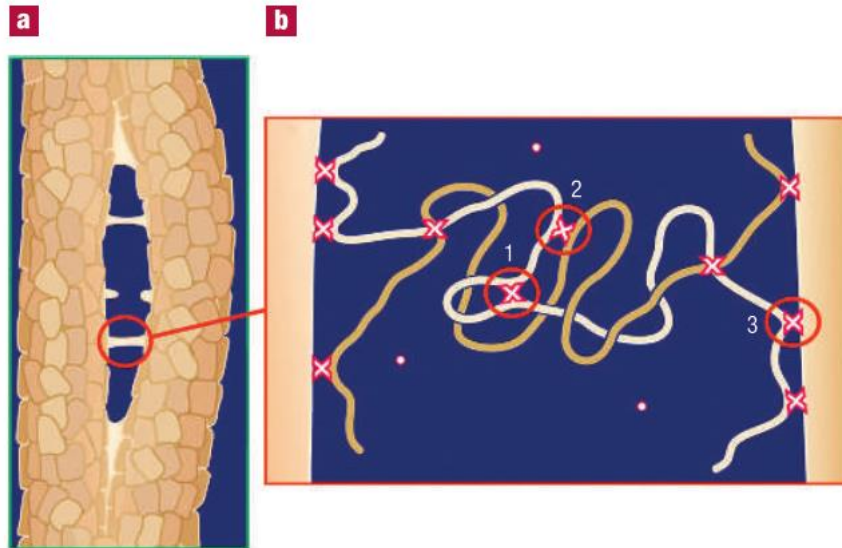
Figure 1.2 Possible kinds of sacrificial bonds involved in the glue between the mineralized collagen fibrils. (a),Glue filaments could resist the separation of mineralized fibrils. (b), The suspected, calcium-mediated sacrificial bonds in the bone could formbetween (1) two binding regions on one polymer, (2) two polymers or (3) a polymer and amineral plate or acombination of these. For all cases the sacrificial bond might involvemultipleweak bonds in parallel.(Reproduced with permission from Reference [8]. Copyright © 2005 Nature Publishing)

The ionic interaction strength is very sensitive to the environment such as ionic strength, pH value, solvent, and temperature. The relatively stable environment within living systems provides the precondition that ionic interaction can be widely used. As mentioned at the beginning of this section, ionic interaction is rarely used in artificial materials. Nevertheless, the evidence that ionic interaction plays an important role in the structural material is very encouraging for the design of artificial ionic materials.

1.3 Ionic molecular glass: combination of ionic liquids and molecular glass

Ionic molecular materials refer to organic molecules that are primarily bound by ionic interaction. Obviously, the most famous and explored ionic molecular materials are ionic liquids. The definition of ionic liquids is ambiguous to some extent. Usually, people refer ionic liquids as "organic salts with a melting temperature below 100 °C". [12,13] However, as the library of ionic liquids extends dramatically, the "100°C" in definition extends to other arbitrary temperature. For example, room temperature ionic liquids refer to organic salts that are in their liquid state at room temperature. [13] The field of ionic liquid expands dramatically because its application in green solvents, catalysts, electrolytes and pharmaceuticals. [14]

By definition, ionic liquids are molten salts. However, once they are cooled down, many of the ionic liquids form semi-crystal instead of complete crystalline. The direct reflection is in their differential scanning calorimetry (DSC) scans, a glass transition exists.[15] This is because of the structural frustration in the ionic liquid molecules. In glassy state, the ionic liquid or ionic glass in a more accurate definition has a similar property to a molecular glass, which possesses pretty high modulus (around GPa).[16] Compared with inorganic ionic glass, they are much less brittle. [17] They are good candidates for practical applications if their glass transition temperature can be higher than room temperature. However, in the literature, these ionic liquids usually have pretty low T_g which is well below 0 °C. [16,18–21]

Multivalence is another important issue that limits the mechanical property and glass transition temperature in ionic liquids. Because most ionic liquids research actually focuses on lowering the viscosity of ionic liquid for application in solvent and electrolyte. [22–25] As a result, multivalence has been avoided in the area of ionic liquids. Nevertheless, for the better mechanical property at room temperature and higher glass transition temperature, the higher valance is favored. Grinstaff et al. showed that with diphosphonium cations and EDTA anions, the ionic network has much higher viscosities with the non-charged network or monovalent ionic liquids. In addition, free-standing ionic network is obtained by using diphosphonium cation with multivalent para-tetracarboxy-5,10,15,20-

tetraphenyl-21H,23H-porphine anion. (Figure 1.3) The similar supramolecular ionic network has also been reported by Aboudazadeh et al. using dications and citrate. [26]
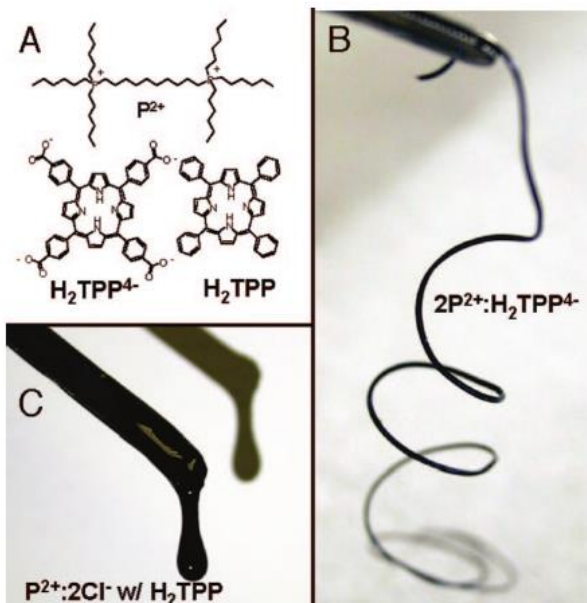
Another important issue is that because the structural frustration in these ionic liquids is usually limited, the glass is not very stable and will slowly go through cold crystallization process to form crystal or semi-crystal over time, which affects their mechanical properties.[16,27] Here we turn to the area of organic molecular glass for more stable ionic glass. The organic molecular glass is a class of organic molecules which do not crystallize readily upon cooling. There are several structure design principles for the organic molecular glass to avoid crystallization including nonpolar molecules structures, bulky heavy substituents, and large molecule size.[28] Figure 1.4 shows the typical structure of two molecular glasses which includes heavy pendant group, non-planar structure, and pretty large molecular size.[29] Incorporating these design principles, we aimed to frustrate any crystallization which may result in inhomogeneity in materials, leading to disruption of network and compromise of strength.

Combining glass-forming ionic liquid, the importance of multivalence in the supramolecular ionic network and organic molecular glass, we aim to synthesize a new material that we named network-forming ionic glass. The definition for network-forming ionic glass is a stable glassy organic network that is primarily connected by ionic interaction. The key elements in network-forming ionic glass is: 1) the material is a stable glass which is ensured by excessive structural frustration; 2) the ionic network is connected only by ionic interaction, which is another way of saying the network is composed of cations and anions; 3) in order to form the network, the cation and anion need to be multivalent, which means the valence/functionality/number of charges of cation/anion needs to be larger than two and the counterion's functionality needs to be larger than three.
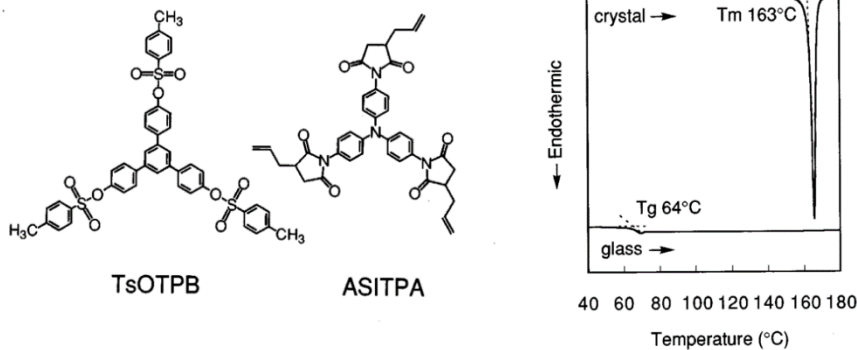
The network-forming ionic glass can also be considered as a counterpart to conventional thermosets, which is a heavily crosslinked network formed by covalent bonds. Instead, ionic glass is a reversible network primarily with ionic crosslinks, combining both strength and adaptivity. Building the structure-property relationship of ionically-connected material is beneficial for the development of new generation of functional materials such as self-healing materials[30] and malleable thermoset[31].

1.4 Ionic polymeric materials
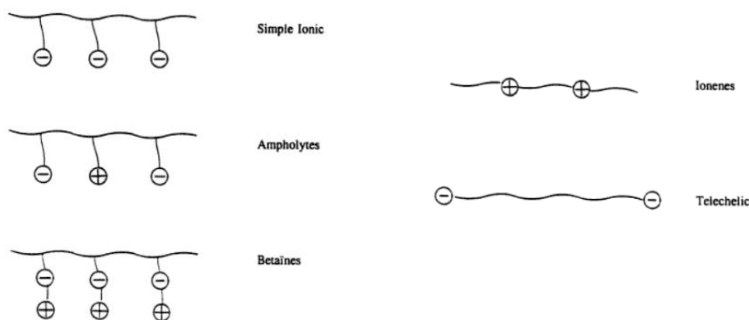
As mentioned earlier in section 1.2, nature has attributed a critical role to ionic interaction in living systems mostly in the form of ionic biopolymers. Ionic polymer is the artificial version of these ionic biopolymers. Depending on the actual classification, ionic polymeric materials have different percentages of the ionic moiety. For example, ionenes are polymers with ionic repeating units in the backbone. Polyelectrolytes usually refer to polymers where the ionic groups are covalently bonded to the polymer backbone and the ionic groups' mole substation level is usually larger than 80% (high ionic content). While ionomers refer to the similar polymers with ionic pendant groups with less than 15 mole percent of ionic content. Ionic polymers can also be categorized based on the type of charges they carry. (Figure 1.5)[32]

The effect of ions on the structure-morphology-property relations is one of the most significant and well-studied aspects of ionic polymers. There are several models that describe morphology of ionomers. One of the most popular model, the so-called Eisenberg-Hird-Moore (EHM) model is based on ionic aggregate. Basically, there are primary ionic aggregates that are consist of several ion pairs in ionic polymers. The size of the aggregate is affected by the dielectric constant of the polymer backbone. The chain mobility is constrained by the ionic aggregates.[33]

For ionic polymers, the existence of ionic moiety strongly affects the properties of the polymers. The effect of ionic interaction is quite different depending on the states of the materials. With respect to the viscoelastic properties of ionic polymers in their glassy

state, the presence of ionic groups does not result in major changes. However, in rubbery plateau regime, the properties can be vastly different from non-ionic polymer because of the extra physical crosslink from the ionic interaction. In the melts flow region, with the weakening of ionic interaction, the viscoelastic property of ionic polymer resembles that of thermoplastic thus provide great reprocessibility compared with covalently crosslinked rubber. [34]
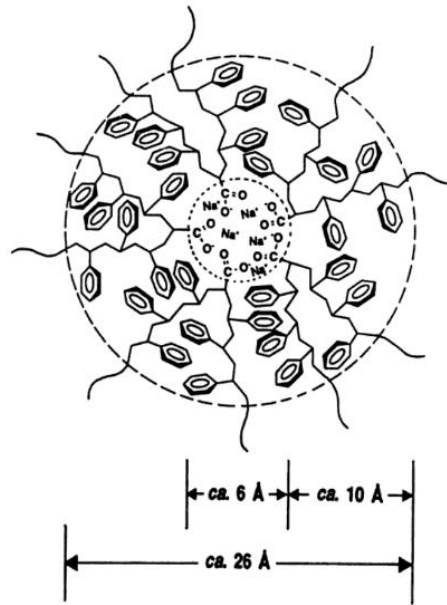
Based on their morphology and properties at different states, ionic polymers have been widely used in industry. The most significant applications include packaging, films, ion-conductive membranes, adhesives, fluid additives, and coatings. [32]

1.5 Current application of ionic interaction in self-healing materials

The state-of-the-art high-performance self-healing materials are composites reinforced with microcapsules or microvascular that contain healing agents.[35] (Figure 1.7) Thanks to the combined excellent mechanical property and self-healing capability, the self-

a Capsule based   **b** Vascular   **c** Intrinsic
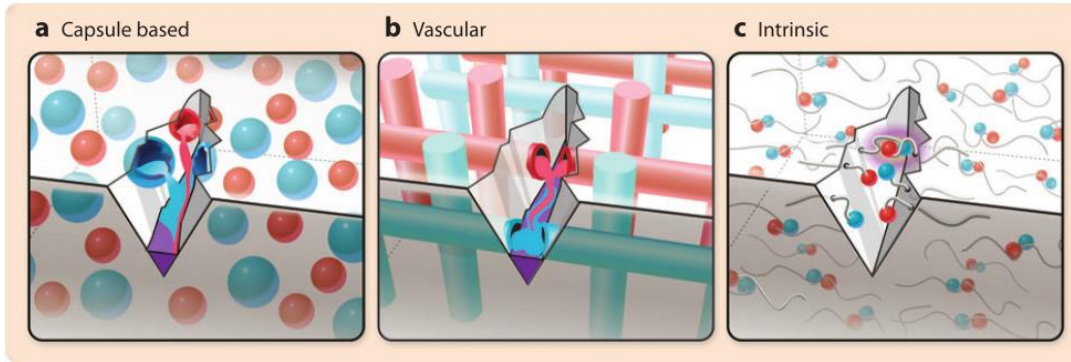
healing composites can maintain strength and toughness until achieving limited healing cycles that the healing agents can last. Today, advanced engineering applications require a new generation of self-healing materials with integrations of more traits, such as response to the constantly changing environment, autonomous sensing, and most important of all, multiple healing cycles that can significantly extend service life. Intrinsic self-healing materials that based on supramolecular interaction have been demonstrated to possess much more healing cycles than composite-based systems.[36,37]

Intrinsic self-healing polymer replies on the reversibility of secondary interaction. Compared with other supramolecular forces, ionic interaction is unique because of its versatile bond energy, adjustable strength, and specific response to environment. [38,39] Thus, depending on the actual ionic interaction configuration, the properties of the ionic material can cover a wide application spectrum.

Compared to H-bond based supramolecular self-healing polymer, the exposure of ionic interactions in literature isn't quite as high.[40] Nevertheless, there are still some examples in literature. For example, there are reports of utilizing ionomer in the ballistic self-healing application. Usually, an ionomer was subject to a ballistic test. The healing process actually occurred via an elastic rebound followed by a friction-induced thermal melt process. A thermoplastic poly(ethylene-co-methacrylic acid) (EMAA) copolymer is a typical ionomer for this study. It was discovered that ionic content is critical for the successful healing of the sample: too low ionic content lead to lacking sufficient strength around the puncture site while too high ionic content hinders the polymer mobility and thermal/elastic energy transfer. [41,42]
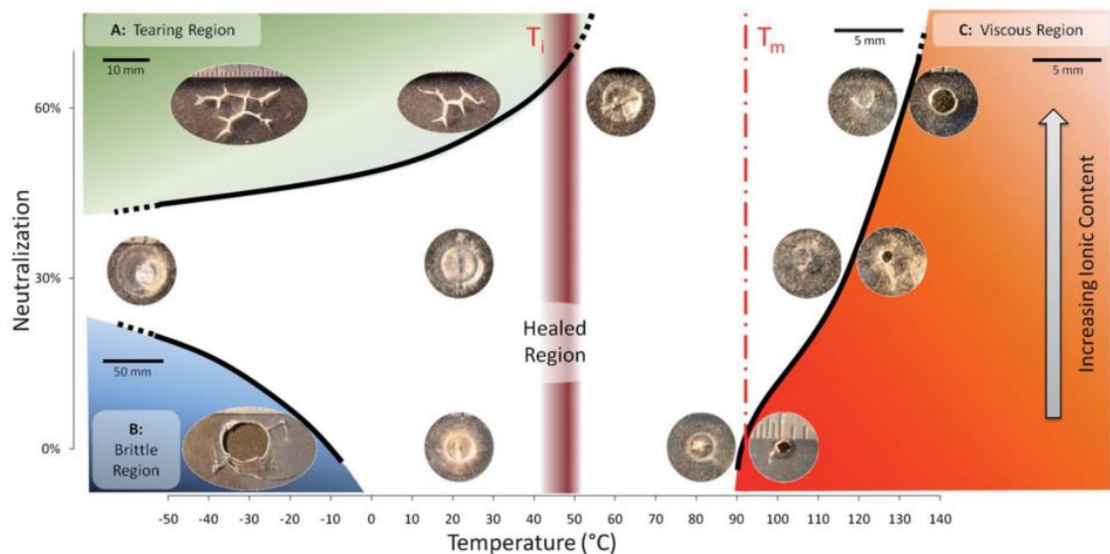
The other important category of ionic self-healing material is self-healing gel. These materials have great self-healing dynamics thanks to the existence of solvent or low glass transition temperature of the matrix. However, they also tend to be weak in modulus thus not suitable for the structural material. Aboudazdeh et al. showed that with neutralization of (di-/ tri-)carboxylic acids and (di-/tri-)alkyl amines, weakly bonded supramolecular polymers behave similarly to a gel-like polymer with a modulus of 10MPa in its solid state. The crossover temperature of G' and G'' can be tuned between 30 and 80 °C using a different combination of carboxylic acids and alkyl amines. [43] Wei et al. utilized the ionic interaction between poly(acrylic acid) (PAA) and ferric ions to synthesize

a self-healing ionic gel. The gel is pretty weak in modulus (10kPa) but has fast dynamics to self-heal at room temperature. [44] To overcome the weakness of poor mechanical property, attempts have been made by making tough double network hydrogels with ionic interaction. Henderson et al. shown that by ionically crosslinking PMMA backbone with solvated PMAA midblock as ending groups with divalent acetates (Zn, Ca, Ni, Co, Cu), the consequence mechanical property has been improved to up to 21 MPa.[45] Generally speaking, gel-like materials indicate weak mechanical properties, which greatly limited the practical application of this class of materials.

In view of the above discussion, the self-healing *via* ionic interaction relies either on the elevated temperature (in the case of ionomer ballistic test) or on the existence of extra solvents (in the case of ionic gels). Apparently, the efficient self-healing at ambient environments cannot be achieved without a reasonable fast chain dynamics. However, fast dynamics at room temperature means lower T_g, which indicates the mechanical properties will be affected. The current challenge in the ionic self-healing materials or even for other intrinsic self-healing materials is to achieve self-healing at ambient conditions for the polymeric network with high T_g or competitive mechanical performance.

1.6 References

(1)   Pauling, L. *The Nature of the Chemical Bond and the Structure of Molecules and Crystals*; Cornell University Press, 1960.

(2)   Morokuma, K. *Acc. Chem. Res.* **1977**, *10*, 294.

(3)   Xu, D.; Tsai, C. J.; Nussinov, R. *Protein Eng.* **1997**, *10*, 999–1012.

(4)   Yang, X.; Kim, J.-C. *Int. J. Pharm.* **2010**, *388*, 58–63.

(5)   Kapustinskii, A. F. *Q. Rev. Chem. Soc.* **1956**, *10*, 283–294.

(6)   Fernandes, A. M.; Rocha, M. A. A.; Freire, M. G.; Marrucho, I. M.; Coutinho, J. A. P.; Santos, L. M. N. B. F. *J. Phys. Chem. B* **2011**, *115*, 4033–4041.

(7)   Wathier, M.; Grinstaff, M. W. *J. Am. Chem. Soc.* **2008**, *130*, 9648–9649.

(8)   Fantner, G. E.; Hassenkam, T.; Kindt, J. H.; Weaver, J. C.; Birkedal, H.; Pechenik, L.; Cutroni, J. A.; Cidade, G. a G.; Stucky, G. D.; Morse, D. E.; Hansma, P. K. *Nat. Mater.* **2005**, *4*, 612–616.

(9)   Hendsch, Z. S.; Tidor, B. *Protein Sci.* **1994**, *3*, 211–226.

(10)   Fantner, G. E.; Hassenkam, T.; Kindt, J. H.; Weaver, J. C.; Birkedal, H.; Pechenik, L.; Cutroni, J. A.; Cidade, G. A. G.; Stucky, G. D.; Morse, D. E.; Hansma, P. K. *Nat. Mater.* **2005**, *4*, 612–616.

(11)   Hansma, P. K.; Fantner, G. E.; Kindt, J. H.; Thurner, P. J.; Schitter, G.; Turner, P. J.; Udwin, S. F.; Finch, M. M. *J. Musculoskelet. Neuronal Interact.* **2005**, *5*, 313–315.

(12)   Leys, J.; Wübbenhorst, M.; Preethy Menon, C.; Rajesh, R.; Thoen, J.; Glorieux, C.; Nockemann, P.; Thijs, B.; Binnemans, K.; Longuemart, S. *J. Chem. Phys.* **2008**, *128*, 064509.

(13)   Hallett, J. P.; Welton, T. *Chem. Rev.* **2011**, *111*, 3508–3576.

(14)   Ohno, H. *Bull. Chem. Soc. Jpn.* **2006**, *79*, 1665–1680.

(15)   Ramos, J. J. M.; Afonso, C. A. M.; Branco, L. C. *J. Therm. Anal. Calorim.* **2003**, *71*, 659–666.

(16)   Shamim, N.; McKenna, G. B. *J. Phys. Chem. B* **2010**, *114*, 15742–15752.

(17)   Angell, C. A. *Proc. Natl. Acad. Sci. U. S. A.* **1995**, *92*, 6675–6682.

(18)   Chhotaray, P. K.; Gardas, R. L. *J. Chem. Thermodyn.* **2014**, *72*, 117–124.

(19)   Kadoya, S.; Izutsu, K.; Yonemochi, E.; Terada, K.; Yomota, C.; Kawanishi, T. *Chem. Pharm. Bull. (Tokyo).* **2008**, *56*, 821–826.

(20)   Greaves, T. L.; Drummond, C. J. *Chem. Rev.* **2008**, *108*, 206–237.

(21)   Domańska, U. *Thermochim. Acta* **2006**, *448*, 19–30.

(22)   Martinez, L. M.; Angell, C. A. *Nature* **2001**, *410*, 663–667.

(23)   Zhang, Y.; Zhang, S.; Lu, X.; Zhou, Q.; Fan, W.; Zhang, X. *Chemistry* **2009**, *15*, 3003–3011.

(24)   Daguenet, C.; Dyson, P. J.; Krossing, I.; Oleinikova, A.; Slattery, J.; Wakai, C.; Weingärtner, H. *J. Phys. Chem. B* **2006**, *110*, 12682–12688.

(25)   Zhou, Z.-B.; Matsumoto, H.; Tatsumi, K. *Chemistry* **2005**, *11*, 752–766.

(26)   Aboudzadeh, M. A.; Muñoz, M. E.; Santamaría, A.; Fernández-Berridi, M. J.; Irusta, L.; Mecerreyes, D. *Macromolecules* **2012**, *45*, 7599–7606.

(27)   Imanari, M.; Fujii, K.; Endo, T.; Seki, H.; Tozaki, K.; Nishikawa, K. *J. Phys. Chem. B* **2012**, *116*, 3991–3997.

(28)   Shirota, Y.; Kageyama, H. *Chem. Rev.* **2007**, *107*, 953–1010.

(29)   Yoshiiwa, M.; Kageyama, H.; Shirota, Y.; Wakaya, F.; Gamo, K.; Takai, M. *Appl. Phys. Lett.* **1996**, *69*, 2605.

(30)   Varley, R. In *Self Healing Materials*; Sybrand van der Zwaag, Ed.; Springer Netherlands, 2008; pp. 95–114.

(31)   Montarnal, D.; Capelot, M.; Tournilhac, F.; Leibler, L. *Science* **2011**, *334*, 965–968.

(32)   Schlick, S. *Ionomers: Charaterization, Theory, and Applications*; CRC Press, 1996.

(33)   Eisenberg, A.; Hird, B.; Moore, R. B. *Macromolecules* **1990**, *23*, 4098–4107.

(34)   Tant, M. R.; Wilkes, G. L. *J. Macromol. Sci., Rev. Macromol. Chem. Phys.* **1988**, *C28*, 1–63.

(35)   Blaiszik, B. J.; Kramer, S. L. B.; Olugebefola, S. C.; Moore, J. S.; Sottos, N. R.; White, S. R. *Annu. Rev. Mater. Res.* **2010**, *40*, 179–211.

(36)   Cordier, P.; Tournilhac, F.; Soulié-Ziakovic, C.; Leibler, L. *Nature* **2008**, *451*, 977–980.

(37)   Hentschel, J.; Kushner, A. M.; Ziller, J.; Guan, Z. *Angew. Chem. Int. Ed. Engl.* **2012**, *51*, 10561–10565.

(38) Yang, Y.; Urban, M. W. *Chem. Soc. Rev.* **2013**, *42*, 7446–7467.

(39) Craig, S. L. *Angew. Chem. Int. Ed. Engl.* **2009**, *48*, 2645–2647.

(40) Syrett, J. A.; Becer, C. R.; Haddleton, D. M. *Polym. Chem.* **2010**, *1*, 978–987.

(41) Varley, R. In Self Healing Materials. An Alternative Approach to 20 Centuries of
      Materials Science; Springer, 2007; pp. 95–114.

(42) Kalista, S. J.; Pflug, J. R.; Varley, R. J. *Polym. Chem.* **2013**, *4*, 4910-4926.

(43) Aboudzadeh, M. A.; Muñoz, M. E.; Santamaría, A.; Marcilla, R.; Mecerreyes, D.
      Macromol. Rapid Commun. **2012**, *33*, 314–318.

(44) Wei, Z.; He, J.; Liang, T.; Oh, H.; Athas, J.; Tong, Z.; Wang, C.; Nie, Z. *Polym.
      Chem.* **2013**, *4*, 4601-4605.

(45) Henderson, K. J.; Zhou, T. C.; Otim, K. J.; Shull, K. R. *Macromolecules* **2010**, *43*,
      6193–6201.

CHAPTER 2

SYNTHESIS AND STRUCTURE-PROPERTY RELATIONSHIP OF NETWORK-FORMING IONIC GLASS

2.1 Abstract

The structure-property relationship for ionic glass is critical for rational design and preparation of functional ionic materials. Combing the two aspects of molecular glass and ionic liquids, we intend to build a stable molecular glassy network primarily connected by ionic interaction. A major advantage of ionic networks from small organic molecules is the possibility to fine-tune the macroscopic properties, such as the glass transition temperature and even the fragility, by modifying the chain lengths and molecular architecture of the building blocks. While empirical observations of the dependence of macroscopic properties on the discrete molecular structure exist for certain ionic molecular supercooled liquids and glasses, the general structure-function and the dynamics-function dualities remain unexplored. The molecular packing structure and dynamics of the random interconnected network are not known, because of the reasons stated previously. By synthesizing a series of same class ionic glass, we studied the role of minor structural variation in the determination of ionic glasses' microstructure, glass transition temperature, and mechanical properties.

2.2 Introduction

Compared with secondary bonds (H-bonding, π-π stacking etc.), the advantage of ionic interaction includes, 1) high tunability over interaction strength only by minor structure modification; 2) isotropic connection. As a counterpart to crosslinked network formed by covalent bonds, it would be worthwhile to build a reversible network primarily with ionic interaction. For this desired network which we name Crosslinking Ionic Network (CIN), building the structure-property relationship is beneficial for the development of new class of functional materials such as self-healing materials and malleable thermoset. In

addition to the potential materials application, the glasses formed primarily by ionic interaction, which we named Network-forming Ionic Glass, is rather an extension of ionic liquids into its glass regime. They are of great fundamental scientific interests, possessing the potential to solve some long standing questions about glass transition and fragility.[1–3]

In order to build the desired ionic glass, we drew on the experience of structure design principles from organic molecular glass. Organic molecular glass or amorphous molecular materials is a class of organic molecules which do not crystallize readily upon cooling.[4] These materials have been widely explored previously for various application including electrically conducting materials, resists and OLEDs.[5–8] They are readily prepared from melt sample or solution by either rapid cooling or air standing cooling. The stability of these molecular glasses depends on the designed structure. Some molecular glasses tend to crystallize on heating above T_g, with polymorphism. However, if structural frustration is large enough, it is very easy to enter the thermodynamic non-equilibrium state, and can avoid crystallization for usual processing condition even above T_g. There are several structure design principles for organic molecular glass to avoid crystallization including nonpolar molecules structures, and existence of different conformers.[4] It has been shown that the incorporation of aryl substituents into TDAB allows the formation of amorphous glasses. The reason why alkyl chain could promote glass-forming capability is that the flexibility of alkyl chain increase the possibilities of different conformers. This effect can be dramatically enlarged by employing longer alkyl chains. [9–11]

On the other hand, ionic liquids as a "molten salts", has been studied intensively over two decades. Conventionally ionic liquids (or technically room temperature ionic liquids) are organic salts with a melting temperature below 100 ℃ by definition. It was found later that some classes of ionic liquids are glass formers as well.[12,13] Many ionic liquids easily form a glass with DSC curve showing a clear signature of glass transition.[14–16] Generally speaking, ionic liquids' crystallization is hindered. So it is not uncommon that ionic liquid can exhibit glass transition together with other phase transition such as cold recrystallization and fusion.[17] However, glass forming ionic liquids often have relatively low glass transition temperature (commonly below 200K), which limits the application of

these materials in solid state. The low T_g of ionic liquids is due to weak cohesive energy, which is determined by the balance of attractive (electrostatic force) and repulsive (Pauli repulsions of outer shell electrons) contributions to the cation and anion potential. Another reason for low T_g of ionic liquids is actually due to focus of application. A lot of efforts have been devoted to lower the glass transition temperature. That is because lower viscosity is more appreciated in the application of IL as solvents.

Combining the "frustration of crystallization" architecture design principles in organic molecular glass area and various selections of ionic pairs in ionic liquids area, we built series of ionic glasses with systematically varying structure. In our study, in order to increase the density of ionic crosslink, we used small diammonium cations and citrate anions to address both the formation of network and degree of crosslink. A major advantage of building network using small organic molecules is the possibility to fine-tune the macroscopic properties by tailoring the chain lengths and molecular architecture of the building blocks. Herein we show an example of establishing the structure-property relationship by simply changing the length in either side chain or backbone of ionic glass's building block.

2.3 Structure-property relationship of di-ammonium ionic glass
2.3.1 Microstructure analysis and frustrate crystallization in di-ammonium ionic glass

Peak assignments is given to the main three peaks that are shown in Figure 2.1. Peak II and III are related to first-neighbor interactions or to intramolecular correlations. Specifically, peak II has amplitude that is smaller compared with Peak I and Peak III. Peak II shift from higher q to lower q with longer backbone chain length. In order to estimate the spatial correlation length D, which corresponds to the size of structural heterogeneities from peak positions, we use $D=2\pi/Q_{max}$ as approximation. D_{II} varies linearly with backbone alkyl chain length. For n=3, the D_{II} is in accordance with fully extended intramolecular N-N distance in cation. However, with longer backbone chain length, the two linear fitting line deviate with either other. 1) when spacer between positive charges

18
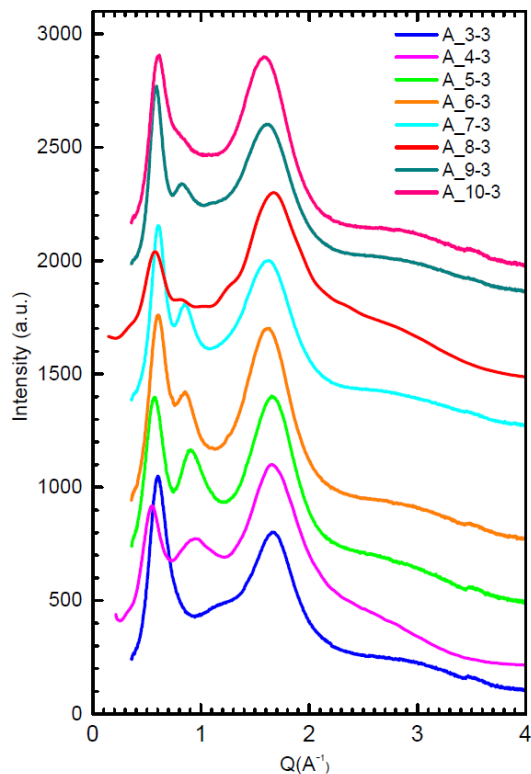
Figure 2.1 Powder XRD pattern of ionic glass A_3-3 to A_10-3. From Left to right, the three main peaks are referred as Peak I, II and III.

are short, the electrostatic force tends to extend the cation backbone; with longer chains, this effect damps quickly (2) alkyl chain's flexibility is relatively constant, so that D_{II} has good linear behavior; (3) the conformation of cation is unknown, but it is far from fully extended conformation.

On the other hand, Peak I and Peak III have relatively constant q position. Peak III has a correlation length $D_{III} \approx 3.9$ Å. Simulation on similar systems attributed this feature to intermolecular correlations between cation tail/anion pairs and anion pairs or adjacent tails.[11,18,19] It can be seen from figure 4, when comparing A_5-3 and A_5-4. Peak III shift to smaller q, which indicates larger correlation length. Indeed, butyl side chain should provide greater blocker between cation and anion.[20] Peak I has a correlation length $D_I \approx$ 10-13 Å. This peak is associated with structural heterogeneities with nanometer spatial scale and is ubiquitous in ILs.

Table 2.1 Peak position (q value) of ionic glass powder XRD and their corresponding lengths

n	Peak I(Å^{-1})	D1(Å)	Peak II(Å^{-1})	D2(Å)	Peak III(Å^{-1})	D3(Å)	D_{N-N}(Å)
3	0.601	10.4	1.176	5.3	1.662	3.8	5.3
4	0.544	11.5	0.941	6.7	1.655	3.8	6.6
5	0.571	11.0	0.908	6.9	1.653	3.8	7.8
6	0.608	10.3	0.859	7.3	1.609	3.9	9.1
7	0.609	10.3	0.857	7.3	1.619	3.9	10.3
8	0.456	13.8	0.88	7.1	1.571	4.0	11.6
9	0.589	10.7	0.827	7.6	1.605	3.9	12.9
10	0.598	10.5	0.775	8.1	1.566	4.0	14.1

Strong theoretical and experimental evidence showed that these long alkyl chains are packed into oily domains. These alkyl chain segregation has been found in various systems including Imidazolium ILs, phosphonium, ammonium. Even for very short alkyl chains, this feature exist. Because of the relative constant q value of peak I, we believe it is mainly
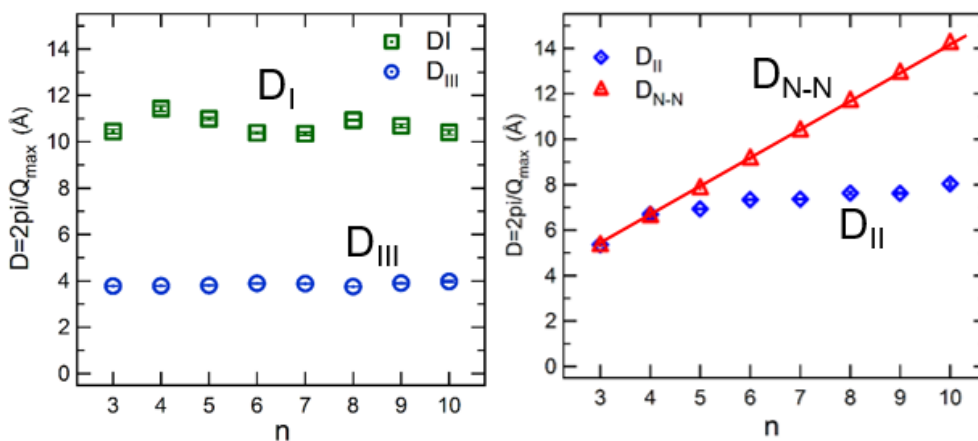
Figure 2.2 Left: Corresponding length for Peak II D_{II} and theoretical fully extended backbone length D_{N-N} as function of backbone length n. Right: Corresponding length for Peak I D_I and Peak III D_{III} as function of backbone length n.

contributed by side chains of the ionic glass. Another evidence is that A_5-4 again has a quite noticeable change.

Backbone chains are greatly affected by charged polar head. Unlike side chains with one free tail, both ends of backbone alkyl chain are connected to charged polar head, intermolecular "packing" of these alkyl chains are greatly inhibited. As a consequence, for short backbones, because of strong electrostatic repulsion, alkyl chain is fully extended. For longer backbones, the electrostatic repulsion solvophobically repel alkyl backbone into a high degree of curvature.

Backbone in cations affects glass transition temperature greatly. Previously, an odd-even effect of glass transition temperature as a function of backbone chain length has been reported by out group. It is very intriguing that, without periodic packing, how the difference between odd-number and even-number cations is manifested into alternation of macroscopic property. It has been argued that the structural heterogeneity may cause dynamic heterogeneity in ionic liquids. It is currently under investigation whether the glass transition temperature difference between odd-number and even-number ionic glass is caused by either heterogeneity.
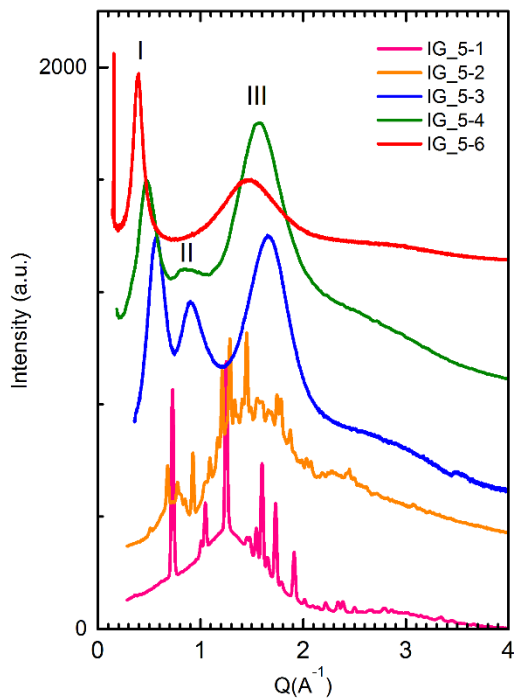
Figure 2.3 Powder XRD pattern of ionic glass A_3-3 to A_10-3. The major peaks are marked.

One big advantage of ionic glass is the tunability of ionic interaction strength. Given the certain type of ionic interaction (same charge distribution and size), the strength depends on the distance between cation and anion. We are able to tune the strength of ionic interaction easily by extending or shortening the steric hindrance between charges. In the simplest case, we can easily tune ionic glass's crystallinity by adjusting the side chain length. As shown in figure 2.4, the ionic materials consist of diammonium cation and citrate anion. When varying the side chain length from methyl to butyl, the crystallinity decreases till fully amorphous phase. In the case of diammonium cation, propyl side chain is enough to frustrate all crystallization.

From XRD results, we've shown Peak I and Peak III are mainly correlated with side chains. Peak I is a common feature in ionic liquids. In various system, structural heterogeneity exists over domains of around 1 nm. This nanostructure is the result of nanoscale phase separation between charged polar heads and uncharged alkyl chains. These polar and nonpolar domains percolate through the liquid phase and form sponge-like structure. The position of Peak I is strongly affected by side chain length as can be seen in Figure 2.4. Comparing A 5-4 with A 5-3, longer side chains result in considerable shift of Peak I position towards lower q, indicating larger nanoscale structure. To our surprise, Peak I position is independent of backbone length. This means in the diammonium ionic glass system, the nanoscale "oily" domains are mainly constructed by the alkyl side chains other than alkyl backbone.

As mentioned previously, the alkyl side chains around N atom is designed to introduce frustration into the molecule structure. Because of the great flexibility of alkyl chain, great number of conformers with similar conformational energy is possible. When the cations and anions are packed, numerous choices of packing result in frustration of crystallization. There are two aspects that longer side chains can promote glass-forming capability. Firstly, with longer alkyl chain, there are much more potential conformers, which means these structure frustration is more populated in the system. Second, strong intermolecular interaction promote local crystallization because it results in more aligned packing and reduces the number of conformers. Side chains adjust ionic interaction

strength, which controls distance between charge center in cation (in this case, N atom) and anion (O atom). In this sense, when ionic interaction is weaker, materials are harder to crystallize. This is also true in ionic liquids, where ionic liquids containing pyridinium or imidazolium cations are better glass-formers because of delocalization of charge.

2.3.2. Thermal properties of di-ammonium ionic glass

The heat flow jump shown in Fig. 1 is the calorimetric fingerprint of the glass transition in network-forming ionic glass. In literature, glass transition temperature has been reported by using extrapolated onset temperature (more in earlier literature) or the endothermic shift temperature at half-height. Here we used the latter method. It is not uncommon that ionic liquids exhibit a glass transition, especially for pyridinium/imidazolium- type ionic liquids with delocalized charge. Compared with those
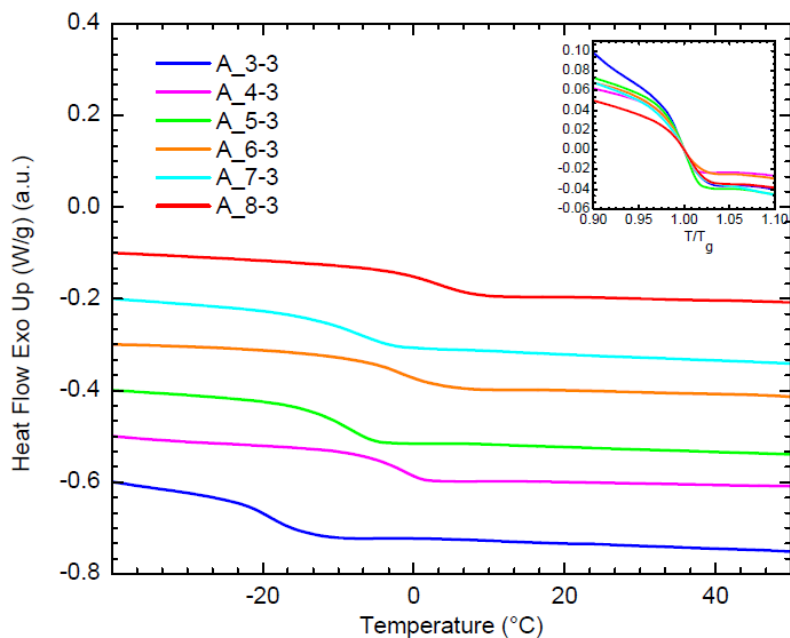
Figure 2.4 DSC curve of ionic glass A_3-3 to A_8-3. Insert shows enlarged view of DSC heat flow curve near glass transition temperature with normalized temperature axis as T/T_g

glass-forming ionic liquids, ionic glass doesn't have other thermodynamic phase transition such as cold recrystallization and fusion because of completely frustrated crystallization at practical cooling speed. In addition, glass transition temperature is higher compared with ionic liquids with same ion pair type thanks to the formation of network. It is well-known

that enthalpy relaxation is quite common in glass-forming materials depending on the cooling process prior to heating. However, such overshoot peak in the heat capacity is barely seen in ionic glass. This indicates at experimental cooling rate (10K/min), mobility of molecules is low, structural relaxation is greatly limited in these network-forming ionic glasses. This is due to the heavy crosslink density in the ionic network. Usually the glass transition spans a range of 7-10 K determined by the extrapolated onset and end from DSC curve.

Table 2.2 Glass transition, transition range, ΔCp and calculated molecular weight

Sample	T_g, K	ΔT, K	$\Delta C_p(T_g)$, $J \cdot K^{-1} \cdot g^{-1}$	$\Delta C_p(T_g)$, $J \cdot K^{-1} \cdot mol^{-1}$	M, g/mol
A_3-3	255.21	6.96	0.40	181.81	454.53
A_4-3	270.71	7.21	0.36	168.68	468.55
A_5-3	263.85	8.00	0.44	212.41	482.75
A_6-3	271.74	9.09	0.36	178.84	496.77
A_7-3	265.45	10.10	0.38	194.10	510.79
A_8-3	275.05	9.86	0.33	173.19	524.81
A_9-3	273.27	9.87	0.35	188.59	538.83
A_10-3	251.85	10.86	0.33	182.44	552.85

As seen in Figure 2.3, the glass transition temperature of all diammonium citrate ionic glasses ranges from -19 °C to 2 °C. Our group has previously reported an odd-even effect of glass transition temperatures in these ionic glasses with different spacer length. We found that the ionic glasses with even-number methylene units in cations have slightly higher glass transition temperatures than odd-numbered ones. This phenomenon has been explained by comparing their atomic-level mobility: the odd-numbered cations have been found to be more mobile than the even-numbered ones. Here we found that the ΔC_p for the same series also seem to has an odd-even effect. The ΔC_p of odd-numbered ionic glass is consistently larger than that of even-numbered ones. This can be also explained by the odd-even mobility difference. ΔC_p of glass transition reflects particle's entropy lost from mobile

liquid state to frozen glassy state. The odd-numbered species with higher mobility will lose more entropy during glass transition.

We also listed ΔC_p with different units for easier comparison with other glass forming systems. For $\Delta C_p(T_g)$ with unit $J \cdot K^{-1} \cdot g^{-1}$, it is directly calculated by DSC heat flow curve. The $\Delta C_p(T_g)$, $J \cdot K^{-1} \cdot mol^{-1}$ is otherwise calculated by molecular weight of ionic glasses. However, because in network-forming ionic glass, it is hard to define such a molecular unit, we use [(diammonium cation)$_1$ (citrate)$_{2/3}$] as the unit for calculating molecular weight and thus $\Delta C_p(T_g)$, $J \cdot K^{-1} \cdot mol^{-1}$.

Anion exchange method is used to combine the cation and anion into final ionic glass. It is fairly easy to replace the anion with other carboxylic acids or other acids as long
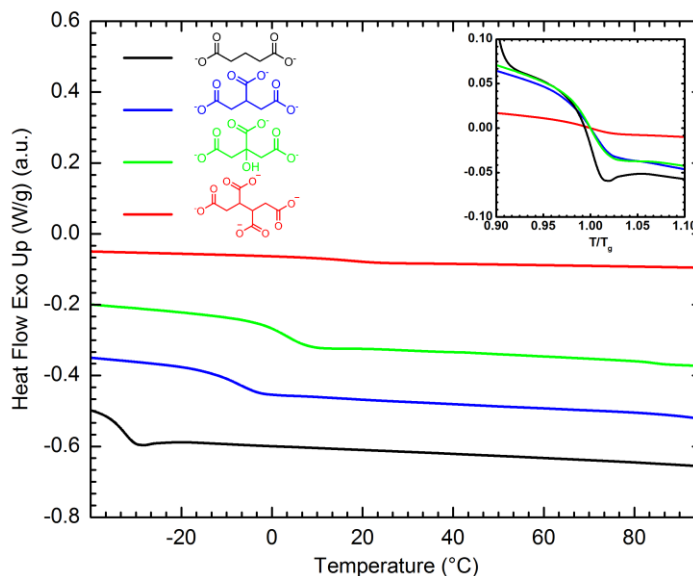
Figure 2.5 DSC curve of ionic glass A_8-3 with different anions. Insert shows enlarged view of DSC heat flow curve near glass transition temperature with normalized temperature axis as T/T$_g$

as the intermediate hydroxide salt is stable. Therefore, it is recommended that for ammonium hydroxide, the eluent from anion exchange column should be protected with inert atmosphere and low temperature to avoid the reaction with acidic gases in air and Hofmann elimination. To ensure the efficiency of the acid-base neutralization, there is certain requirement for the pKa value of the organic acids. While practically, the

25

neutralization reaction happens in methanol with very small amount of water, most carboxylic acids can react with ammonium hydroxide with almost 100% conversion rate.

One of the key features of ionic glass is the formation of network. Theoretically the glass transition temperature of ionic glass should depends on both the strength of ionic interaction and ionic crosslink density. To test whether the multivalency of anion has effect on the glass transition temperature, we prepared series of ionic glass with same cation (A_8-3) and different anions with same ion exchange method. The acids we tested have similar backbone structure and different carboxylic acids number. From glutaric acid to tricarballylic acid and 1,2,3,4-Butanetetracarboxylic acid, the carboxylic acid functional group number increase from 2 to 4 per molecule. Because of the same ion pair type, the ionic interaction strength in these ionic glasses is considered to be similar. The DSC trace of these ionic glasses has been shown in Figure 6. Not surprisingly, the glass transition temperature of ionic glasses increase with higher functionality of anion. In addition, compared with tricarballylic acid, citric acid provides same functionality but additional hydrogen bonding. This results in slightly higher T_g than ionic glass formed by tricarballylic acid. Interestingly, the glass transition ΔC_p decreases with increasing functionality. The same trend has been observed before in thiol-ene system. The more rigid network exhibit less enthalpy relaxation and smaller ΔC_p. The crosslink density will control the absorption of heat as temperature increases, i.e., the more flexible and lower crosslinked networks will have the highest heat capacities. Same trend goes with enthalpy relaxation which is mentioned previously. For glutaric acid anion, the enthalpy relaxation is present in DSC trace; which with higher crosslink density, it is not seen.

2.3.3 Mechanical properties and viscosity of ionic glass

The rheological measurement was performed using TA Instruments AR-G2 Rheometer. The geometry used was 8mm aluminum plates and the testing method was temperature sweep in oscillation mode. The frequency of dynamic loading was 1Hz and the strain was 0.3%. During the testing procedure, the gap was controlled between 900-

1200μm with active axial force adjustment. Temperature control was made using active cooling system and environmental test chamber.

Dried sample was transferred to aluminum plate on rheometer under nitrogen purge. Upon heating, the sample will turn into viscous liquid, which was easier to load correctly without any over/under filling or introducing any gas bubbles. After sample loading, a temperature sweep test (typical temperature range is -30~50 °C) was carried out. G' and G'' was obtained as a function of temperature. The cross point of G' and G'' was used to determine the glass transition temperature.
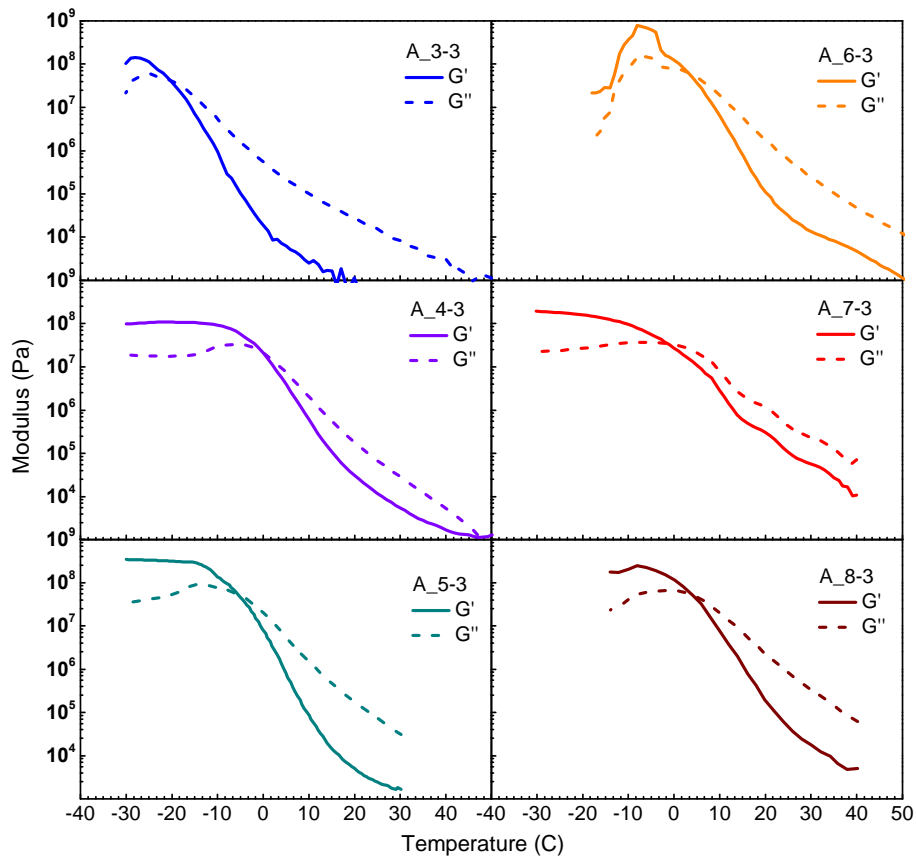
Figure 2.6 Temperature sweep measurement of ionic glass A_3-3 to A_8-3 at 1 Hz shear rate.

Figure 2.6 shows the dynamic temperature sweep data of ionic glass with different backbone length. Dynamic storage modulus (G') and loss modulus (G'') are plotted as a function of temperature. These ionic glass are thermoreversible, and rheological data collected on heating and cooling are highly reproducible with negligible hysteresis in T_{relax}

(1-2 °C difference). These figures shows the dramatic change of ionic glasses' viscoelastic property over a certain temperature range. At low temperature, the materials' rheological response is highly elastic (or solid-like) with G'>G''. The temperature-independent plateau in G' below certain temperature indicates well-defined ionic network at low temperature. Common value for this plateau storage modulus is 0.2-0.4 GPa. For comparison, typical molecular glasses and glass-forming ionic liquids have plateau modulus around 1 GPa. Similar to above mentioned molecular glasses, because of lacking of entanglement, the materials appear brittle.

At high temperature, the rheological response is predominantly viscous with G'<G''. The materials undergo a transition from viscous liquid-like behavior to elastic solid-like behavior. In supramolecular materials area, the crossover temperature where G'=G'' has been used as convenient indicator for T_{gel}. Here, we also used this crossover temperature as relaxation temperature. At this temperature, the ionic glass has a longest relaxation time comparable to the time scale of experiment ($\tau \approx \omega^{-1} = 10$ s). Compared with T_g obtained from DSC measurement, T_{relax} is a little higher because glass transition temperature is usually defined with $\tau \approx 100$ s.

It is worthwhile to point out that for supramolecular network, usually G' (G'') at T_{gel} is low; for ionic glass, the modulus at T_{gel} is around 40 MPa, which is similar to the rubbery plateau modulus of a rubber. This can be explained by lacking of chain entanglement in ionic glass.

2.4 Structure-property relationship of di-imidazolium ionic glass

The transition glass temperatures of the di-imidazole complexes with citric acid do not show an odd-even effect as in the di-ammonia network. In contrast, the T_g for the material are very similar near 253 K. The di-imidazole bromide salt displayed increased hydrophobicity by increasing the time it takes to dissolve in methanol. This phenomenon was observed when dissolving the bromide salt for the anion exchange column.
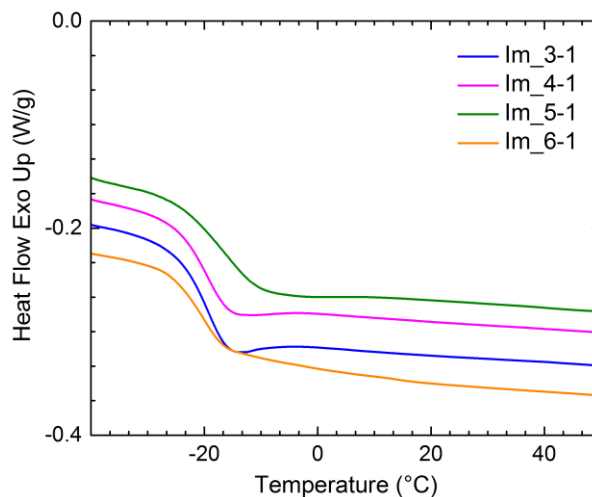
Figure 2.7 DSC curve of ionic glass Im_3-1 to Im_6-1 with citric acid as anion.

2.5 Experimental details

2.5.1. Materials and methods

All chemicals were purchased from Aldrich as highest purity grade and used without further purification. All reactions were performed under nitrogen/argon atmosphere. NMR spectra were recorded on Varian Unity 400 NB, Varian VXR 500 and Varian Unity 500 NB spectrometer. High resolution electrospray mass spectra were obtained on a Micromass Q-Tof Ultima. Elemental analysis was obtained from Exeter Analytical CE 440 CHN Analyzer and PerkinElmer 2400 Series II CHN/O Elemental Analyzer and Thermo Scientific Orin Ion Selective Electrodes.

DSC Measurement. The DSC measurement was performed using TA Instrument Q20 Differential Scanning Calorimeter equipped with a Liquid Nitrogen Cooling System (LNCS). Nitrogen was used as sample purge gas. Typical sample loading is 10-20 mg. Typical DSC measurement procedure includes 4 cyclic scans. One cyclic scan includes one heating and cooling process. The trace started from cooling from room temperature.

Temperature range for scan is -100~100 ℃ with heating/cooling rate 10℃/min. There was a slight difference between the first scan and the latter three scans due to thermal history of the sample. The latter three heating curves overlap with each other. The glass transition temperatures were determined at the inflection point of the step from the last heating scan.

Rheometer Measurement. The rheological measurement was performed using TA Instruments AR-G2 Rheometer. The geometry used was 8mm aluminum plates and the testing method was temperature sweep in oscillation mode. The frequency of dynamic loading was 1Hz and the strain was 0.3%. During the testing procedure, the gap was co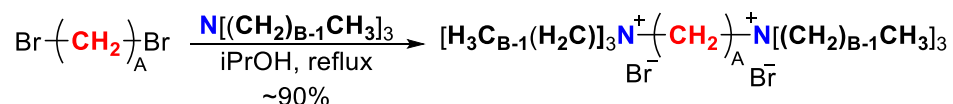ntrolled between 900-1200μm with active axial force adjustment. Temperature control was made using active cooling system and environmental test chamber.

Dried sample was transferred to aluminum plate on rheometer under nitrogen purge. Upon heating, the sample will turn into viscous liquid, which was easier to load correctly without any over/under filling or introducing any gas bubbles. After sample loading, a temperature sweep test (typical temperature range is -30~50 °C) was carried out. G' and G'' was obtained as a function of temperature. We used the cross point of G' and G'' to determine the glass transition temperature.

SWAXS Measurements. The wide angle X-ray diffraction was conducted for all samples using Bruker General Area Detector Diffraction System (GADDS) and Rigaku Miniflex 600 powder XRD. Powder diffraction was done at -10 ℃ and room temperature (RT). For all ionic glasses, we did not observe any structure difference from the XRD patterns at -10 ℃ and RT (above and below Tg). Figure 3 shows XRD of A_x-3 in 0-4 Å^{-1} Q range. All ionic glass in this series show four major diffraction features in this Q-range: (i) a peak (I) at low Q ($Q_{max} \approx 0.6$ Å^{-1}) that is relatively unaffected by backbone length in amplitude and peak position; (ii) a minor peak (II) at intermediate Q ($Q_{max} \approx 0.8\text{-}1.1$ Å^{-1}) that is strongly affected by backbone length in peak position; (iii) a peak (III) at high Q ($Q_{max} \approx 1.6$ Å^{-1}) that is relatively unaffected by backbone length in peak position; (iv) a minor shoulder peak (IV) at higher Q ($Q_{max} \approx 2.8\text{-}3.0$ Å^{-1}) that appears as a bump in the background.

2.5.2. Synthesis of diammonium ionic glass

$$Br\!-\!(CH_2)_A\!-\!Br \xrightarrow[\text{iPrOH, reflux} \atop \sim 90\%]{N[(CH_2)_{B\text{-}1}CH_3]_3} [H_3C_{B\text{-}1}(H_2C)]_3 N^+\!-\!(CH_2)_A\!-\!N^+[(CH_2)_{B\text{-}1}CH_3]_3$$
$$\qquad\qquad\qquad\qquad\qquad\qquad\qquad\qquad Br^- \qquad\quad Br^-$$

General procedure

Di-bromoalkane (20mmol) and tri-alkylamine (80mmol) was loaded into a round-bottom flask with nitrogen inlet and condenser, followed by adding 100mL appropriate solvent. For 1,3-dibromopropane, 1,4-dibromobutane, 1,5-dibromopentane, 1,6-dibromohexane, the solvent was ethanol, for 1,7-dibromoheptane, 1,8-dibromooctane, 1,9-dibromononane, the solvent was isopropanol or acetonitrile. For higher di-bromoalkane the solvent was methyl isobutyl ketone. The reactions were carried out under nitrogen atmosphere and at reflux temperature for 48-96 hours. For 1,3-dibromopropane, 1,4-dibromobutane, 1,5-dibromopentane, 1,6-dibromohexane, 1,7-dibromoheptane, 1,8-dibromooctane, 1,9-dibromononane reaction, the diammonium bromide salt was obtained by recrystallization using ethanol-ethyl acetate. For higher di-bromoalkane, the product was obtained by extraction using water-ethyl ether for multiple times followed by recrystallization in ethanol-ethyl acetate at -20 ℃.

N1,N1,N1,N3,N3,N3-hexapropylpropane-1,3-diaminium bromide

A white crystal was obtained after recrystallization in 95% yield. ^{1}H NMR (DMSO): δ 0.90 (t, 18, CH_3); 1.50-1.72 (br, 12, CH_2); 1.94-2.09 (br, 2, CH_2); 3.18-3.35 (br, 16, CH_2-N). ^{13}C NMR (DMSO): δ 10.50 (CH_3); 14.89, 15.50 (CH_2); 54.34 (CH_2-N); 59.44 (CH_2-N). ESI MS: 164.2. Elemental analysis: (theory: C, 51.64%; H, 9.91%; N, 5.74%) Found: C, 51.49%, H, 9.72%, N, 5.36%.

Figure 2.8 ¹H NMR spectrum of IG 3-3 diaminium bromide salts.

N1,N1,N1,N4,N4,N4-hexapropylbutane-1,4-diaminium bromide

A white crystal was obtained after recrystallization in 92% yield. ^{1}H NMR (DMSO): δ 0.91 (t, 18, CH_3); 1.57-1.70 (br, 16, CH_2); 3.10-3.27 (br, 16, CH_2-N). ^{13}C NMR (DMSO): δ 10.58 (CH_3); 14.81, 18.44 (CH_2); 57.22 (CH_2-N); 59.42 (CH_2-N). ESI MS: 171.2. Elemental analysis: (theory: C, 52.59%; H, 10.03%; N, 5.58%) Found: C, 52.27%, H, 9.63%, N, 5.19%.

Figure 2.9 ^{1}H NMR spectrum of IG 4-3 diaminium bromide salts.

N1,N1,N1,N5,N5,N5-hexapropylpentane-1,5-diaminium bromide

Figure 2.10 ^{1}H NMR spectrum of IG 5-3 diaminium bromide salts.

A white crystal was obtained after recrystallization in 90% yield. ^{1}H NMR (DMSO): δ 0.91 (t, 18, CH$_3$); 1.22-1.30 (br, 2, CH$_2$); 1.57-1.69 (br, 16, CH$_2$); 3.10-3.20 (br, 16, CH$_2$-N). ^{13}C NMR (DMSO): δ 10.57 (CH$_3$); 14.81, 20.85, 22.93(CH$_2$); 57.62 (CH$_2$-N); 59.26 (CH$_2$-N).

ESI MS: 178.2. Elemental analysis: (theory: C, 53.49%; H, 10.15%; N, 5.42%) Found: C, 53.32%, H, 10.29%, N, 5.25%.

N1,N1,N1,N6,N6,N6-hexapropylhexane-1,6-diaminium bromide

A white crystal was obtained after recrystallization in 95% yield. ^{1}H NMR (DMSO): δ 0.91 (t, 18, CH$_3$); 1.29-1.36 (br, 4, CH$_2$); 1.55-1.69 (br, 16, CH$_2$); 3.10-3.21 (br, 16, CH$_2$-N). ^{13}C NMR (DMSO): δ 10.55 (CH$_3$); 14.82, 21.02, 25.31(CH$_2$); 57.65 (CH$_2$-N); 59.20 (CH$_2$-N). ESI MS: 185.2. Elemental analysis: (theory: C, 54.34%; H, 10.26%; N, 5.28%) Found: C, 54.25%, H, 10.30%, N, 5.34%.
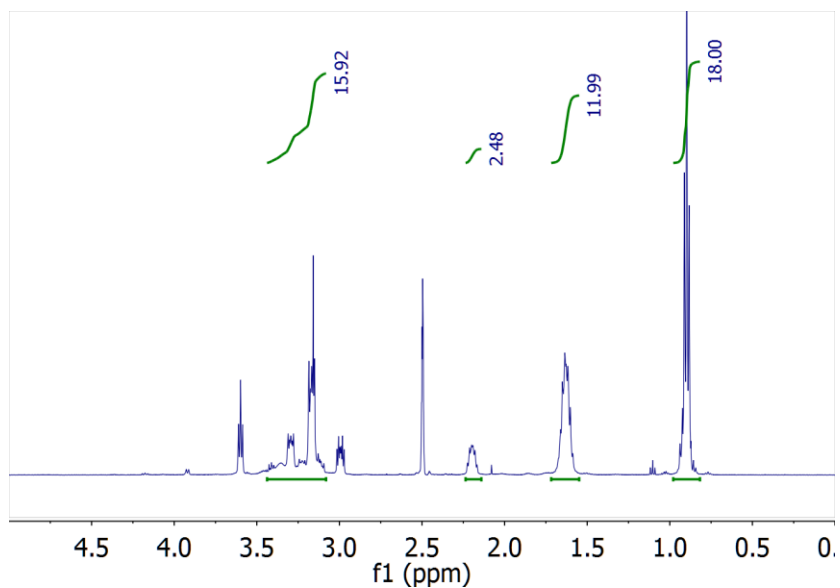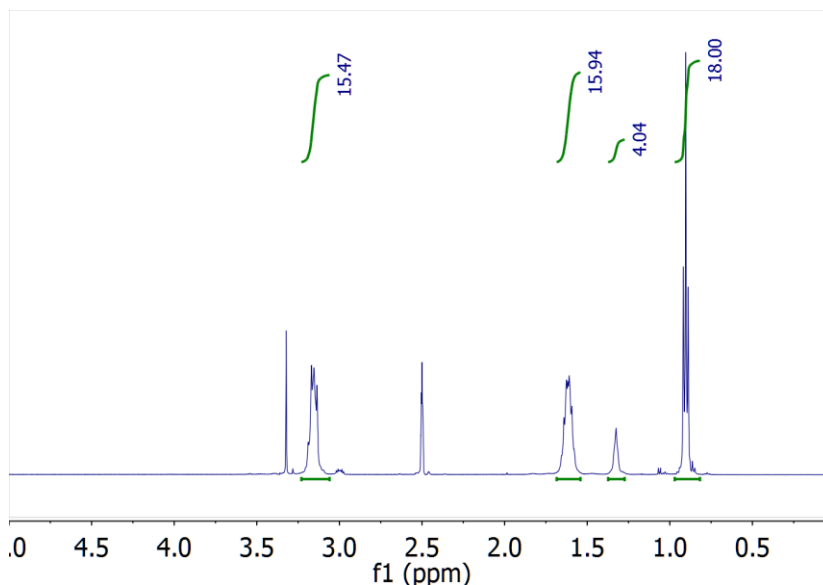

Figure 2.11 ^{1}H NMR spectrum of IG 6-3 diaminium bromide salts.

N1,N1,N1,N7,N7,N7-hexapropylheptane-1,7-diaminium bromide

A white crystal was obtained after recrystallization in 86% yield. ^{1}H NMR (DMSO): δ 0.90 (t, 18, CH$_3$); 1.24-1.40 (br, 6, CH$_2$); 1.54-1.67 (br, 16, CH$_2$); 3.08-3.21 (br, 16, CH$_2$-N). ^{13}C NMR (DMSO): δ 10.55 (CH$_3$); 14.82, 16.53, 21.02, 25.31 (CH$_2$); 57.62 (CH$_2$-N); 59.26 (CH$_2$-N). ESI MS: 192.2. Elemental analysis: (theory: C, 55.14%; H, 10.37%; N, 5.14%) Found: C, 55.04%, H, 10.34%, N, 5.19%.
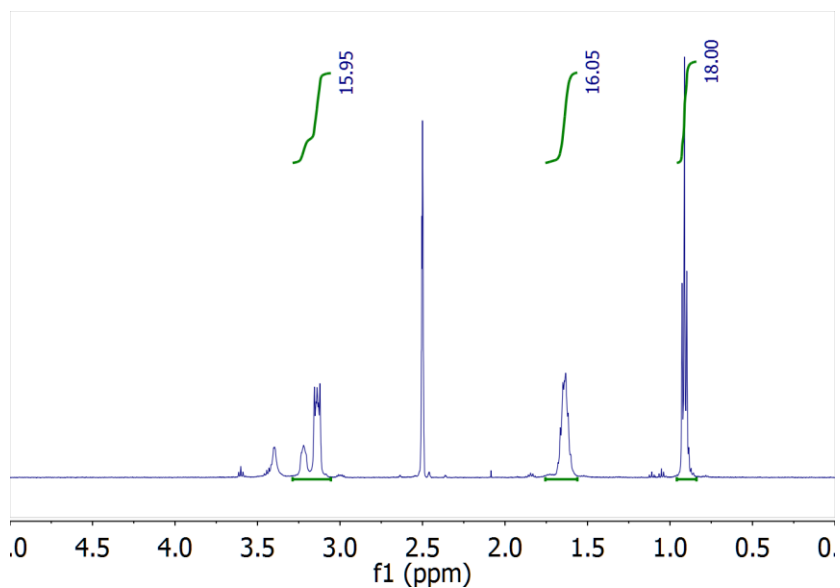
Figure 2.12 ^{1}H NMR spectrum of IG 7-3 diaminium bromide salts.

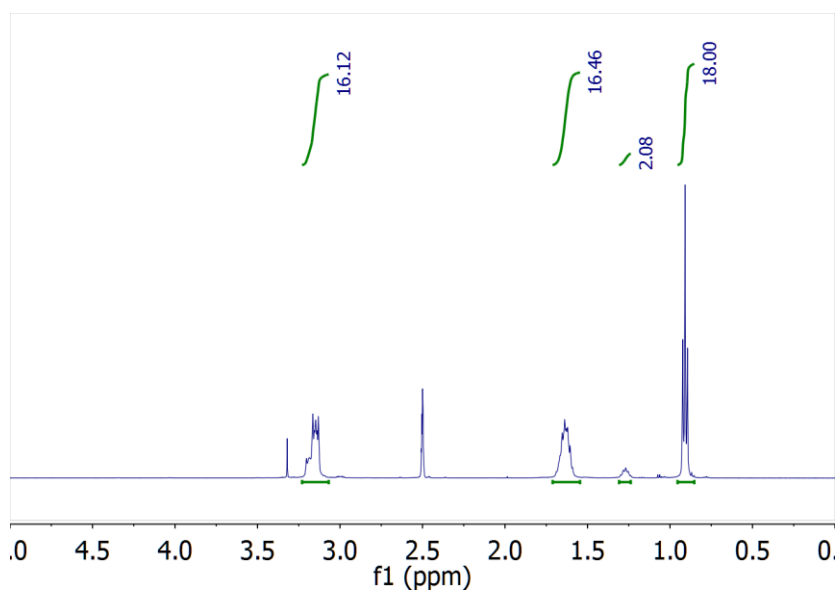**N1,N1,N1,N8,N8,N8-hexapropyloctane-1,8-diaminium bromide**
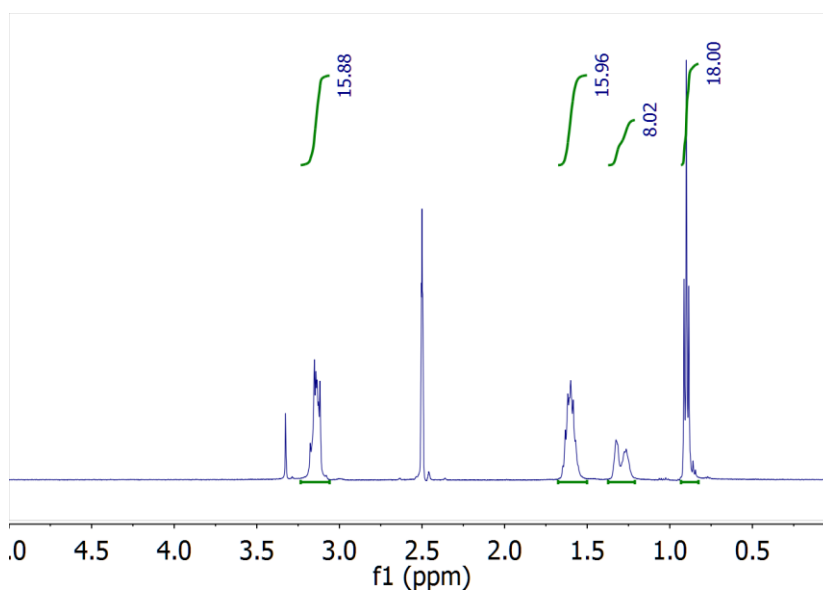
Figure 2.13 ^{1}H NMR spectrum of IG 8-3 diaminium bromide salts.

A white crystal was obtained after recrystallization in 90% yield. ^{1}H NMR (DMSO): δ 0.90 (t, 18, CH$_3$); 1.22-1.36 (br, 8, CH$_2$); 1.53-1.67 (br, 16, CH$_2$); 3.09-3.21 (br, 16, CH$_2$-N). ^{13}C NMR (DMSO): δ 10.55 (CH$_3$); 14.83, 16.52, 21.13, 25.79, 28.38 (CH$_2$); 57.81 (CH$_2$-N);

59.20 (CH$_2$-N). ESI MS: 199.2. Elemental analysis: (theory: C, 55.91%; H, 10.47%; N, 5.02%) Found: C, 55.43%, H, 10.48%, N, 5.08%.

N1,N1,N1,N9,N9,N9-hexapropylnonane-1,9-diaminium bromide

A white crystal was obtained after recrystallization in 82% yield. ^{1}H NMR (DMSO): δ 0.89 (t, 18, CH$_3$); 1.20-1.36 (br, 10, CH$_2$); 1.52-1.70 (br, 16, CH$_2$); 3.08-3.23 (br, 16, CH$_2$-N). ^{13}C NMR (DMSO): δ 10.54 (CH$_3$); 14.82, 21.12, 25.88, 28.45, 28.79 (CH$_2$); 57.81 (CH$_2$-N); 59.22 (CH$_2$-N). ESI MS: 206.2. Elemental analysis: (theory: C, 56.64%; H, 10.56%; N, 4.89%) Found: C, 56.53%, H, 10.50%, N, 4.92%.
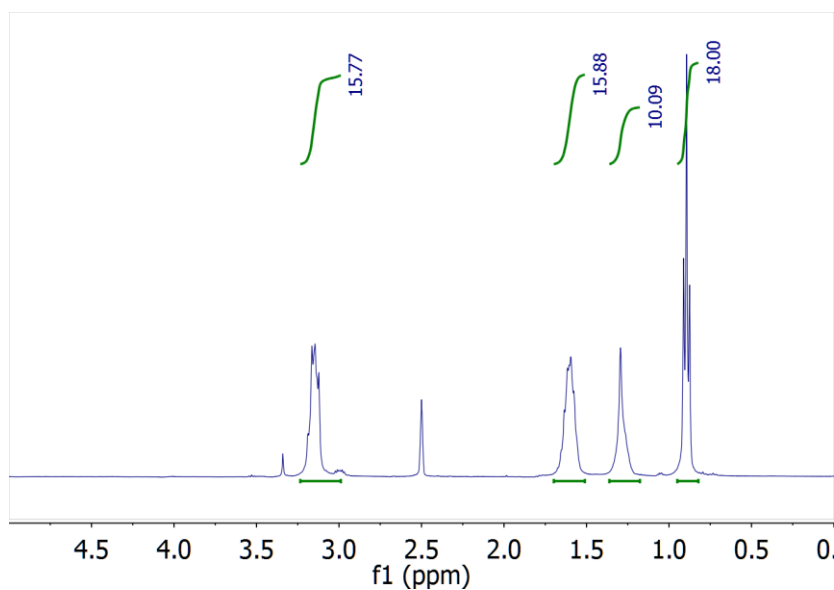
Figure 2.14 ^{1}H NMR spectrum of IG 9-3 diaminium bromide salts.

N1,N1,N1,N10,N10,N10-hexapropyldecane-1,10-diaminium bromide

A pale yellow crystal was obtained after recrystallization in 80% yield. ^{1}H NMR (DMSO): δ 0.89 (t, 18, CH$_3$); 1.20-1.36 (br, 12, CH$_2$); 1.50-1.70 (br, 16, CH$_2$); 3.09-3.23 (br, 16, CH$_2$-N). ^{13}C NMR (DMSO): δ 10.55 (CH$_3$); 14.81, 16.54, 21.11, 25.88, 28.51, 28.85 (CH$_2$);

57.81 (CH$_2$-N); 59.20 (CH$_2$-N). ESI MS: 213.23. Elemental analysis: (theory: C, 57.33%; H, 10.65%; N, 4.78%) Found: C, 57.12%, H, 10.51%, N, 4.80%.
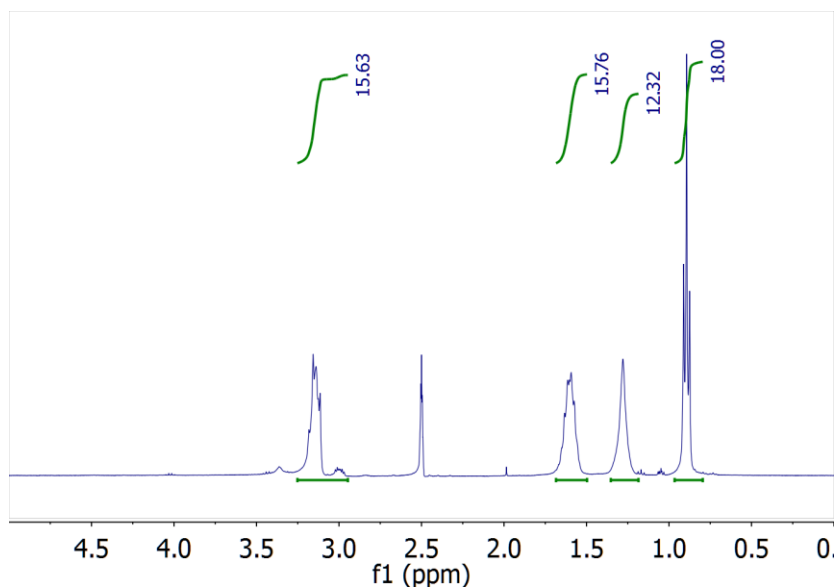
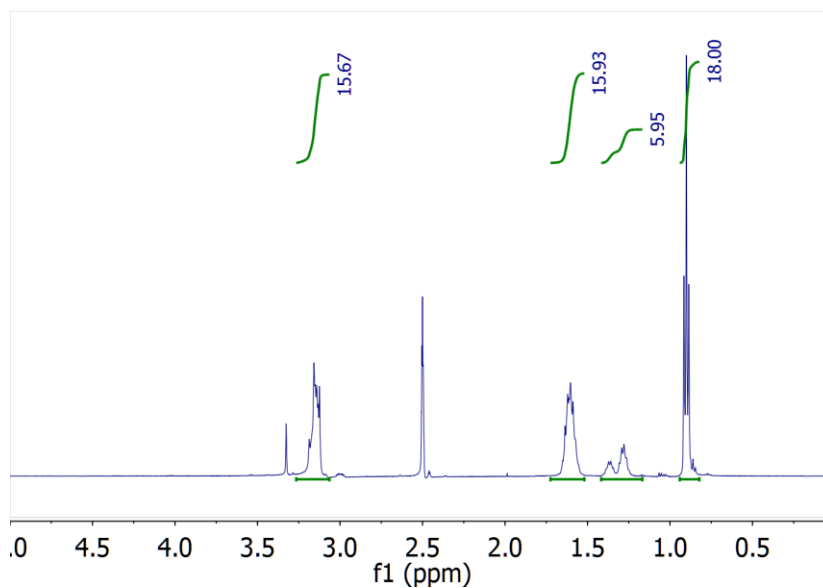*Figure 2.15 ^{1}H NMR spectrum of IG 10-3 diaminium bromide salts.*

**N1,N1,N1,N12,N12,N12-hexapropyldodecane-1,12-diaminium bromide**
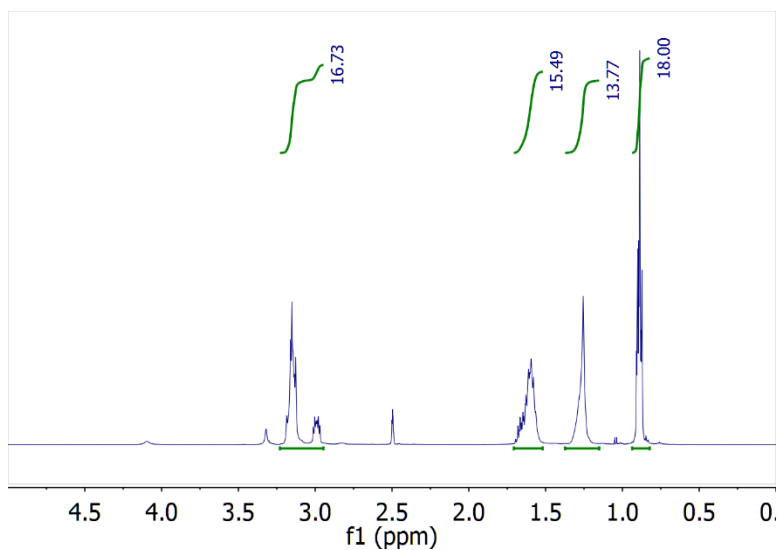
Figure 2.16 ^{1}H NMR spectrum of IG 10-3 diaminium bromide salts.

A pale yellow crystal was obtained after recrystallization in 80% yield. ^{1}H NMR (DMSO): δ 0.89 (t, 18, CH$_3$); 1.20-1.35 (br, 16, CH$_2$); 1.50-1.70 (br, 16, CH$_2$); 3.08-3.22 (br, 16, CH$_2$-N). ^{13}C NMR (DMSO): δ 10.55 (CH$_3$); 14.82, 16.55, 18.96, 25.88, 28.52, 28.98 (CH$_2$);

57.81 (CH$_2$-N); 59.20 (CH$_2$-N). ESI MS: 227.3. Elemental analysis: (theory: C, 58.62%; H, 10.82%; N, 4.56%) Found: C, 58.44%, H, 10.78%, N, 4.57%.
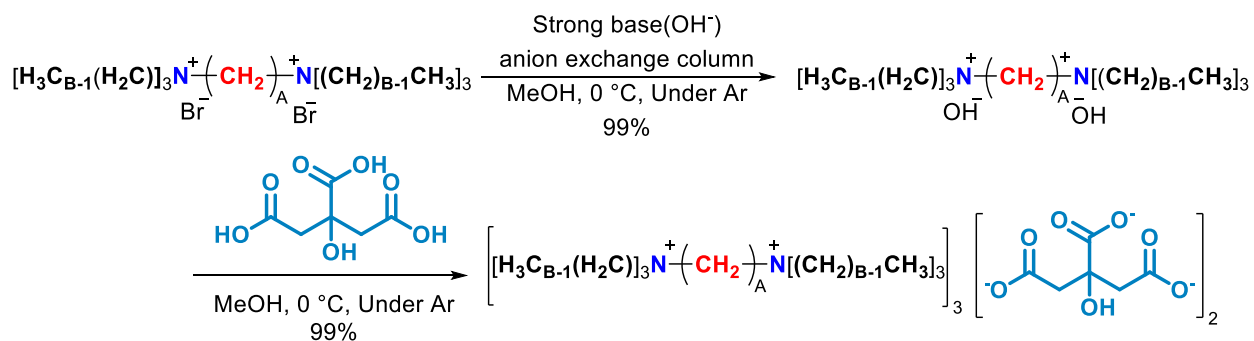
General Procedure

The diammonium bromide salt was dissolved in methanol. The solution was added into an anion exchange column (Dowex® Monosphere® 550A UPW type 1 strong base anion exchange resin, preliminary elution and wash was carried out using methanol). In order to maximize the conversion of bromide anion into hydroxide anion, the column was run carefully and the eluent was protected under argon atmosphere. The eluent was reacted directly (*in situ*) with citric acid in methanol in ice bath. After the anion exchange column, the solution was evaporated. The sample was freeze-dried or dried under high vacuum at 50 ℃ for 48h. The materials were obtained at room temperature. For most of these ionic glasses, their T$_g$ are below room temperature, so they were obtained as viscous liquids at ambient environment. Seradyn Aquatest CMA Karl-Fisher titrator was used to determine the water content in the final product. All the products have water content below 1800 ppm. For elemental analysis, air sensitive capsules were used to avoid the effect from moisture in air. The bromide analysis was done to confirm the conversion of ion exchange. For all samples, bromide content is less than 100ppm.

N1,N1,N1,N3,N3,N3-hexapropylpropane-1,3-diaminium citrate

A transparent viscous liquid was obtained after drying in >99% yield. ^{1}H NMR (D$_2$O): δ 0.95 (t, 54, CH$_3$); 1.64-1.76 (br, 36, CH$_2$); 2.00-2.10(br, 6, CH$_2$); 2.59 (d, 4, CH$_2$); 2.64 (d, 4, CH$_2$); 3.20-3.27 (br, 48, CH$_2$-N). ^{13}C NMR (D$_2$O): δ 9.90 (CH$_3$); 14.94-15.28 (CH$_2$) ; 45.32 (CH$_2$-COO$^-$); 54.49 (CH$_2$-N); 60.47 (CH$_2$-N); 75.01 (C-OH); 178.46 (COO$^-$), ESI MS: positive ion 163.7 m/z, negative ion 190.9 m/z. Elemental analysis: (theory: C,66.04%; H,11.38%; N, 6.16%) Found: C, 65.83%, H, 11.26%, N, 5.89%.

N1,N1,N1,N4,N4,N4-hexapropylbutane-1,4-diaminium citrate

A transparent viscous liquid was obtained after drying in >99% yield. ^{1}H NMR (D$_2$O): δ 0.94 (t, 54, CH$_3$); 1.63-1.79 (br, 48, CH$_2$); 2.57 (d, 4, CH$_2$); 2.63 (d, 4, CH$_2$); 3.13-3.31 (br, 48, CH$_2$-N). ^{13}C NMR (D$_2$O): δ 9.89 (CH$_3$); 14.97-15.17 (CH$_2$) ;18.66 (CH$_2$); 45.54 (CH$_2$-COO$^-$); 57.38 (CH$_2$-N); 60.16 (CH$_2$-N); 74.86 (C-OH); 181.51 (COO$^-$), ESI MS: positive ion 171.2 m/z, negative ion 190.9 m/z. Elemental analysis: (theory: C,66.62%; H,11.47%; N, 5.98%) Found: C, 66.53%, H, 11.12%, N, 5.76%.

N1,N1,N1,N5,N5,N5-hexapropylpentane-1,5-diaminium citrate

A transparent viscous liquid was obtained after drying in >99% yield. ^{1}H NMR (D$_2$O): δ 0.94 (t, 54, CH$_3$); 1.34-1.41 (br, 6, CH$_2$); 1.63-1.78 (br, 48, CH$_2$); 2.57 (d, 4, CH$_2$); 2.62 (d, 4, CH$_2$); 3.11-3.26 (br, 48, CH$_2$-N). ^{13}C NMR (D$_2$O): δ 9.92 (CH$_3$); 14.97 (CH$_2$); 21.12-22.86 (CH$_2$) ; 45.61 (CH$_2$-COO$^-$); 58.00 (CH$_2$-N); 60.06 (CH$_2$-N); 75.28 (C-OH); 181.20 (COO$^-$), ESI MS: positive ion 178.7 m/z, negative ion 190.9 m/z. Elemental analysis: (theory: C,67.18%; H,11.55%; N, 5.80%) Found: C, 66.88%, H, 11.08%, N, 5.51%.

N1,N1,N1,N6,N6,N6-hexapropylhexane-1,6-diaminium citrate

A transparent viscous liquid was obtained after drying in >99% yield. ^{1}H NMR (D$_2$O): δ 0.92 (t, 54, CH$_3$); 1.29-1.40 (br, 12, CH$_2$); 1.55-1.73 (br, 48, CH$_2$); 2.58 (d, 4, CH$_2$); 2.63 (d, 4, CH$_2$); 3.10-3.22 (br, 48, CH$_2$-N). ^{13}C NMR (D$_2$O): δ 9.94 (CH$_3$); 14.96 (CH$_2$); 21.12-25.38 (CH$_2$) ; 45.42 (CH$_2$-COO$^-$); 58.23 (CH$_2$-N); 59.98 (CH$_2$-N); 75.10 (C-OH); 178.66 (COO$^-$), ESI MS: positive ion 185.8 m/z, negative ion 190.9 m/z. Elemental analysis: (theory: C,67.70%; H,11.63%; N, 5.64%) Found: C, 67.55%, H, 11.48%, N, 5.32%.

N1,N1,N1,N7,N7,N7-hexapropylheptane-1,7-diaminium citrate

A transparent viscous liquid was obtained after drying in >99% yield. ^{1}H NMR (D$_2$O): δ 0.91 (t, 54, CH$_3$); 1.21-1.44 (br, 18, CH$_2$); 1.54-1.73 (br, 48, CH$_2$); 2.56 (d, 4, CH$_2$); 2.61 (d, 4, CH$_2$); 3.00-3.17 (br, 48, CH$_2$-N). ^{13}C NMR (D$_2$O): δ 9.98 (CH$_3$); 14.96 (CH$_2$); 21.15-28.01 (CH$_2$) ; 45.45 (CH$_2$-COO$^-$); 58.41 (CH$_2$-N); 59.95 (CH$_2$-N); 75.10 (C-OH); 178.65 (COO$^-$), ESI MS: positive ion 192.7 m/z, negative ion 190.9 m/z. Elemental analysis: (theory: C,68.19%; H,11.71%; N, 5.48%) Found: C, 68.05%, H, 11.42%, N, 5.23%.

N1,N1,N1,N8,N8,N8-hexapropyloctane-1,8-diaminium citrate

A transparent viscous liquid was obtained after drying in >99% yield. ^{1}H NMR (D$_2$O): δ 0.93 (t, 54, CH$_3$); 1.28-1.39 (br, 24, CH$_2$); 1.55-1.73 (br, 48, CH$_2$); 2.58 (d, 4, CH$_2$); 2.63 (d, 4, CH$_2$); 3.06-3.21 (br, 48, CH$_2$-N). ^{13}C NMR (D$_2$O): δ 9.93 (CH$_3$); 14.94 (CH$_2$); 21.20-28.24 (CH$_2$) ; 45.49 (CH$_2$-COO$^-$); 58.48 (CH$_2$-N); 59.94 (CH$_2$-N); 75.18 (C-OH); 177.25 (COO$^-$), ESI MS: positive ion 199.8 m/z, negative ion 190.9 m/z. Elemental analysis: (theory: C,68.66%; H,11.78%; N, 5.34%) Found: C, 68.32%, H, 11.56%, N, 5.20%.

N1,N1,N1,N9,N9,N9-hexapropylnonane-1,9-diaminium citrate

A transparent viscous liquid was obtained after drying in >99% yield. ^{1}H NMR (D$_2$O): δ 0.92 (t, 54, CH$_3$); 1.29-1.40 (br, 30, CH$_2$); 1.54-1.73 (br, 48, CH$_2$); 2.57 (d, 4, CH$_2$); 2.62 (d, 4, CH$_2$); 3.10-3.23 (br, 48, CH$_2$-N). ^{13}C NMR (D$_2$O): δ 9.97 (CH$_3$); 14.95 (CH$_2$); 21.25-28.46 (CH$_2$) ; 45.48 (CH$_2$-COO$^-$); 58.49 (CH$_2$-N); 59.97 (CH$_2$-N); 75.20 (C-OH); 178.36 (COO$^-$), ESI MS: positive ion 206.7 m/z, negative ion 190.9 m/z. Elemental analysis: (theory: C,69.10%; H,11.85%; N, 5.20%) Found: C, 68.90%, H, 11.65%, N, 5.13%.

N1,N1,N1,N10,N10,N10-hexapropyldecane-1,10-diaminium citrate

A transparent viscous liquid was obtained after drying in >99% yield. ^{1}H NMR (D$_2$O): δ 0.92 (t, 54, CH$_3$); 1.30-1.40 (br, 36, CH$_2$); 1.55-1.74 (br, 48, CH$_2$); 2.58 (d, 4, CH$_2$); 2.63 (d, 4, CH$_2$); 3.11-3.25 (br, 48, CH$_2$-N). ^{13}C NMR (D$_2$O): δ 9.96 (CH$_3$); 14.94 (CH$_2$); 21.26-28.87 (CH$_2$) ; 45.49 (CH$_2$-COO$^-$); 58.48 (CH$_2$-N); 59.97 (CH$_2$-N); 75.21 (C-OH); 178.52

(COO⁻), ESI MS: positive ion 213.8 m/z, negative ion 190.9 m/z. Elemental analysis: (theory: C,69.52%; H,11.91%; N, 5.07%) Found: C, 69.40%, H, 11.82%, N, 5.01%.

N1,N1,N1,N12,N12,N12-hexapropyldodecane-1,12-diaminium citrate

A transparent viscous liquid was obtained after drying in >99% yield. ^{1}H NMR (D$_2$O): δ 0.92 (t, 54, CH$_3$); 1.31-1.40 (br, 48, CH$_2$); 1.54-1.74 (br, 48, CH$_2$); 2.58 (d, 4, CH$_2$); 2.63 (d, 4, CH$_2$); 3.10-3.24 (br, 48, CH$_2$-N). ^{13}C NMR (D$_2$O): δ 9.96 (CH$_3$); 14.95 (CH$_2$); 19.10-28.87 (CH$_2$) ; 45.49 (CH$_2$-COO⁻); 58.46 (CH$_2$-N); 59.95 (CH$_2$-N); 75.22 (C-OH); 177.66 (COO⁻), ESI MS: positive ion 227.8 m/z, negative ion 190.9 m/z. Elemental analysis: (theory: C,70.30%; H,12.03%; N, 4.82%) Found: C, 69.98%, H, 11.86%, N, 4.63%.

2.5.3. Synthesis of diimidazolium ionic glass
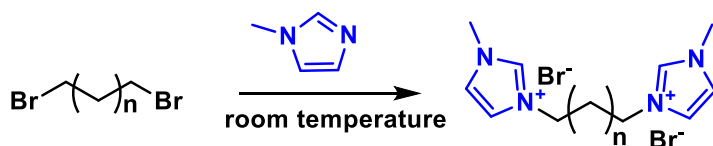
General procedure: The reaction was done at room temperature in a standard atmosphere. The reaction proceeded after massing α,ω-dibromoalkane (1 equivalent) and substituted imidazole compound (4 equivalents). Methyl imidazole was added to a round bottom flask followed by the addition of α,ω-dibromoalkane drop wise and then reacted for 48 hours. The product, a di-substituted alkyl imidozole salt, was purified by recrystallization at 80 ℃ with ethanol and ethyl acetate.

3,3'-(propane-1,3-diyl)bis(1-methyl-1H-imidazol-3-ium) bromide
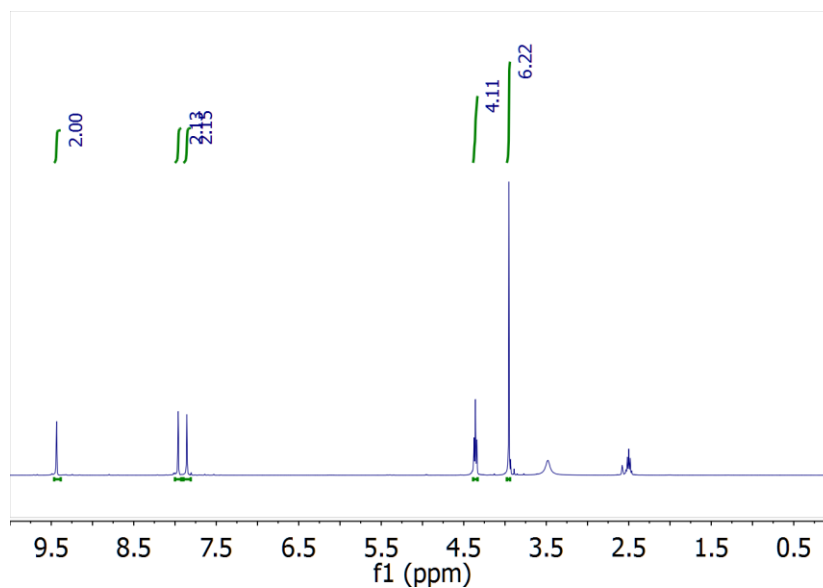
Figure 2.17 ^{1}H NMR spectrum of ImIG 3-1 diimidazolium bromide salts.

A white crystal was obtained after recrystallization in 93% yield. ^{1}H NMR (DMSO): δ 3.48 (br, 2, CH$_2$); δ 3.95 (s, 6, CH$_3$); δ 4.34 (t, 4, CH$_2$-N); δ 7.86 (s, 2, CH); δ 7.96 (s, 2, CH); δ 9.44 (s, 2, CH).

3,3'-(butane-1,4-diyl)bis(1-methyl-1H-imidazol-3-ium) bromide
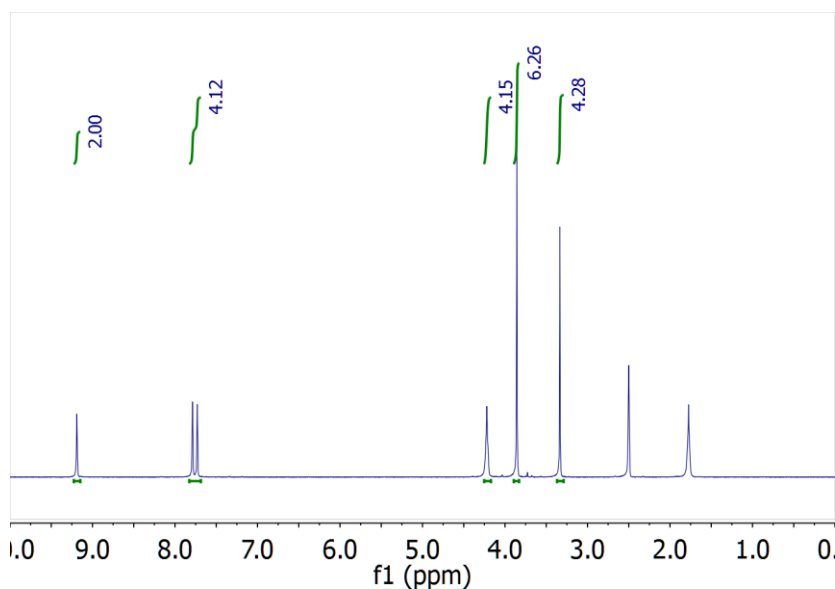
Figure 2.18 ^{1}H NMR spectrum of ImIG 4-1 diimidazolium bromide salts.

A white crystal was obtained after recrystallization in 90% yield. ^{1}H NMR (DMSO): δ 3.33 (br, 4, CH$_2$); δ 3.86 (br, 6, CH$_3$); δ 4.22 (br, 4, CH$_2$); δ 7.73 (s, 2, CH); δ 7.79 (s, 2, CH); δ 9.19 (s, 2, CH).

3,3'-(pentane-1,5-diyl)bis(1-methyl-1H-imidazol-3-ium) bromide

A white crystal was obtained after recrystallization in 95% yield. ^{1}H NMR (DMSO): δ 1.21 (q, 2, CH$_2$); δ 1.81 (q, 4, CH$_2$); δ 3.86 (s, 6, CH$_2$); δ 4.17 (t, 4, CH$_2$-N), δ 7.73 (s, 2 CH); δ 7.79 (s, 2, CH); δ 9.17 (s, 2, CH).
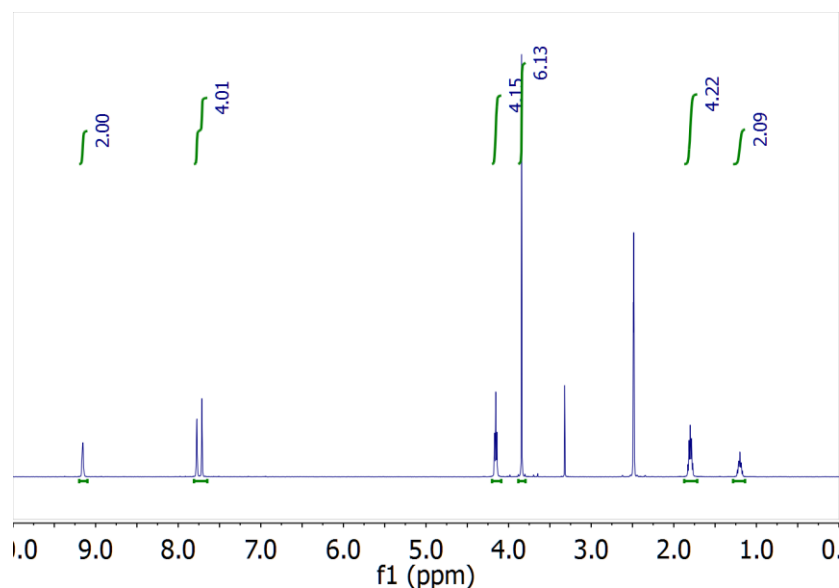
Figure 2.19 ^{1}H NMR spectrum of ImIG 5-1 diimidazolium bromide salts.

3,3'-(hexane-1,6-diyl)bis(1-methyl-1H-imidazol-3-ium) bromide

A white crystal was obtained after recrystallization in 90% yield. ^{1}H NMR (DMSO): δ 1.26 (t, 4, CH$_2$); δ 1.78 (m, 4, CH$_2$); δ 3.86 (s, 6, CH$_2$); δ 4.17 (t, 4, CH$_2$-N), δ 7.73 (s, 2 CH); δ 7.81 (s, 2, CH); δ 9.22 (s, 2, CH).
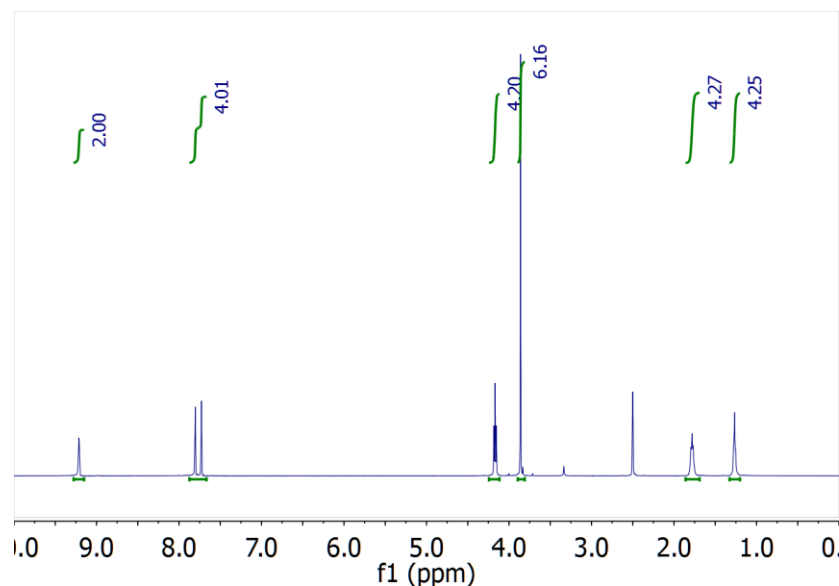
Figure 2.20 ^1H NMR spectrum of ImIG 6-1 diimidazolium bromide salts.

2.6 References

(1)   Angell, C. A. *Science* **1995**, *267*, 1924–1935.

(2)   Martinez, L. M.; Angell, C. a. *Nature* **2001**, *410*, 663–667.

(3)   Angell, C. A. *Proc. Natl. Acad. Sci. U. S. A.* **1995**, *92*, 6675–6682.

(4)   Shirota, Y.; Kageyama, H. *Chem. Rev.* **2007**, *107*, 953–1010.

(5)   Shirota, Y. *J. Mater. Chem.* **2000**, *10*, 1–25.

(6)   Dai, J.; Chang, S.; Hamad, A.; Yang, D. *Chem. Mater.* **2006**, *18*, 3404–3411.

(7)   Sciences, N. **2007**.

(8)   Tanino, T.; Yoshikawa, S.; Ujike, T.; Nagahama, D.; Moriwaki, K.; Takahashi, T.; Kotani, Y.; Nakano, H.; Shirota, Y. *J. Mater. Chem.* **2007**, *17*, 4953.

(9)   Conboy, J. C.; Messmer, M. C.; Richmond, G. L. **1998**, 6722–6727.

(10)   Zhao, Y.; Liu, X.; Lu, X.; Zhang, S.; Wang, J.; Wang, H.; Gurau, G.; Rogers, R. D.; Su, L.; Li, H. *J. Phys. Chem. B* **2012**, *116*, 10876–10884.

(11)   Jose, R.; Patel, T. J.; Cather, T. A.; Grebowicz, J.; Han, H.; Bhowmik, P. K.; Agra-Kooijman, D. M.; Kumar, S. *J. Colloid Interface Sci.* **2013**, *411*, 61–68.

(12)   Xu, W.; Cooper, E. I.; Angell, C. A. *J. Phys. Chem. B* **2003**, *107*, 6170–6178.

(13)   Dlubek, G.; Yu, Y.; Krause-Rehberg, R.; Beichel, W.; Bulut, S.; Pogodina, N.;

Krossing, I.; Friedrich, C. *J. Chem. Phys.* **2010**, *133*, 124502.

(14)   Shi, C.; Li, S.; Zhang, W.; Qiu, L.; Yan, F. *J. Mater. Chem. A* **2013**, *1*, 13956-13962.

(15)   Lowe, A. B.; McCormick, C. L. *Chem. Rev.* **2002**, *102*, 4177–4189.

(16)   Pas, S. J.; Dargusch, M. S.; MacFarlane, D. R. *Phys. Chem. Chem. Phys.* **2011**, *13*, 12033–12040.

(17)   Dean, P. M.; Turanjanin, J.; Yoshizawa-Fujita, M.; MacFarlane, D. R.; Scott, J. L. *Cryst. Growth Des.* **2009**, *9*, 1137–1145.

(18)   Zheng, W.; Mohammed, A.; Hines, L. G.; Xiao, D.; Martinez, O. J.; Bartsch, R. A.; Simon, S. L.; Russina, O.; Triolo, A.; Quitevis, E. L. *J. Phys. Chem. B* **2011**, *115*, 6572–6584.

(19)   Rocha, M. A. A.; Neves, C. M. S. S.; Freire, M. G.; Russina, O.; Triolo, A.; Coutinho, J. A. P. C.; Santos, L. M. N. B. F. *J. Phys. Chem. B* **2013**, *117*, 10889–10897.

(20)   Hayes, R.; Imberti, S.; Warr, G. G.; Atkin, R. *Phys. Chem. Chem. Phys.* **2011**, *13*, 13544–13551.

CHAPTER 3

ODD-EVEN EFFECT IN NETWORK-FORMING IONIC GLASS AND LIQUID

3.1 Abstract

Odd-even effects, the non-monotonic dependency of physical properties on odd/even structural units, are widely observed in homologous series of crystalline materials. However, such alternation is not expected for molecular amorphous materials. Herein, we report the synthesis of a class of network-forming ionic glasses (IG) using multivalent ammonium cations and citrate anions. The glass transition temperatures of these amorphous solids show an alternating pattern with increasing backbone length. To understand the phenomenon's molecular origin, we performed incoherent elastic neutron scattering measurements of the nano-second atomic dynamics. Our results suggest that the molecules' mobility, thus the glass transition temperature, correlates with their structural symmetry.

3.2 Introduction

In 1877, A. Baeyer discovered that the melting point of fatty acids does not exhibit a monotonic increase with increasing chain length.[1] Later on, almost all standard organic chemistry textbooks mention that even-membered n-alkanes and most of their α- and α,ω-substituents have higher melting temperatures than the odd membered counterparts. Besides melting point,[2,3] odd-even effects of various systems have been shown in other properties such as fusion/sublimation enthalpy,[4] density,[5] mechanical properties[6,7] and surface properties[8]. In general, "packing effects" are used to explain this alternation trend in crystalline materials. However, periodic packing does not exist in amorphous solids. Thus, the odd-even effect was not expected for molecular amorphous materials. For example, in most semi-crystalline polymer homologues, although the melting temperatures (T_m) show odd-even alternation, the glass transition temperatures (T_g) only have a

monotonic trend.[9,10] Here we report that the odd-even effect also exists in the fully amorphous state. We synthesized homologous network-forming ionic glasses where organic multivalent cations and anions are connected primarily by electrostatic interactions. We found that the glass transition temperatures of this class of ionic glasses show a non-monotonic rise with increasing backbone chain length. We further investigated this odd-even effect by measuring the nano-second hydrogen mean squared displacement (MSD). The experiments described herein may be useful in guiding the design and the development of future functional amorphous materials. In addition, influence of molecular symmetry on the glass transition is important for understanding and ultimately controlling dynamical slowing by tailoring the molecular architecture and intermolecular interactions.[11,12,13]

3.3 Odd-even glass transition temperatures in network-forming ionic glass homolog

Increasing the spike length decreases the glass transition temperature (Table 3.1). Both electrostatic and van der Waals forces likely influence the phase behavior. Because electrostatic force is inversely proportional to the square of distance, increasing the length of side chains increases the steric hindrance between positive and negative charges. As a result, even though the van der Waals forces between segments may increase, glass transition temperature drops due to weaker electrostatic interactions. Based on this observation, side chain length was reduced in order to increase the glass transition
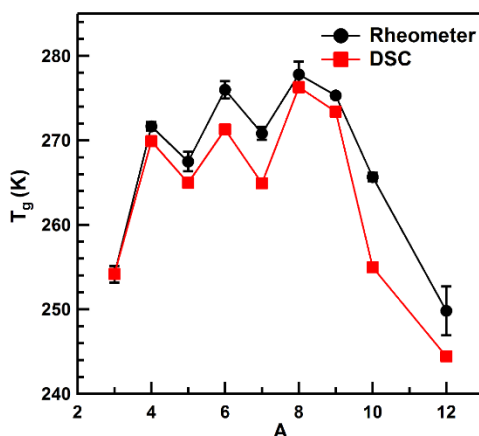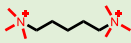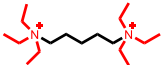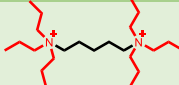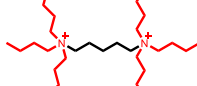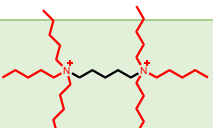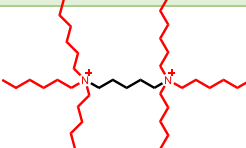
Figure 3.1 Odd-even dependence of the glass transition temperatures (determined by both rheology and DSC) of IGs by varying spacer alkyl chain length (IG A-3) (Copyright © 2014 American Chemical Society)

47

temperature. However, no glassy solids were obtained when the side chains were reduced to a methyl or ethyl group. When the side chains are reduced, the cations and anions can get closer, resulting stronger electrostatic attraction that leads to stable nano-crystals. Instead, opaque semi-crystal samples were obtained. These results demonstrate that the ionic interaction strength can be fine-tuned by tailoring the structure of the building blocks as long as the spikes are long enough to frustrate crystallization.

Table 3.1 T_g of ionic glass with different spikes length

Cation structure (anions are citrate)		T_g (K) (determined by DSC)
IG5-1		N/A
IG5-2		N/A
IG5-3		264K
IG5-4		250K
IG5-5		245K
IG5-6		223K

Investigating the dependence of T_g on spacer length, the overall trend exhibits a peak shape (Figure 3.1). The drop in T_g for long spacer lengths is explained by the competition between the electrostatic and van der Waals forces. An unexpected odd-even effect was observed in the spacer length study. IGs with an even number of methylene groups consistently have higher T_g than the odd-numbered IGs. The magnitude of the odd-even effect varies from system to system. For our IGs, the maximum difference in neighboring T_g is 15K. To compare, for n-alkane, the maximum difference of neighboring

T_m is about 30 K;[2] for some polyesters, it ranges from 15-100K ;[6,10,14] for α,ω-diamides, it can be as large as 130K.[4] The alternation amplitude decreases with longer chains, which is consistent with n-alkanes and its derivates.[2,4] When n>9, the odd-even effect was not observed suggesting the effect from weaker ionic interaction per molecular volume becomes more prominent. To the best of our knowledge, this is the first time such odd-even effect of T_g has been observed in ionic networks.

Unlike crystallization, glass transition is not a thermodynamic transition, but rather a dynamic slowing-down process. Therefore, packing effects in crystalline materials cannot be applied directly to amorphous solids. To understand the odd-even phenomenon from the dynamic point of view, we measured the atomistic dynamics of IGs using incoherent elastic neutron scattering (IENS). IENS probes the effective Debye-Waller factor $\exp\left(-\frac{1}{6}\langle r^2 \rangle Q^2\right)$ averaged over the nanosecond time resolution window, which directly yields the hydrogen mean squared displacement (MSD).[15] For our IG system, most
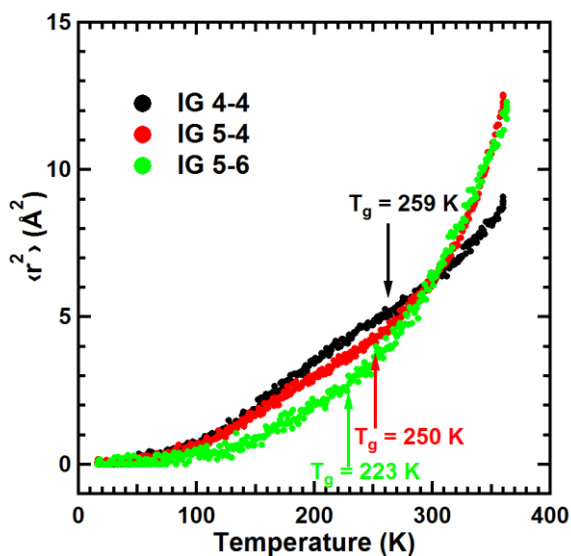
Figure 3.2 Nano-second hydrogen mean squared displacement (MSD) of three selective IGs extracted from elastic incoherent neutron scattering experiments. (The glass transition temperatures are determined by DSC.) (Copyright © 2014 American Chemical Society)

of the hydrogen atoms are in non-spherical cations, so the MSD would reflect mostly the cations' behavior. Detailed data analysis can be found in the experimental section (Figure 3.5). Three samples (IG 4-4, IG 5-4 and IG 5-6) were chosen in order to decouple the contributions to MSD from the side chains and backbone. As shown in Figure 3.2, typical

IG's nanosecond hydrogen MSD as a function of temperature can be divided into three regimes: (i) below 100 K, MSD shows pure harmonic behavior, almost all relaxational degrees of freedom freeze; (ii) From 100K to 250 K, anharmonic motions start contributing. IG 4-4 and IG 5-4 with the same spike length show similar temperature dependence, while IG 5-6 with longer hexyl side chain exhibits slower motions. This contrast suggests that the motion of the IG alkyl side chain (spikes group) dominates in this temperature range. In comparison, the backbone is primarily immobile in this regime as the ionic cross-links behave like "anchors" and restrict the backbone diffusional movement; (iii) above 250K, which is close to the glass transition temperature, the hydrogen MSDs increase dramatically. IG 5-4 and IG 5-6 with the same backbone length behave almost identically while IG 4-4 moves much slower. Therefore we can reasonably conclude that the nanosecond molecular motions of IG are determined by the backbone rather than the side chain in this temperature range.

Comparing IG 4-4 and IG 5-4, which have the same number of spike groups but adjacent number of spacer groups, the main difference of their MSD lies in regime (iii) ($T>T_g$), where IG 4-4 molecules exhibit considerably slower motions compared to IG 5-4. This measurement of the molecular mobility explains why IG 4-4 has a higher T_g than its odd membered counterparts. Indeed, the mobility of the molecules is influenced by their structural symmetry, central symmetry for even membered IG and mirror symmetry for odd membered IG, which ultimately determines the configurational entropy of the system and thus affects the glass transition temperature. Another interesting feature of the MSD plot is that all three curves seem to have a common crossover point around 300 K, which is under current investigation.

3.4 Dynamic odd-even effect in network-forming ionic liquids

Despite the existence of odd-even effect in various systems, odd-even effect of dynamic properties was rarely reported in literature. An early case is the odd-even effect on the viscoelastic properties in nematic liquid crystal. Rotational viscosity of these liquid crystals exhibit alternation trend with alkyl chain length.[16–18] More recent molecular

dynamics (MD) simulation produced slight odd-even effects on rotational diffusion coefficients.[19] Another case is in several alkylimidazolium based and pyrrolidinium based ionic liquids, the viscosity also exhibits subtle odd-even trends with increasing alkyl chain length.[20–22] MD simulation predicted that the same trend goes with ion diffusion coefficient and electrical conductivity in these ionic liquids. [22,23] Santos et al. and Dupont et al. provided nanostructuration evidences in liquid phase regarding the structure-property relationship in imidazolium-based ionic liquid including dissociation energies, volatility and surface tension. [24–29] However, in both cases, the structural sensitivity of dynamic-related properties such as viscosity and vapor pressure is rather weak. In addition, the experimental measurement of dynamic properties at molecular level such as diffusion coefficient is still lacking.

Herein, we present the discovery of a clear dynamical odd-even effect in liquid state. We prepared a homologue of glass-forming ionic liquids by coupling stoichiometric di-ammonium alkyl cations and citrate anions. To study the odd-even effect with fine spatial and temporal resolution, we employed wide-angle neutron and synchrotron diffractions and quasi-elastic neutron scattering. We measured NIL series' microstructure by X-ray powder diffraction and local structure by neutron and X-ray Pair Distribution Function (PDF) analysis. Both results suggested very slight alternating trend in the local structures of the liquids. We found that the mean squared displacement exhibited an odd-even effect as a function of the alkyl backbone length in cation. The incoherent quasi-elastic neutron scattering measurements revealed significant odd-even effects in the dynamic properties such as the diffusion coefficient, the residence time, and the rotational relaxation time. The understanding of such sensitivity of dynamic properties over structures will motivate more fundamental studies on the structure-property relationship for molecular viscous flow. We also expect this work to be helpful for technological applications requiring novel materials with structural sensitivity.

All NILs under investigation were synthesized based on a previously reported procedure.[30–32] For brevity, these ionic liquids were named as "NIL n-m", where n was the number of methylene units in alkyl backbone and m was the number of methylene/methyl

units in side chains. We have chosen this excellent glass-forming liquid over common ionic liquids because the structural difference between glass and liquid state is minimal. For our work, we would like to demonstrate that huge differences in dynamics could result from slight difference in structure. With excessive structural frustration by the alkyl side chains in cation, the ionic network refused to crystalize upon cooling. Both n and m determined the NIL's glass transition temperature as a result of competition between the electrostatic and van der Waals forces.

As analyzed in Chapter 2 (Figure 2.1, 2.2), there is no alternating trend in NIL's microstructure, we decided to check whether the local structures of NILs could reveal any alternating trend. Pair Distribution Function (PDF) analysis using both synchrotron X-rays and neutrons gave local (r < 10 Å) structural information of atoms in NILs. Such local structural information is dominated by the intramolecular atomic correlations, although cross-correlations between molecules also contribute to the scattering signal. We collected PDF data in the liquid state at 300K (Figure 3.3). The local structures of NILs and their corresponding glass states were almost identical. The PDFs were very close with only slight difference on some peaks' height such as a decreased intensity of the first peak at 300K at 1.07 Å. For the X-ray PDF measurements, we used normal hydrogenated samples. Due to the negligible X-ray cross-sections of hydrogen atoms, the XPDF mainly revealed the C-C correlations with the prominent first two peaks at 1.55 Å and 2.7 Å. The scattering from the two N atoms in the cation is weak compared to the majority C atoms. The number of the nearest C-C neighbors (1.55 Å) was found to be larger for the odd-NILs than the even-NILs. However, such odd-even local structural differences can no longer be identified beyond the second nearest neighbor of C-C. In order to reveal the hydrogen ordering, we synthesized deuterated samples for the neutron PDF measurements. In addition to the C-C correlations similarly to what was observed in XPDF, the NPDF further revealed two prominent C-D correlations at 1.07 Å and 2.1 Å. On the contrary to C-C coordination number, the number of the first (1.07 Å) and second (2.1 Å) C-D neighbors was found smaller for the odd-NILs than the even-NILs. The alternating trend of C-C and C-D correlations revealed by PDF analysis indicate that weak odd-even effect of the molecular morphology exits in NILs. It is interesting to note that such local molecular morphology

differences is so weak that they do not translate into any long-range odd-even packing of the molecules, as evidenced in the previous XRD data.
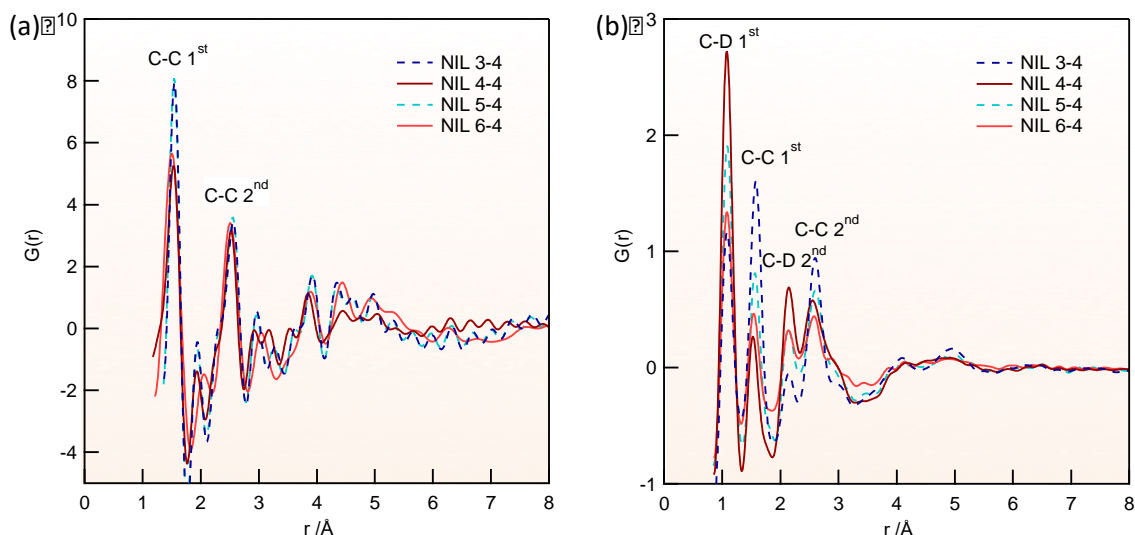
Figure 3.3 (a) X-ray Pair Distribution Function (PDF) of normal protonated sample NIL n-4 at 300K; (b) Neutron PDF of deuterated sample NIL n-4 at 300K. In both neutron and X-ray PDF, the number of C-C 1st neighbor of odd-NILs was larger than even-NILs; in neutron PDF, the number of C-D 1st neighbor of even-NILs was larger than odd-NILs. These odd-even local structural differences is hard to be identified beyond second nearest neighbor of C-C and C-D.

The molecular scale dynamics of the NILs was then investigated using Incoherent Elastic Neutron Scattering (IENS). We chose the butyl side chain (m=4) series for dynamic study because of the match of their dynamic features to the time window of the back scattering instrument.[33] Due to the exceptionally large incoherent cross section of hydrogen atoms, IENS probes the hydrogen motions. As most of the hydrogen atoms are in the cations, the measurement predominantly probed the motions of the cations. The measured intensity is proportional to the effective Debye-Waller factor $\exp\left(-\frac{1}{6}\langle r^2 \rangle Q^2\right)$ of the hydrogen atoms in the system, averaged over the nano-second time resolution window, which directly yields the hydrogen Mean Squared Displacement (MSD). As shown in Figure 3.4a, the measured temperature dependence of the MSD can be divided into three regimes: harmonic motion, side chain motion and, backbone motion. From 100K to 250 K, the first increase of MSD started to emerge. This increase of MSD is due to the rotational motion and confined segments motion in NILs. It is noticeable that the even-numbered NILs show larger MSD values than neighboring odd-numbered ones in this regime. Above
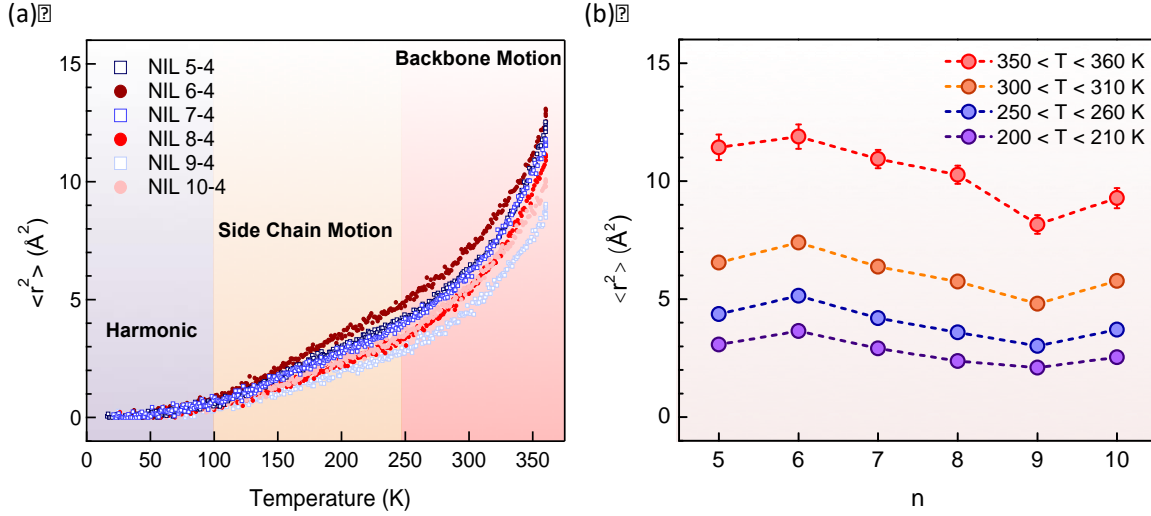
Figure 3.4 (a) The temperature dependence of the Mean Squared Displacement (MSD) of NIL series n-4 (n=5-10); (b) Average MSD of different temperature ranges as a function of the backbone repeating units showed a clear odd-even alternation. The alternating trend that even-NILs has larger MSD value than odd-NILs becomes clearer at higher temperature.

250K, the backbone motion dominated. The MSDs increased dramatically in this regime due to the diffusions of the whole ion. In this regime, larger differences between odd- and even-numbered cations are observed. We plot the average MSDs within four different temperature ranges (10 K for each range) as functions of the backbone repeating units n (Figure 3.4b). For the two higher temperature ranges, we observed more obvious odd-even effects on average MSD values than lower temperatures. Note that this dynamical odd-even effect was observed in liquid states in absence of any long-range order.

To take a step further, we measured the diffusional dynamics of NILs using Quasi Elastic Neutron Scattering (QENS) at 360K. The wave-vector transfer Q and energy transfer E dependence of the scattering intensity, basically the double differential cross section, is described by the Fourier transform of the self-intermediate scattering function:

$$I(Q, E) = N \cdot \mathcal{F}\{F_s(Q, t)\} \otimes R(Q, E) \qquad (3.1)$$

where N is the normalization factor, $F_s(Q,t)$ is the self-intermediate scattering function, and $R(Q,E)$ is the Q-dependent energy resolution function. The $F_s(Q,t)$ can be further decoupled as the product of the translational correlation function $F_T(Q,t)$ and the rotational correlation function $F_R(Q,t)$ of the hydrogens of the cations:

$$F_s(Q,t) = A(Q)F_T(Q,t)F_R(Q,t) \qquad (3.2)$$

where *A(Q)* represents the fast motions of the atoms that are outside the time window of the measurements and is fixed to be unity because of its coupling with the
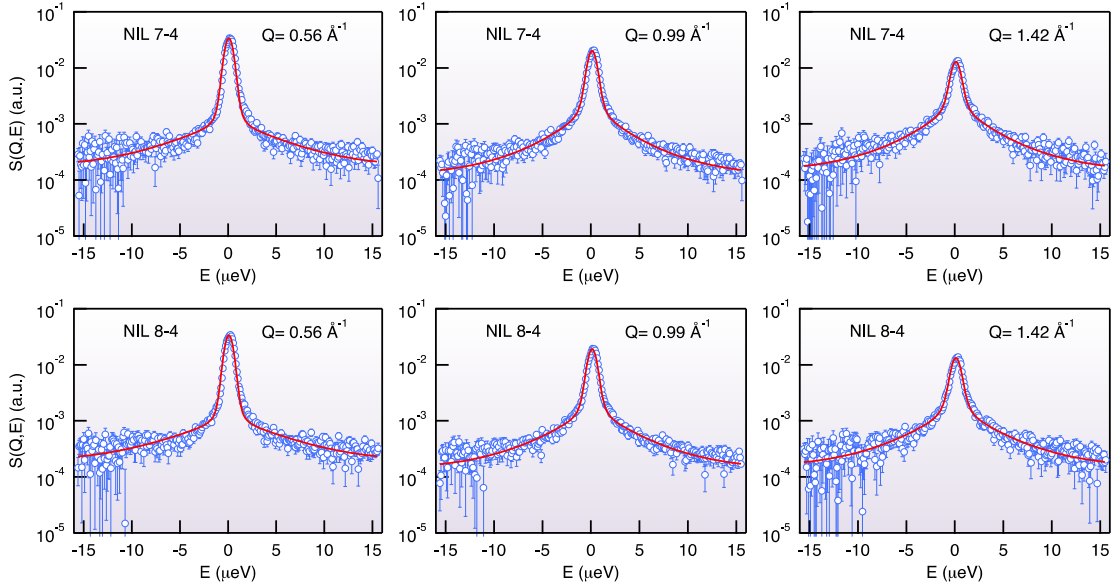
Figure 3.5 Quasi-Elastic Neutron Scattering (QENS) spectra of samples NIL 7-4 and NIL 8-4 at three representative Q values. Red lines represented the fits with the translational random-jump-diffusion and rotational Sears expansion model. The model was able to capture the key features in the measured QENS spectra in all Q ranges and fit all data remarkably well.

normalization factor *N*. $F_T(Q,t)$ represents the contribution from the translational diffusion. For simple liquid, it can be described by the random-jump-diffusion model:

$$F_T(Q,t) = \exp\left(-\frac{t}{\tau_T}\right)$$

$$\frac{1}{\tau_T} = \frac{DQ^2}{1+DQ^2\tau_0} \qquad (3.3)$$

where *D* is the translational diffusion coefficient and τ_0 is the residence time between random jumps of particles. [34]

$F_R(Q,t)$ represents the rotational diffusion of a molecule. Its *Q* and *t* dependence can beseparated by the Sears expansion.[35] Here we terminate the expansion at the first three terms because the higher-order terms are negligible in our experimental *Q* range. Thus, the expression for $F_R(Q,t)$ is as follows:

$$R(Q,t) = j_0^2(Qa) + 3j_1^2(Qa) \exp\left[-\frac{t}{3\tau_R}\right] + 5j_2^2(Qa)\exp\left[-\frac{t}{\tau_R}\right] \tag{3.4}$$

where a stands for the radius of the rotation, τ_R is the relaxation time associated with the rotational diffusion, $j_n(x)$ are the spherical Bessel functions.
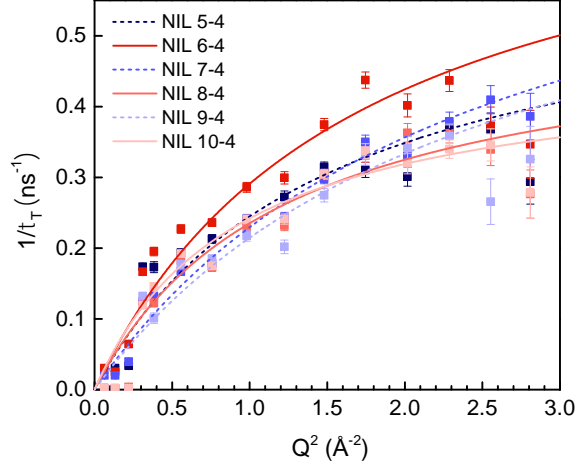
Figure 3.6 The translational broadening linewidth $1/\tau_T$ as function of Q^2. The trend can be described by the random-jump-diffusion model: $\frac{1}{\tau_T} = \frac{DQ^2}{1+DQ^2\tau_0}$. The trend of linewidth showed an initial linear region whose slope yielded the diffusion coefficient D, and then it flattened out to a constant value given by the inverse of random-jump-diffusion residence time τ_0.
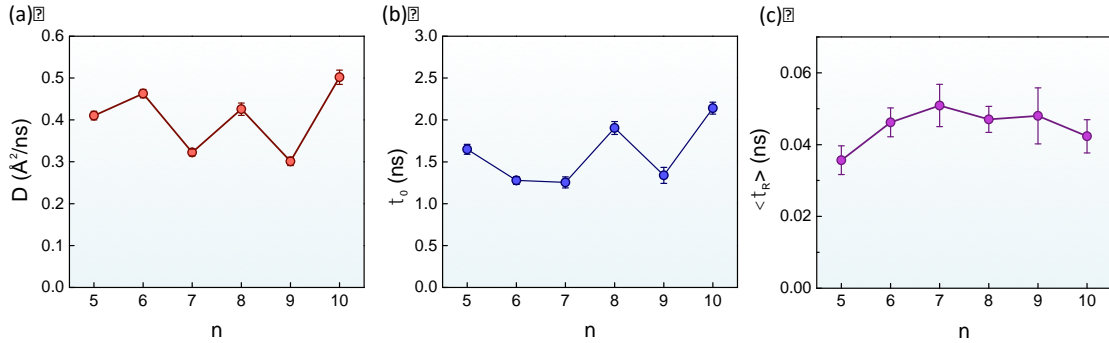
Figure 3.7 (a) Diffusional coefficient D; (b) random-jump-diffusion residence time τ_0 ; and (c) rotational relaxation time τ_R as functions of backbone repeating units n.

Demonstrations of the fittings of the QENS spectra of two samples NIL 7-4 and NIL 8-4 with the above-described model were illustrated in Figure 3.5. The model was able to capture the key features in the measured QENS spectra in all Q ranges and fit all data remarkably well with three parameters: the diffusional relaxation time τ_T (which further

yields the diffusion coefficient D and the residence time τ_0), the rotational relaxation time τ_R, and the rotational radius a.

For the translational motion, the diffusion coefficient D exhibited great sensitivity on NIL's odd-even structural units. We plotted the linewidth of the translational component $1/\tau_T$ of the spectrum as a function of Q^2 (Figure 3.6). For all samples, the trend of linewidth showed an initial linear region with Q whose slope yielded the diffusion coefficient D, and at higher Q values it flattened out to a plateau which defines random-jump-diffusion residence time τ_0. As shown in Figure 3.6a, the translational diffusion coefficient D exhibited a remarkable odd-even trend as a function of the backbone repeating units n of the cation. The odd-numbered cations showed significantly smaller diffusion coefficients than the neighboring even-numbered ones. This observation was consistent with, yet more
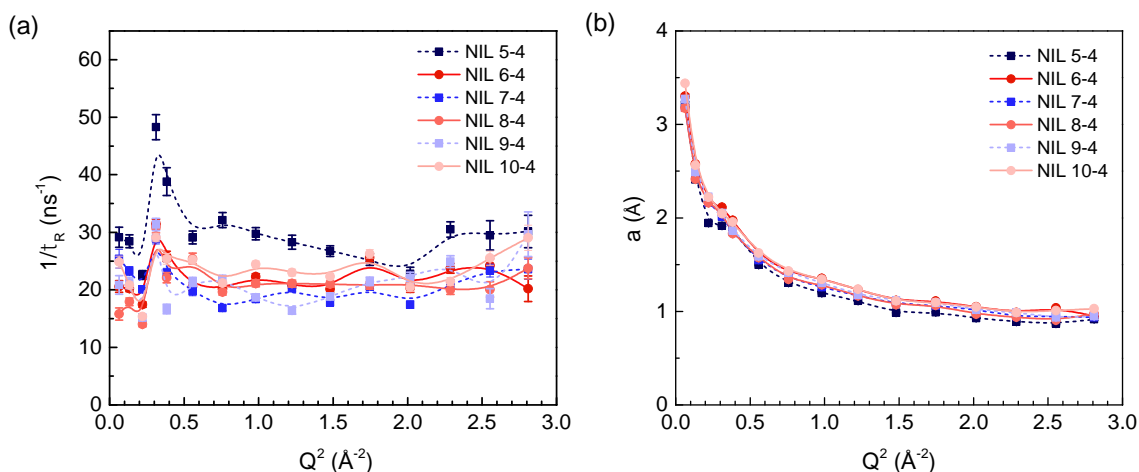
Figure 3.8 Rotational contribution can be described by the Sears expansion, we terminate the expansion at the first three terms because higher terms are negligible in our experimental Q range: $F_R(Q,t) = j_0^2(Qa) + 3j_1^2(Qa)\,exp\left[-\dfrac{t}{3\tau_R}\right] + 5j_2^2(Qa)exp[-\dfrac{t}{\tau_R}].$ *(a) the broadening linewidth $1/\tau_R$ as function of Q^2, the τ_R is almost independent of Q in most of the Q value; (b) the rotation radius a as function of Q^2, the a goes to around 1Å at higher Q, which corresponds to the C-H bond distance.*

striking than, the MSD trend, described previously. The largest difference of neighboring odd- and even-numbered NILs was between NIL 9-4 and NIL 10-4. With one additional methylene unit, the diffusion coefficient differed by almost a factor of two. For the residence time τ_0 (Figure 3.7b), there's also a similar alternation trend (except for the case n=6, which may be due to the uncertainties in the measurements and analysis). The general

trend was that even-numbered cations showed a longer residence time between jump-diffusion events.

Further analysis of the rotational motion also reveals a similar odd-even effect. From the rotational contribution $R(Q,t)$, two essential parameters can be extracted: the
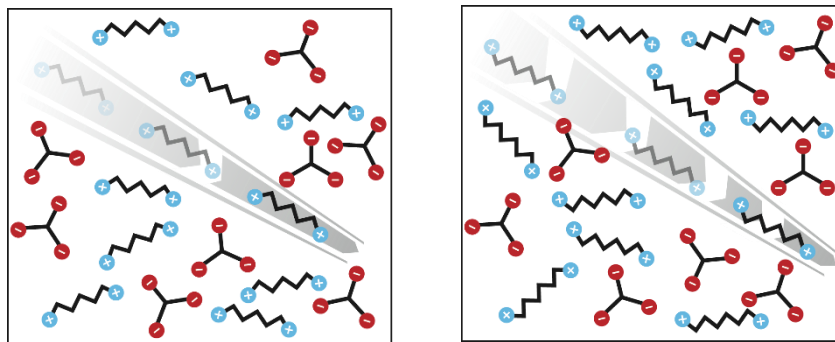
Figure 3.9 Schematic depiction of dynamic odd-even effect of NILs: odd-NILs cation (left) move slower than even-NILs (right). Dynamic properties such as translational diffusional coefficient, residence time and relaxation time showed sensitivity on backbone repeating units n.

radius of the rotation a and the rotational relaxation time τ_R. All samples exhibited similar trends of correlation between rotation radius a, and wave-vector transfer Q: a decreased in low Q regime ($Q < 0.75$ Å^{-1}) and flattened out to about 1 Å, which corresponded to the C-H distance (Figure 3.8a). For all NIL samples, the rotational relaxation time τ_R was almost independent of Q, especially in the range of $0.56 < Q^2 < 2.81$ Å^{-2} (Figure 3.8b). Interestingly, the mean rotational relaxation time $<\tau_R>$ over the measured the Q range also showed an odd-even trend towards backbone repeating units n (Figure 3.9).

Without noticeable packing differences, the diffusion coefficient and residence time of NIL changes significantly with addition of only one methylene group (Figure 5d,e). This extent of structural sensitivity on dynamical properties is surprising given the absence of long-range order in liquid state. Therefore, such observation challenges the conventional understanding of the odd-even effect in terms of molecular packing. Our results suggest that single molecular morphology, although subtle as shown in the local pair distribution functions, could still result in striking macroscopic dynamic differences. Understanding the principles governing this structure-property is important to the design and synthesis of responsive materials. Such molecular structural sensitivity of dynamics is reminiscent of a

glass transition process, where the transport properties of molecules change by several orders of magnitude while the differences between intermolecular structures can hardly be appreciated. The dynamical odd-even effect could also provide new insight into molecular viscous flow.

In summary, we discovered a dynamic odd-even effect in liquids. The microstructure analysis by powder XRD showed similar arrangements of molecular ions for the homolog of ionic liquids. However, PDF analysis by neutron and X-ray reveal that the molecular morphology exhibits weak alternating trend as function of repeating methylene units. The elastic neutron scattering suggests that the odd-even trend of nanosecond MSD as function of n is very clear at high temperature. Further QENS measurements conducted in liquid state confirms the odd-even trends exist in diffusion coefficient of translational motion, residence time, and rotational motion. Such great sensitivity of dynamical properties on the repeating methylene units in cations is very intriguing. Studies of this structure-dynamic relationship will further bridge the understanding of molecular structures and properties of liquids.

3.5 Odd-even effect of diffusional coefficient in n-alkane

n-alkane (C_nH_{2n+2}), one of the principal components of gasoline, is perhaps the best-known example of a substance exhibiting an intriguing "odd-even effect".[2] Namely, for a wide range of carbon atom numbers, solid n-alkanes with even numbers of carbon atoms have higher densities and melting points than those of the average of the two odd number neighbors. Therefore, the density and the melting point curves of solid n-alkane as functions of the number of carbon atoms show an interesting sawtooth shape (Figure 3.10). The phenomenon was first discovered in 1877, however, it wasn't explained rigorously until more than a century later. [1,2] Nowadays, the standard textbook explanation of the "odd-even effect" is that solid n-alkanes with even numbers of carbon atoms pack better into ordered periodic crystalline structures, so they have higher densities and melt at higher temperatures; while n-alkane with odd numbers of carbon atoms do not pack as well, and thus their densities are lower and lower temperatures are needed to melt them. [36] However,

a more fundamental understanding of what determines the packing efficiencies of *solid n-alkanes* and whether "odd-even effects" also exist in *liquid n-alkanes* are not known to date.

Ultimately, the packing of molecules in the liquid state is determined by the molecular structures and interactions. Although the ordered periodic packing is not as well defined in liquid state as in the liquid state, the molecular structures and interactions still depend on the odd-even variation of chain length of the n-alkane molecules. According to this logic, we hypothesize that the odd-even variation of the chain length of n-alkane molecules will also cause *odd-even effects in the liquid state*. Such odd-even effects in the liquid state may be subtle in the thermodynamic and structural quantities because of the transient nature of liquid local structures; however, they will be manifested in the dynamical and transport properties, in a similar way that the glass transition occurs without presence of any strong evidence of any structural changes.

In 1877, A. Baeyer discovered that the melting point of fatty acids does not exhibit a monotonic increase with increasing chain length as do their boiling points[1]. Instead, the even-members' melting point is relatively higher than the odd-members. The longer the chain length, the smaller are the relative differences. This holds for the n-alkanes and also most of its α- and α,ω-substituents. In Figure 1a, the melting points and boiling points of n-alkanes from ethane (n=2) to nonane (n=9) are plotted as functions of the number of carbon atoms n. The melting points show an alternative trend while the boiling points do not. Other physical properties, such as sublimation enthalpy and solubility, which are related to the liquid state, also display similar alternations (odd-even effect). [4,37]

Today in most organic chemistry textbooks, the odd-even effects of n-alkane on their melting points are described and explained by the so-called "packing effects". [36]However, what exactly is the difference between the packing of odd- and even-number n-alkane was not shown until 1999. [2] With the help of single crystal diffraction and computer controlled crystal growing device, the lattice constant of n-alkanes were obtained.
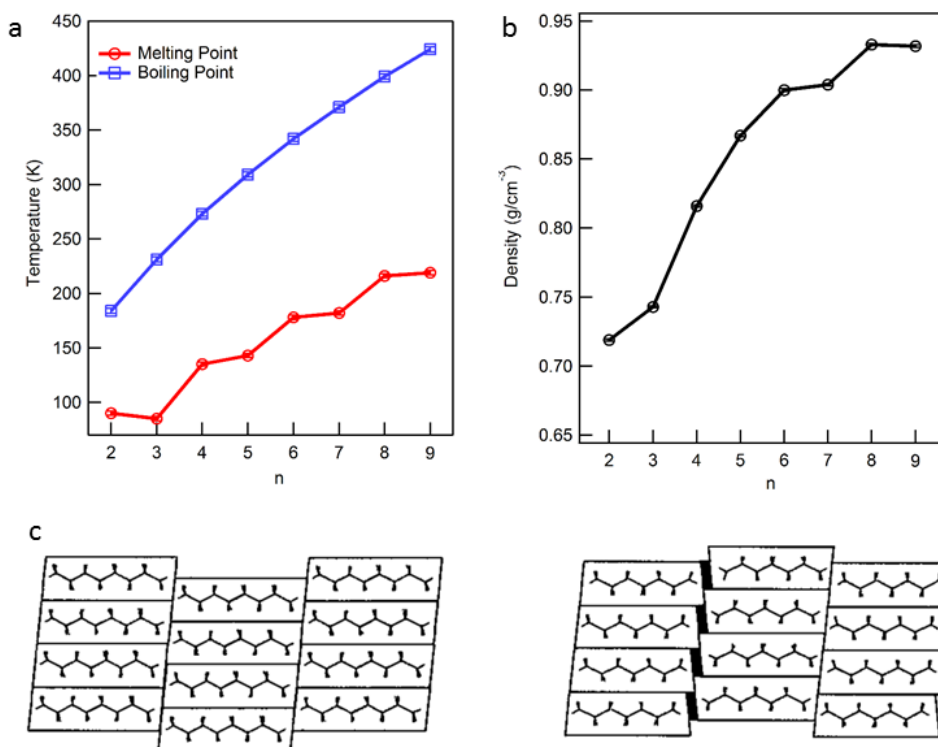
Figure 3.10 Odd-even Effect in Solid n-Alkanes (a) The melting points and boiling points of n-alkanes as function of the number of carbon atoms n=2-9; (b) the density of n-alkanes at -183 °C as function of n; (c) single crystal diffraction experiment indicates that the difference of packing between even-number (left) and odd-number (right) n-alkanes [taken from[2]]. n-Alkanes with even numbers of carbon atoms pack better into ordered periodic crystalline structures, so they have higher densities and they melt at higher temperatures; while n-alkane with odd numbers of carbon atoms do not pack as well, and thus their densities are lower and lower temperatures are needed to melt them. [2]

Then the densities of crystalline n-alkanes can be readily calculated and were found to exhibit an odd-even trend as well, shown in Figure 3.10b. It was discovered that the intermolecular distances between the end groups, namely, the CH_3 groups, are responsible for the alternation in the densities and melting points (Figure 3.10c). Basically, n-alkanes with even numbers of carbon atoms pack better into ordered periodic crystalline structures,

so they have higher densities and they melt at higher temperatures; while n-alkane with odd numbers of carbon atoms do not pack as well, and thus their densities are lower and lower temperatures are needed to melt them. Thereafter, the "packing effects" are used to explain the odd-even effects of the physical properties in liquid state.

Keeping in mind the fascinating odd-even effects of solid n-alkane, it is natural to ask whether such odd-even effects also exist in the liquid state. For instance, at room temperature, the density of n-alkanes only shows a monotonic trend as a function of the number of carbon atoms n (Figure 3.11a); while the viscosity of n-alkanes also shows a monotonic trend at different temperatures. [38,39] Therefore, superficially it seems that the odd-even effects do not exist in the liquid state, which sort of make sense since the periodic packing is not well defined in liquids. [40,41] However, these data are obtained and plotted at the same temperatures, which are much higher than their corresponding melting points. Then the odd-even effect may not show up simply because of the large thermal activations. In the end, the addition of CH_2 group will still affect the intermolecular distances between the end groups and the molecular structures in the liquids. Therefore, it is worth further
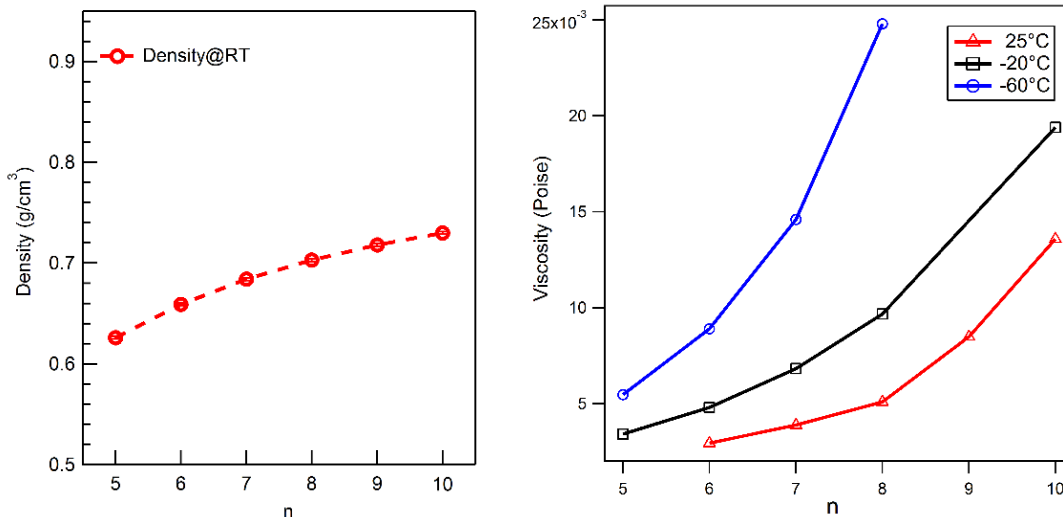
Figure 3.11 Density and Viscosity of Liquid n-Alkane at Constant Temperatures (No Obvious Odd-Even Effect at Constant Temperature Cut). (a) Density of liquid n-alkanes at room temperature; [49,50] (b) viscosity of liquid n-alkanes at selected temperatures. No odd-even effect is seen at such constant temperature cuts[38]. [density data taken from NIST fluid database]

investigating the physical properties of liquid n-alkanes near their respective melting points.

We hypothesize that this extra CH_2 group will still cause an alternative trend of certain properties in liquid state.
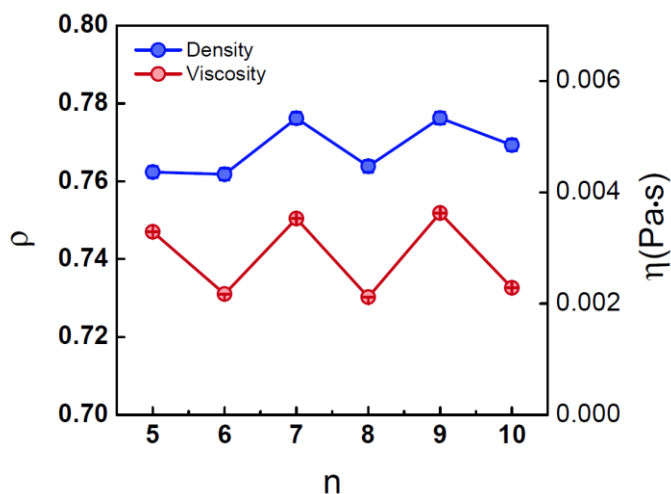
Figure 3.12 The density and viscosity of n-alkanes at their respective melting points.

To compare the basic thermodynamic properties of n-alkanes near their melting point, we have plotted their density and viscosity near melting temperature. We have set a temperature set that is always 3K above individual n-alkane's melting point. This temperature set is chosen to decouple the melting temperature odd-even effect with n-alkane's own dynamic properties. The data is calculated using NIST Thermophysical Properties of Fluid System. (Figure 3.12) Surprisingly we observed an odd-even effect for n-alkanes from pentane to decane. The fluctuation of density and viscosity is very subtle with difference less than 0.02g/mL and 0.002 Pa*s. However, the odd-even trend is clearly shown. This provides a strong indication that the dynamic properties at molecular level may have an odd-even effect in liquid state as well, which prompts us to carry out the QENS experiment to measure the microscopic dynamic properties.

High-resolution incoherent QENS technique benefits from the exceptionally large incoherent cross section of hydrogen atoms, and thus is very suitable to study single-particle self-motion with a sub-picosecond resolution. A diversity of dynamic processes, spanning from various fast segments relaxations to relatively slower translational and rotational diffusion, exist in n-alkane system. [42–45] In comparison to bulk quantities, the

microscopic dynamic properties directly reflect the subtle differences between individual n-alkanes in the series. [46]

Our QENS measurements using the DCS spectrometer at NIST Center for Neutron Research are shown in Figure 3.13. We chose the incident neutron wavelength to be 8Å, which provided an elastic energy resolution about 30 meV FWHM. Again we measured QENS spectra slightly (3K) above each n-alkane's individual melting point (T_m +3K). This temperature set is chosen to decouple the melting temperature odd-even effect with n-alkane's own dynamic properties and make sure that the n-alkanes stays in liquid state through the data acquisition process (about 6h per sample).

The wave-vector transfer Q and energy transfer E dependence of the scattering intensity, basically the double differential cross section, is described by the Fourier transform of the self-intermediate scattering function:

$$I(Q, E) = N \cdot \mathcal{F}\{F_s(Q, t)\} \otimes R(Q, E) \qquad (3.5)$$

where N is the normalization factor, $F_s(Q,t)$ is the self-intermediate scattering function, and $R(Q,E)$ is the Q-dependent energy resolution function. The $F_s(Q,t)$ can be further decoupled as the product of the translational correlation function $F_T(Q,t)$ and the rotational correlation function $F_R(Q,t)$ of the hydrogens of the cations:

$$F_s(Q, t) = A(Q)F_T(Q, t)F_R(Q, t) \qquad (3.6)$$

where $A(Q)$ represents the fast motions of the atoms that are outside the time window of the measurements and is fixed to be unity because of its coupling with the normalization factor N. $F_T(Q,t)$ represents the contribution from the translational diffusion. For glass-forming liquid, it can be described by the stretch exponential (KWW) model:

$$F_T(Q, t) = \exp\left[-\left(\frac{t}{\tau_T}\right)^\beta\right] \qquad (3.7)$$

64

where τ_T is the relaxation time and β is the stretch exponent.
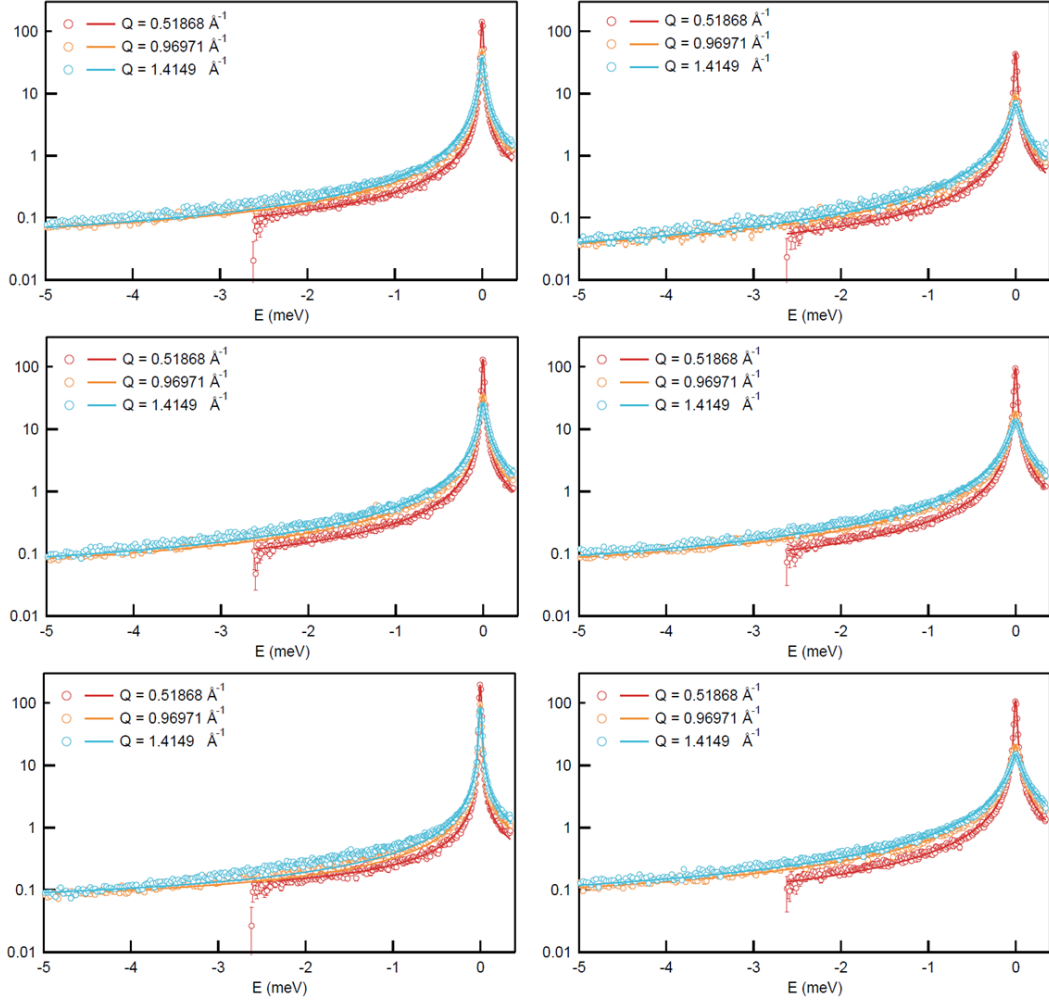
Figure 3.13 Quasi-Elastic Neutron Scattering (QENS) spectra of samples pentane, hexane, heptane, octane, nonane and decane at three representative Q values. Solid lines represented the fits with the translational stretched exponential model. The model was able to capture the key features in the measured QENS spectra in all Q ranges and fit all data remarkably well.

$F_R(Q,t)$ represents the rotational diffusion of a molecule. Its Q and t dependence can beseparated by the Sears expansion.[35] Here we terminate the expansion at the first three terms because the higher-order terms are negligible in our experimental Q range. Thus, the expression for $F_R(Q,t)$ is as follows:

$$R(Q,t) = j_0^2(Qa) + 3j_1^2(Qa) \exp\left[-\frac{t}{3\tau_R}\right] + 5j_2^2(Qa)\exp[-\frac{t}{\tau_R}] \quad (3.8)$$

where a stands for the radius of the rotation, τ_R is the relaxation time associated with the rotational diffusion, $j_n(x)$ are the spherical Bessel functions.

Actually when fitted with only translational contribution, the fittings looks remarkably well. Addition of rotational contribution only improves the fitting slightly at high Q value. Demonstrations of the fittings of the QENS spectra of all samples with only translational model were illustrated in Figure 3.13. The model was able to capture the key features in the measured QENS spectra in all Q ranges and fit all data with two parameters: the diffusional relaxation time τ_T, and the stretch exponent β.

The fitted parameters $1/\tau$ and stretch factor β were plotted as function of Q^2 (Figure 3.14). For $Q = 0.5$ Å^{-1}, the relaxation time τ for translational diffusion of n-alkanes is in the order of 10 ps. All even-number n-alkanes have smaller τ compared with odd-numbers. The difference in relaxation time is very large considering their structure difference is only one CH_2 group. Among odd-number n-alkanes, nonane has surprisingly slow dynamics even compared with pentane and heptane. Same trend was observed in β plot: even-number
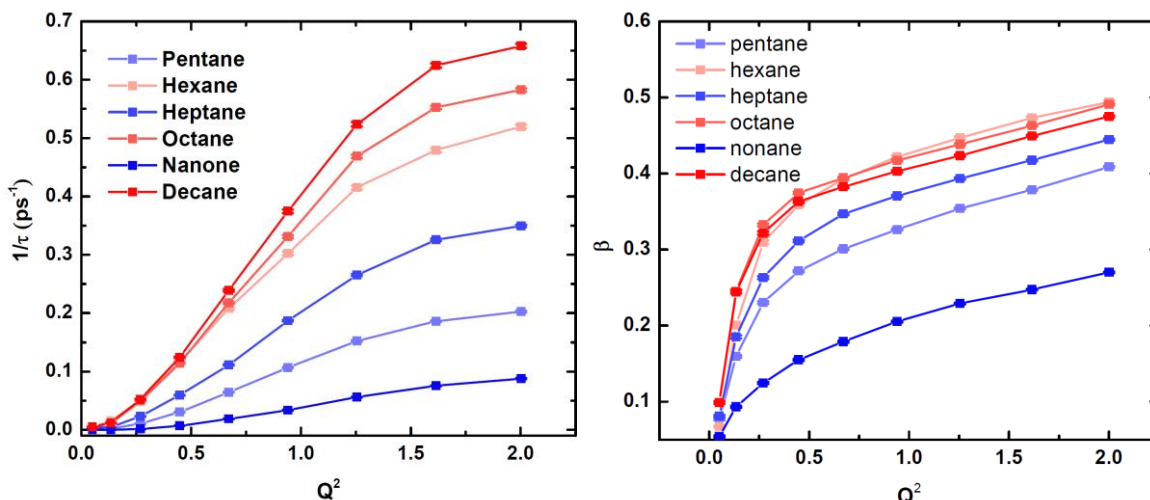
Figure 3.14 Q-dependence of the fitting parameters relaxation time 1/τ and stretch exponent β vs Q². Odd-numbered n-alkanes are plot in blue and even-numbered n-alkanes are plot in red. Both clearly show odd-even alternations as functions of the number of carbon atoms n.

n-alkanes have similar β at different Q while odd-number has much smaller β. The stretching exponent β is usually taken as a measure of heterogeneity in the system. Such a small value indicates a highly heterogeneous state of the system, which requires much more detailed modeling.
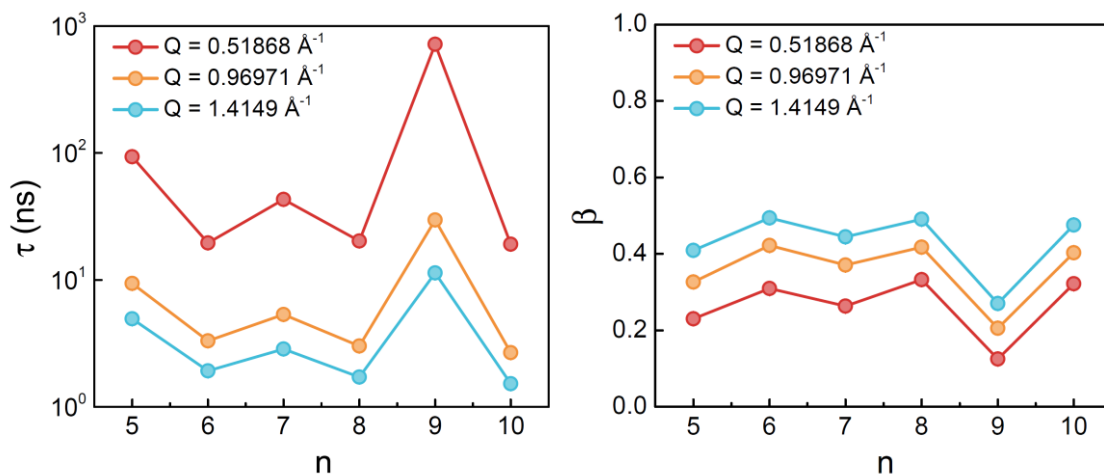
Figure 3.15 The extracted relaxation time τ of liquid n-alkane near their respective melting points as a function of the number of carbon atom in n-alkane clearly show the dynamic odd-even effect. Same trend can be observed for stretch exponent β as well. Three representative Q value are shown. Note that the left figure is plotted in semi-log scale, therefore the relaxation times between neighboring n-alkane differ by 10-50 times.

When we plot the extracted relaxation time τ and stretch exponent β as a function of carbon number n for all samples at three representative Q value (Figure 3.15), we can see a very clear trend of odd-even effect on the dynamics of n-alkanes. Combining the fact that all the data was acquired in liquid state near melting point, this is the first time that a dynamic odd-even effect is observed in n-alkanes. The odd-numbered n-alkane has longer relaxation time than their neighboring even-numbered species, which means that pentane, heptane and nonane moves much slower than hexane, octane and decane. It is very interesting that all even-numbered n-alkanes have very similar relaxation time near their melting point while odd-numbered n-alkane's relaxation time varies. The extreme case is nonane, which has much slower dynamics than either pentane or heptane. Despite the size of nonane is smaller than decane, the dynamics of nonane is 50 times slower than decane! This result is very surprising given the structural difference between nonane and octane is only one methylene group.

The stretch exponent β shows the similar trend as relaxation time. It is worthwhile to note here that unlike common expectation that n-alkane is far away from a very jammed system because of its low viscosity, the stretch exponent is pretty low near their melting point with the all the samples.

3.6 Experimental section

3.6.1 Quasi-elastic neutron scattering (QENS) experiment

The QENS experiment was carried out using the High Flux Back Scattering (HFBS) instrument at NIST Center for Neutron Scattering (NCNR). Thin layer of samples were loaded into cylindrical aluminum containers. Helium glove box was used in order to avoid moisture and enhance heat conductivity. The sample cans were sealed using indium wires. The sealed sample container was then mounted in a top-loading closed-cycle refrigerator (CCR) with temperature accuracy better than 0.1 K. The nominal incident neutron wavelength was 6.271 Å (2.08 meV in energy). The instrument was firstly operated in the fix-window mode, i.e., the Doppler drive was stopped. In this mode, only the elastically scattered neutrons were detected. The temperature was continuously ramped up from 15 K to 363 K with a heating rate of 1 K/min.

After the fix-window scan, the instrument was operated at dynamic-window mode, where the Doppler drive was operated in such a way to provide an energy transfer range of ± 17 μeV, a wave-vector transfer Q range of 0.25-1.75 $Å^{-1}$. The energy resolution near the elastic line was about 1 μeV. All quasi-elastic measurements were taken at 360 K, where all samples were in the liquid phases. Vanadium run was used for detector calibration and instrument resolution.

The elastic scattering intensity is normalized by the base temperature measurement at each wave vector transfer Q. The normalized elastic intensity $\overline{I_T}(Q, E = 0)$ can be expanded as a function of Q^2:

$$\overline{I_T}(Q, E = 0) = \frac{I_T(Q,E=0)}{I_{T_0}(Q,E=0)} = \exp\left(-\langle x^2 \rangle Q^2 + \frac{1}{2}\alpha_2(\langle x^2 \rangle Q^2)^2 + \cdots\right) \qquad (3.9)$$

where $\langle x^2 \rangle = \frac{\langle \Delta r^2 \rangle}{6}$ is the mean squared displacement (MSD) and $\alpha_2 = \frac{3\langle x^4 \rangle}{5\langle x^2 \rangle^2} - 1$ is the dimensionless non-Gaussian parameter. In the low Q limit, the above equation is reduced to:

$$\lim_{Q \to 0} \overline{I_T}(Q, E = 0) = \exp(-\langle x^2 \rangle Q^2) \qquad (3.10)$$

Therefore, the elastic incoherent scattering intensity basically measures the effective Debye-Waller factor. If we plot $-\ln \overline{I}$ vs. Q^2, the slope would be $\langle x^2 \rangle$ (Figure
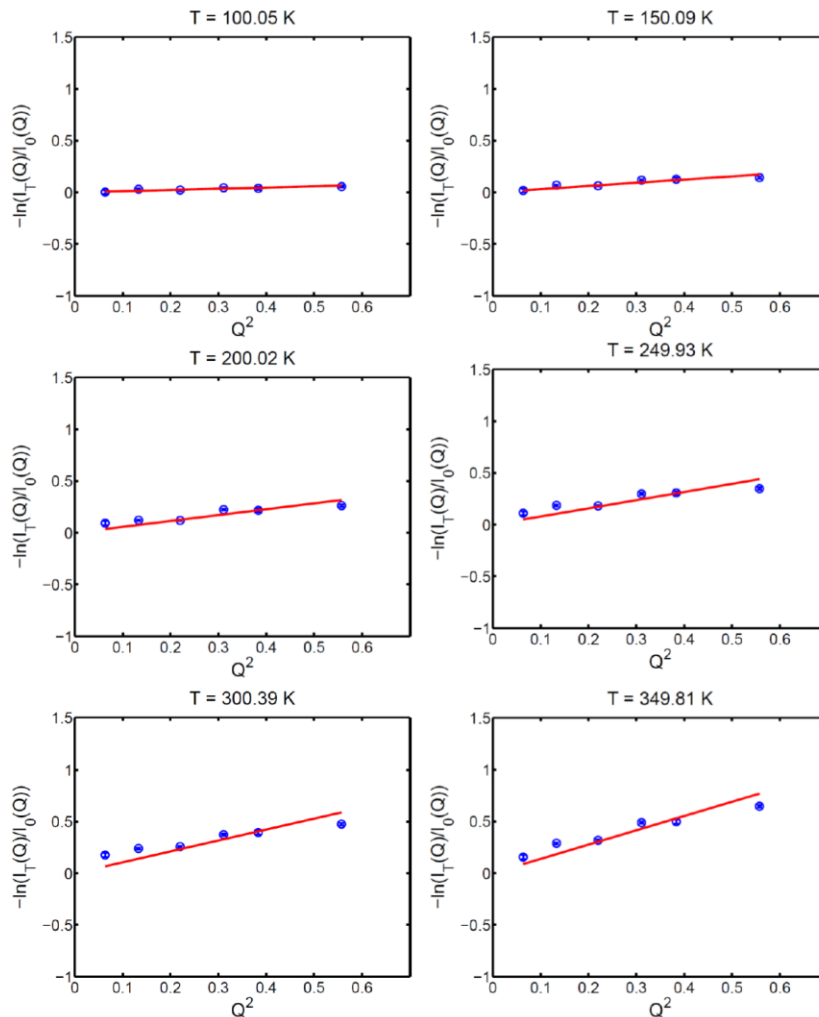
Figure 3.16 Normalized intensity $ln(I_T(Q)/I_0(Q))$ as a function of Q^2 in the low Q limit at representative temperatures for sample IG 5-4. Red lines indicate the fits. (Copyright © 2014 American Chemical Society)

3.16). Note that the instrument has finite energy resolution $R(E)$, which has a Gaussian shape, so the measured intensity is averaged over the instrument resolution window:

$$\overline{I}\big(Q, E = 0, R(t)\big) = \frac{\int_{-\infty}^{\infty} S(Q,E)R(E)dE}{\delta(E)R(E)dE} = \frac{\int_0^{\infty} F(Q,t)R(t)dt}{\int_0^{\infty} R(t)dt} \qquad (3.11)$$

Therefore, the mean squared displacement is also averaged over the instrument resolution window.

$$\langle x^2 \rangle = \frac{\int_0^{\infty} \langle x^2(t) \rangle R(t)dt}{\int_0^{\infty} R(t)dt} \qquad (3.12)$$

The temperature dependence of the mean squared displacement is shown in Figure 3.17.
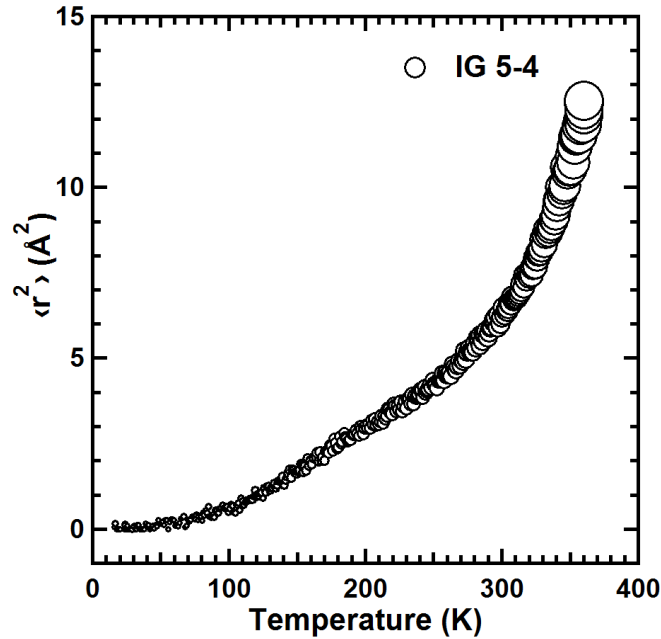
Figure 3.17 The averaged mean squared displacement ‹x²› of the hydrogen atoms of IG 5-4 extracted from elastic scan with an energy resolution of 0.85 µeV using the HFBS spectrometer at NCNR. The size of the point indicates the standard deviation error bar of ‹x²› evaluated from the nonlinear least square fitting. (Copyright © 2014 American Chemical Society)

3.6.2 X-ray and neutron pair distribution function (PDF) experiment

The X-ray PDF experiment was conducted at beam line 11-ID-B of the Advanced Proton Source (APS) at Argonne National Laboratory (ANL) with an incident x-ray energy

of 58.66 keV. The samples were settled inside Kapton capillaries and sealed with epoxy. The samples were aligned both in horizontal and vertical directions within the X-ray beam. The measurements were carried out at room temperature in ambient conditions. The scattering structure factor, with corrections for background scattering, X-ray transmission, and Compton scattering, was obtained from the diffraction data using the PDFgetX2 software package. [47]

The neutron PDF experiment was conducted at the Nanoscale-ordered Materials Diffractometer (NOMAD) beam line of the Spallation Neutron Source (SNS) at Oak Ridge National Laboratory (ORNL).[48] Deuterated samples were used to reduce the incoherent scattering from hydrogen.   The samples were sealed inside 3mm quartz capillaries. The room temperature measurement took about 0.5 h to obtain high resolution PDF.

3.7 References

(1)   Baeyer, A. *Ber. Dtsch. Chem. Ges* **1877**, *10*, 1286–1288.

(2)   Boese, R.; Weiss, H.; Blaser, D. *Angew. Chem. Int. Ed.* **1999**, *38*, 988–992.

(3)   Morishige, K.; Kato, T. *J. Chem. Phys.* **1999**, *111*, 7095.

(4)   Badea, E.; Gatta, G. Della; D'Angelo, D.; Brunetti, B.; Rečková, Z. *J. Chem. Thermodyn.* **2006**, *38*, 1546–1552.

(5)   Mukherjee, G.; Biradha, K. *Cryst. Growth Des.* **2011**, *11*, 924–929.

(6)   Jeong, Y. G.; Jo, W. H.; Lee, S. C. *Polymer (Guildf).* **2004**, *45*, 3321–3328.

(7)   Shiotani, A.; Kohda, M. *J. Appl. Polym. Sci.* **1999**, *74*, 2404–2413.

(8)   Tao, F.; Bernasek, S. L. *Chem. Rev.* **2007**, *107*, 1408–1453.

(9)   Craig, A. a.; Imrie, C. T. *Macromolecules* **1999**, *32*, 6215–6220.

(10)   Mary, L. J. F.; Kannan, P. *J. Polym. Sci., Part A Polym. Chem* **1999**, *37*, 1755–1761.

(11)   Debenedetti, P. G.; Stillinger, F. H. *Nature* **2001**, *410*, 259–267.

(12)   Chandler, D. *Proc. Natl. Acad.* **2009**, *106*, 15111–15112.

(13)   Angell, C. A. *Science* **1995**, *267*, 1924–1935.

(14)   Hägele, C.; Wuckert, E.; Laschat, S.; Giesselmann, F. *Chemphyschem* **2009**, *10*, 1291–1298.

(15)   Wolfgang Doster, Stephen Cusack, W. P. *Nature* **1989**, *337*, 754–756.

(16)   Chen, F.-L.; Jamieson, A. M. *Macromolecules* **1993**, *26*, 6576–6582.

(17)   Buchecker, R.; Schadt, M. *Mol. Cryst. Liq. Cryst.* **1987**, *149*, 359–373.

(18)   Bock, F.-J.; Kneppe, H.; Schneider, F. *Liq. Cryst.* **1986**, *1*, 239–251.

(19)   Capar, M.; Cebe, E. *Phys. Rev. E* **2006**, *73*, 061711.

(20)   Rocha, M. A. A.; Neves, C. M. S. S.; Freire, M. G.; Russina, O.; Triolo, A.; Coutinho, J. A. P. C.; Santos, L. M. N. B. F. *J. Phys. Chem. B* **2013**, *117*, 10889–10897.

(21)   Martins, M. A. R.; Neves, C. M. S. S.; Kurnia, K. A.; Carvalho, P. J.; Rocha, M. A. A.; Santos, L. M. N. B. F.; Pinho, S. P.; Freire, M. G. *Fluid Phase Equilib.* **2015**, *407*, 188–196.

(22)   Leys, J.; Wübbenhorst, M.; Preethy Menon, C.; Rajesh, R.; Thoen, J.; Glorieux, C.; Nockemann, P.; Thijs, B.; Binnemans, K.; Longuemart, S. *J. Chem. Phys.* **2008**, *128*, 064509.

(23)   Zheng, W.; Mohammed, A.; Hines, L. G.; Xiao, D.; Martinez, O. J.; Bartsch, R. A.; Simon, S. L.; Russina, O.; Triolo, A.; Quitevis, E. L. *J. Phys. Chem. B* **2011**, *115*, 6572–6584.

(24)   Rocha, M. A. A.; Coutinho, J. A. P.; Santos, L. M. N. B. F. *J. Chem. Phys.* **2013**, *139*, 104502.

(25)   Vilas, M.; Rocha, M. A. A.; Fernandes, A. M.; Tojo, E.; Santos, L. M. N. B. F. *Phys. Chem. Chem. Phys.* **2015**, *17*, 2560–2572.

(26)   Almeida, H. F. D.; Freire, M. G.; Fernandes, A. M.; Lopes-da-Silva, J. A.; Morgado,

P.; Shimizu, K.; Filipe, E. J. M.; Canongia Lopes, J. N.; Santos, L. M. N. B. F. L. M. N. B. F.; Coutinho, J. A. P. *Langmuir* **2014**, *30*, 6408–6418.

(27) Rocha, M. A. A.; Lima, C. F. R. A. C.; Gomes, L. R.; Schröder, B.; Coutinho, J. A. P.; Marrucho, I. M.; Esperança, J. M. S. S.; Rebelo, L. P. N.; Shimizu, K.; Lopes, J. N. C.; Santos, L. M. N. B. F. *J. Phys. Chem. B* **2011**, *115*, 10919–10926.

(28) Dupont, J. *J. Braz. Chem. Soc.* **2004**, *15*, 341–350.

(29) Consorti, C. S.; Suarez, P. A. Z.; De Souza, R. F.; Burrow, R. A.; Farrar, D. H.; Lough, A. J.; Loh, W.; Da Suva, L. H. M.; Dupont, J. *J. Phys. Chem. B* **2005**, *109*, 4341–4349.

(30) Wathier, M.; Grinstaff, M. W. *J. Am. Chem. Soc.* **2008**, *130*, 9648–9649.

(31) Aboudzadeh, M. A.; Muñoz, M. E.; Santamaría, A.; Fernández-Berridi, M. J.; Irusta, L.; Mecerreyes, D. *Macromolecules* **2012**, *45*, 7599–7606.

(32) Yang, K.; Tyagi, M.; Moore, J. S.; Zhang, Y. *J. Am. Chem. Soc.* **2014**, *136*, 1268–1271.

(33) Meyer, A.; Dimeo, R. M.; Gehring, P. M.; Neumann, D. A. *Rev. Sci. Instrum.* **2003**, *74*, 2759–2777.

(34) Singwi, K. S.; Sjölander, A. *Phys. Rev.* **1960**, *119*, 863–871.

(35) Sears, V. F. *Can. J. Phys.* **1967**, *45*, 237–254.

(36) Wade, L. G. *Organic Chemistry*; Prentice Hall, 2012.

(37) Rocha, M. a a; Coutinho, J. a P.; Santos, L. M. N. B. F. *J. Phys. Chem. B* **2012**, *116*, 10922–10927.

(38) Hirst, L. L.; Corporation, M. *Ind. Eng. Chem.* **1949**, *41*, 2067–2069.

(39) Yoo, C. Do; Kim, S.; Lee, S. H. **2008**, *29*, 1059–1062.

(40) Eyring, H. *J. Chem. Phys.* **1936**, *4*, 283.

(41)   Kauzmann, W.; Eyring, H. *J. Am. Chem. Soc.* **1940**, *62*, 3113–3125.

(42)   Kowert, B. A.; Sobush, K. T.; Fuqua, C. F.; Mapes, C. L.; Jones, J. B.; Zahm, J. A. **2003**, 4790–4795.

(43)   von Meerwall, E.; Beckman, S.; Jang, J.; Mattice, W. L. *J. Chem. Phys.* **1998**, *108*, 4299.

(44)   Feng, H.; Gao, W.; Nie, J.; Wang, J.; Chen, X.; Chen, L.; Liu, X.; Lüdemann, H.-D.; Sun, Z. *J. Mol. Model.* **2013**, *19*, 73–82.

(45)   Morhenn, H.; Busch, S.; Unruh, T. *J. Phys. Condens. Matter* **2012**, *24*, 375108.

(46)   Yu, Y.; Gao, G. **2000**.

(47)   Qiu, X.; Thompson, J. W.; Billinge, S. J. L. *J. Appl. Cryst.* **2004**, *37*, 678.

(48)   Neuefeind, J.; Feygenson, M.; Carruth, J.; Hoffmann, R.; Chipley, K. K. *Nucl. Instruments Methods Phys. Res. B* **2012**, *287*, 68–75.

(49)   Span, R. *Multiparameter Equations of State - An Accurate Source of Thermodynamic Property Data*; Springer, Berlin, 2000.

(50)   Starling, K. E. *Fluid Thermodynamic Properties for Light Petroleum Systems*; Gulf Publishing Company, Houston, Texas, 1973.

CHAPTER 4

APPLICATION OF NETWORK-FORMING IONIC LIQUIDS IN SHOCKWAVE ABSORPTION APPLICATION

4.1 Abstract

Understanding shockwave-induced physical and chemical changes of impact-absorbing materials is an important step toward the rational design of materials that mitigate the damage. In this work, we report a series of network-forming ionic liquids (NILs) that possess an intriguing shockwave absorption property upon laser-induced shockwave. Microstructure analysis by X-ray scattering suggests nano-segregation of alkyl side chains and charged head groups in NILs. Further post-shock observations indicate changes in the low Q region implying that the soft alkyl domain in NIL plays an important role in absorbing shockwaves. Interestingly, we observe a shock-induced ordering in the NIL with longest hexyl side chain, indicating that both nano-segregated structure and shock-induced ordering contribute to NIL's shockwave absorption performance.

4.2 Introduction

Shockwave dissipation materials function to protect personnel and structures from blast overpressure. During shockwave propagation, the brain is especially susceptible to shockwave overpressure. Previous studies have revealed that when brain tissues are exposed to high-intensity shockwaves greater than 10 MPa, severe hemorrhage is possible. Exposure to low-intensity shockwaves less than 1MPa also cause minor morphological changes in neurons, leading to mild-to-moderate traumatic brain injury (mTBI).[1] The human resourse loss from mTBI have significant direct economic impact and indirect costs due to loss of earning ability and the burden of care.[2] Therefore, there are urgent needs to develop materials that effectively absorb low-intensity shockwaves.

Polyurea (PU) is the benchmark material that exhibits effective shockwave absorption properties. In spite of more than 5 years of study, the mechanism by which polyurea absorbs shockwave is still under debate.[3–5] Both experimental data and computational models (mesoscale, all-atom, and coarse-grained molecular level) have offered insights into polyurea's shockwave attenuation capability.[6–8] Roland *et al.* suggested that hydrogen bond-abundant, hard domains of PU have a small or negligible role in shockwave absorption.[9] Grujicic *et al.* confirmed that the impact-induced, rubbery-to-glassy transition acts as a potent ballistic-resistance-enhancing but not a shock-mitigating mechanism.[10] In addition, Grujicic *et al.* stated that the shock-induced hydrogen bond breaking in hard domains plays an important role in the shock-impact mitigation capacity of polyurea.[6] They also proposed shockwave induced ordering within the hard domains and viscoelastic relaxation within the hard/soft interfacial regions as another mechanism for reducing shock impact.[11] Even though an explicit shockwave absorption mechanism is absent, both groups along with other researchers reached the agreement that the micro-phase segregation in polyurea plays an important role for the high shockwave absorption performance.

Similar to the micro-phase segregation observed in polyurea, amphiphilic ionic liquids with alkyl tails also display structural heterogeneities on the nanometer spatial scale that may serve as an effective candidate for shockwave energy dissipation.[12–17] Evidence from both computer simulation and neutron/X-ray diffraction suggested that the alkyl chains in ionic liquids pack into a "soft, oily" matrix while the charged head groups tend to segregate into "hard" domains.[18,19] Recently, Yang et al. studied a class of network-forming ionic liquids (NIL), which are composed of alkyl-diammonium cations and citrate anions.[20] The long alkyl side chains of cations are used to frustrate the crystallization so that amorphous glassy solids form upon cooling. Peaks in the low Q ($Q \approx 0.4\text{-}0.7$ Å^{-1}) regime, corresponding to the nanometer spatial scale, provide the signature of structural heterogeneities in NILs.

4.3 Comparison of shockwave absorption performance between polyurea and network-forming ionic liquids

Laser induced stress waves are used to characterize the shockwave absorption property of NILs. Shockwaves are generated by impingement of a high-energy Nd:YAG pulsed laser on a 400 nm thick Al energy absorbing layer [21–26]. Transfer of energy from the laser pulse leads to rapid expansion of the Al layer. The presence of the confining layer on top of the Al film causes a high amplitude compressive shock wave to propagate through the specimen. The YAG laser power and beam diameter were varied to systematically control the input laser fluence. The out of plane displacement of the specimen surface was measured using a Michelson interferometer with a 532 nm laser diagnostic beam. A photodetector connected with 40GHz oscilloscope recorded the interference signal, which was converted to displacement and velocity history (as described previously by Wang et al).[21] The pressure profile, P(t), was obtained from velocity history using conservation of momentum,

$$P(t) = \rho_0 \left(U_s(t)\right) * U_p(t) = \rho_0 \left(s + cU_p(t)\right) * U_p(t) \tag{4.1}$$

where ρ_0 is initial material density, and $U_p(t)$ is particle velocity0 which is obtained from the measurement. Shock velocity, $U_s(t)$, is given by $s + cU_p(t)$ where s and c are fitted parameters from U_s - U_p Hugoniot of the aluminum substrate. The energy per area, i.e. total transmitted energy, was calculated from the velocity history using conservation of energy and momentum,

$$J(t) = \frac{1}{2} \rho_0 \int_0^t \left(U_p(t)\right)^2 * \left(s + cU_p(t)\right) dt \tag{4.2}$$
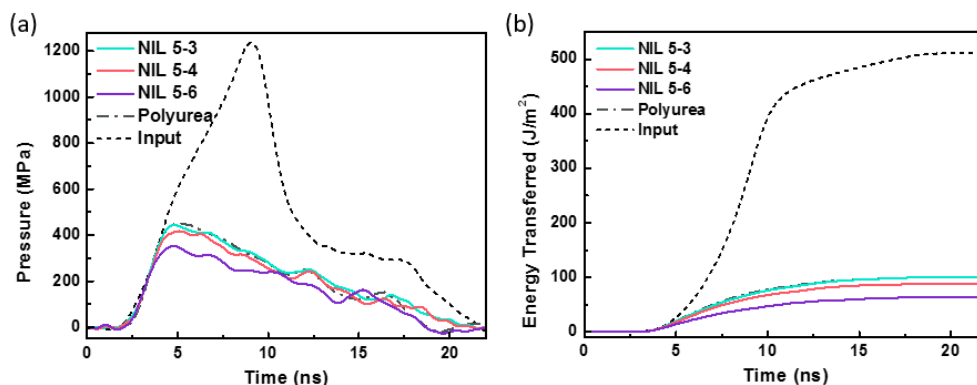
as previously described by Forbes.[27]

Figure 4.1 (a) Representative pressure profiles of NIL samples and polyurea obtained during laser induced shockwave test at 48mJ/mm² laser fluence; (b) representative total transferred energy profiles of NIL and benchmark polyurea specimens at 48mJ/mm² laser fluence. (Copyright © 2015 American Chemical Society)

Interferometric data under the shockwave impact were recorded for all NIL samples using polyurea as a reference .[21,26] The pressure profiles and total transferred shockwave energy were calculated from the measured surface velocity using equations (1) and (2) as described above. Input pressure profiles were obtained from input shockwave test specimen without test film. Direct shockwave impact resulted in a characteristic pressure profile displaying an abrupt rise on the nanosecond time scale. Representative pressure profiles for the different NILs are compared to the input and the benchmark polyurea pressure profiles at 48mJ/mm² laser fluence in Figure 4.1a. All of the materials tested caused a desirable reduction in peak pressure. In Figure 3a and 3b, the absorption of shockwave energy by NILs and polyurea also resulted in a shift of peak pressure time. The total transferred energy is plotted in Figure 4.1b. NIL 5-4 and NIL 5-6 dissipated 82.7% and 87.6% of the total input energy at 48mJ/mm² fluence, respectively. Both the reduction in peak pressure and reduction in total energy demonstrate that NILs are effective shockwave absorption materials. In addition, the NILs with longer side chains exhibited superior shockwave absorption performance. Average peak pressures of pristine NILs and polyurea obtained from multiple pressure profile data at each laser fluence were plotted in Figure 3c. The NILs with longer alkyl chains attenuated more shockwave peak pressure than NILs with shorter alkyl chains at all fluences.

To determine whether the NILs were capable of absorbing multiple rounds of shockwave impact, we measured the shockwave absorption of both pristine and post-shock NILs at various input laser fluences (Figures 4.2). Plotting the average peak pressures of all pristine NIL samples against input fluence revealed that the shockwave energy dissipation performance of NIL 5-6 is the best in the series, followed by NIL 5-4, NIL 5-3 and PU at all input fluences (Figure 4.2a). Furthermore, the differences between the values of peak pressure increased with input fluence since higher input laser fluences generated shockwaves at a faster strain rate. At the highest fluence (91 mJ/mm^2), the peak pressure of NIL 5-6 was 22% lower than that of NIL 5-3. For the post-shocked NIL samples, the peak pressures after absorption by NIL 5-3 and NIL 5-4 remained unchanged. In contrast, the peak pressure of shockwave absorbed by NIL 5-6 increased and became comparable to that of NIL 5-4. This loss of shockwave absorption ability indicated that pristine NIL 5-6
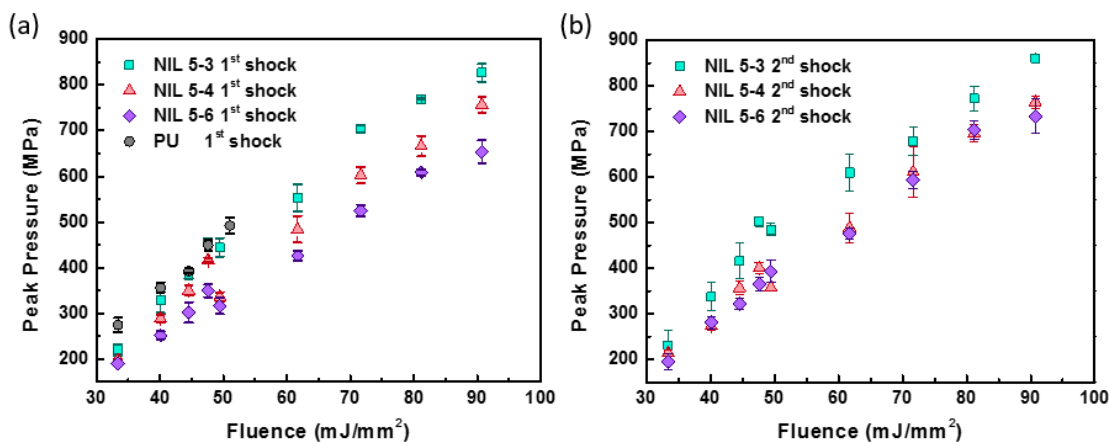

Figure 4.2 (a) average peak pressures at different laser fluences for pristine samples including PU; (b) average peak pressures at different laser fluences for post-shock NIL samples. (Copyright © 2015 American Chemical Society)

attenuated the impact via a slow relaxation or an irreversible alteration of material structure and properties.

4.4 Shock-induced ordering in the nano-segregated network-forming ionic liquid

Powder X-ray diffraction (XRD) enables microstructural analyses of pristine and post-shock NILs, thereby offering insights into NILs' shockwave attenuation mechanism (Figure 4.3). Powder XRD patterns of all NIL samples reflect their amorphous nature. There are three major diffraction features in the XRD plots. With a rough calculation based on the Q value at each peak's position, the correlation lengths for features resulting in peaks I, II and III are 11-13 Å, 7-8 Å and 3.8-4.4 Å. In particular, peak I has been observed in various ionic liquids systems, including alkyl-ammonium/phosphonium based salts, imidazolium salts, and other protic ionic liquids, and detailed neutron and X-ray scattering data show that it represents features associated with the structural heterogeneities on nanometer spatial scale.[19] A previous study also demonstrated that even short alkyl chains, such as ethyl or propyl groups, cause such heterogeneity.[18] The solvophobic interaction between alkyl chains and charged heads likely plays an important role in leading to this structural heterogeneity. Moreover, as alkyl side chain length increases, the nonpolar domains become interconnected and cause "swelling" of the entire ionic network, resulting in a "sponge-like" structure.[28]
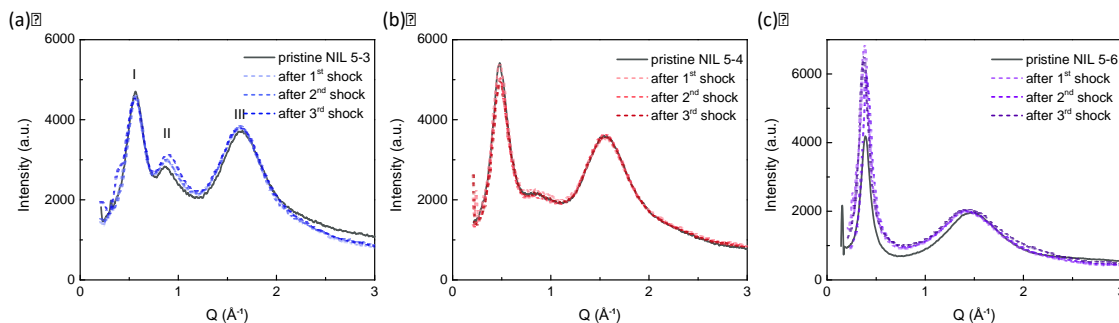

Figure 4.3 XRD pattern before and after shockwave impact for sample (a) NIL 5-3, (b) NIL 5-4 and (c) NIL 5-6. For NIL 5-3 and NIL 5-4, multiple shockwave impacts did not change microstructure significantly; while for NIL 5-6, the amplitude of low Q peak (peak I) increases significantly. (Copyright © 2015 American Chemical Society)

80

Comparing pristine samples of NIL 5-3 to NIL 5-6, it is evident that peak I in XRD shifts to lower Q values, indicating that the size of the heterogeneous domains increases. This result, along with the trend of shockwave dissipation, suggests that shockwave attenuation performance correlates positively with side chain length. After multiple shock impacts (up to three), the XRD patterns of NILs 5-3 and 5-4 remain the same, indicating little change in the microstructure. In contrast, there is peak sharpening with almost a two-fold increase of the amplitude of peak I for NIL 5-6 after the initial impact, suggesting that the segregation related with peak I become better defined. Specifically, the polar atoms (especially anion-anion correlations) across intervening non-polar domains become better correlated. The unchanged peak position indicates that the shockwave impact does not affect the size of the domains. We propose that shockwave causes the polar heads in NIL 5-6, which has the largest structural heterogeneity, to rearrange into a more correlated configuration. This rearrangement is responsible for the increase of NIL 5-6's peak pressure after first shock impact.
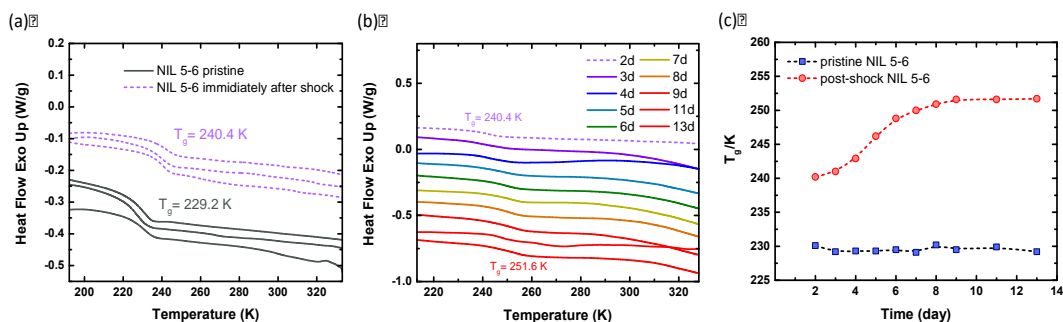
Figure 4.4 (a) Differential scanning calorimetry (DSC) measurements of three batches of NIL 5-6 pristine samples and post-shock samples. Glass transition temperature (T_g) value is marked; (b) DSC curve time evolution of post-shock NIL 5-6 samples. Over 7 days at room temperature, the T_g of post-shock samples increases by 11.2 K. From day 7 to day 11, T_g did not change; (c) plot of T_g as function of time for pristine NIL 5-6 sample and post-shock sample. The 0 day point is when samples were freshly prepared. The sample were freeze-dried for 2 days prior to DSC measurements and shock impacts. (Copyright © 2015 American Chemical Society)

To further validate the existence of hypothesized shock-induced ordering, we examined the differential scanning calorimetry (DSC) measurement of pristine NIL 5-6 and re-recorded the DSC data immediately after shocking on pristine samples (Figure 4.4). Pristine NIL 5-6 has a glass transition temperature (T_g) of 229.2K. After the first shock, the T_g of NIL 5-6 increases to 240.4 K. Nuclear magnetic resonance (NMR) and mass

spectrometry on post-shock sample ruled out the possibility of any shock-induced chemical changes. These results are consistent with our hypothesis of the shock-induced ordering in the heterogeneous domain. The 11.2 K increase of T_g may be due to the extra spatial hindrance from more ordered heterogeneous domain. To examine whether this rearrangement relaxes after shockwave impact, we kept the post-shock NIL 5-6 sample at room temperature and recorded the DSC curves time evolution of post-shock sample over a period of 11 days. The T_g of NIL 5-6 increased by another 11.2 K over 7 days and reached a stable value of 251.6K. This result indicates that the ordering process continues for days even after the shockwave impacts. The relaxing dynamics is rather slow due to high viscosity of NILs at room temperature. For comparison, the T_g of pristine NIL 5-6 is rather stable for months at room temperature.

The energy landscape theory of amorphous materials provides a viewpoint to qualitatively explain our observations. We hypothesize that the spatial correlation of polar heads and non-polar alkyl chains can potentially be rearranged by overcoming an energy barrier. Similar effects have been observed under high hydrostatic pressures. For example, high pressure can cause configurational changes in the alkyl groups of imidazolium ionic liquids.[29,30] Apparently, NIL with longer alkyl chains such as NIL 5-6 is easier to reorganize because of less restriction from the charged head group. The major structural change occurs at the first shock impact because the more correlated conformation are more stable. We also hypothesize that the molecular conformation does not reach local energy minimum immediately after the shockwave impacts, so the ordering processes slowly continues over time. To the best of our knowledge, this is the first time that shock-induced ordering in the liquid phase has been observed. With higher shockwave energy, further configurational changes of NIL along its energy landscape may occur, including possible formation of a crystal or ideal glass.

Combining these findings with the multiple shock experiments, the relationship of the microstructures of NILs and their shockwave absorption performances is evident. In NIL 5-3 and 5-4, the microstructure and shockwave absorption performance do not change through multiple shocks. In NIL 5-6, subsequent shockwave absorption performance is

reduced by irreversible shock-induced structural evolution and ordering in nano-segregated domains from the first shockwave impact. We conclude that the observed shock-induced ordering contributes to the better shockwave absorption performance in the initial shock of NIL 5-6. Thus, at least two mechanisms of shockwave absorption exist in the NIL system. Firstly, in the case of NIL 5-3 and NIL 5-4, the nano-segregated ionic network in NIL dissipate shockwave kinetic energy without causing noticeable structural change. In addition, in the case of NIL 5-6, irreversible change in spatial ordering within the ionic network also play a key role in extra shockwave energy absorbing capability.

4.5 Experimental section

4.5.1. Materials and methods

All chemicals were purchased from Aldrich as highest purity grade and used without further purification. All reactions were performed under nitrogen/argon atmosphere. NMR spectra were recorded on Varian Unity 400 NB, Varian VXR 500 and Varian Unity 500 NB spectrometer. High resolution electrospray mass spectra were obtained on a Micromass Q-Tof Ultima.

X-ray powder diffraction of NIL

X-ray diffraction experiment was conducted using Rigaku Miniflex 600 X-ray diffractometer with Cu Kα radiation. A thin layer of sample was pasted on a glass sample holder, which was then tested in the measurement chamber.

Differential scanning calorimetry (DSC) measurement of NIL

The DSC measurement was performed using TA Instrument Q20 Differential Scanning Calorimeter equipped with a Liquid Nitrogen Cooling System (LNCS). Tzero aluminum pan and lids were used as sample testing containers. Nitrogen was used as sample purge gas.

Typical DSC measurement procedure includes 3 cyclic scans. One cyclic scan includes one heating and cooling process. To minimize the aging effect of NIL at higher

temperature, temperature range for each scan is -100~60 ℃ with heating/cooling rate 10 ℃/min. The glass transition temperatures were determined at the inflection point of the step from the second heating scan. For post-shock samples, we used sample that is untested by DSC to avoid any aging effect from the heating process in DSC runs.

4.5.2 Preparation of NIL shockwave impact test specimen

NIL test specimens, shown schematically in Figure 4.5, were prepared by drop casting 20mg of NIL on a glass substrate (2.5mm x 2.5mm square, 1 mm thick) with a 50μm thick polyimide spacer to control the thickness of the NIL layer. A second glass substrate was then placed on top of the specimen with a pressure of 55 kPa. A NIL layer with 50μm thickness was confirmed by scanning electron microscope. Polyurea test specimens were prepared in a similar fashion by drop casting a mixture of 80 wt% of an oligomeric amine (Versalink P-1000, Air Product and Chemicals) and 20 wt% of a multi-functional isocyanate precursor (Isonate 143L, Dow Chemical) onto a glass substrate with a 50μm thick polyimide spacer. A second glass substrate was then placed on top of the specimen and the mixture was cured 24 hours at room temperature and another 24 hours at 60 ℃. Both the NIL and polyuria sandwich specimens were prepared for laser-induced shockwave testing by electron beam deposition of a 400 nm thick Al layer (400 nm) on the outer surface of one glass substrate , followed by spin coat deposition of a 6 μm thick sodium silicate layer on the top of the Al layer. Another Al layer (200 nm) was deposited on the surface of the glass substrate on the opposite side of the specimen via electron beam deposition.
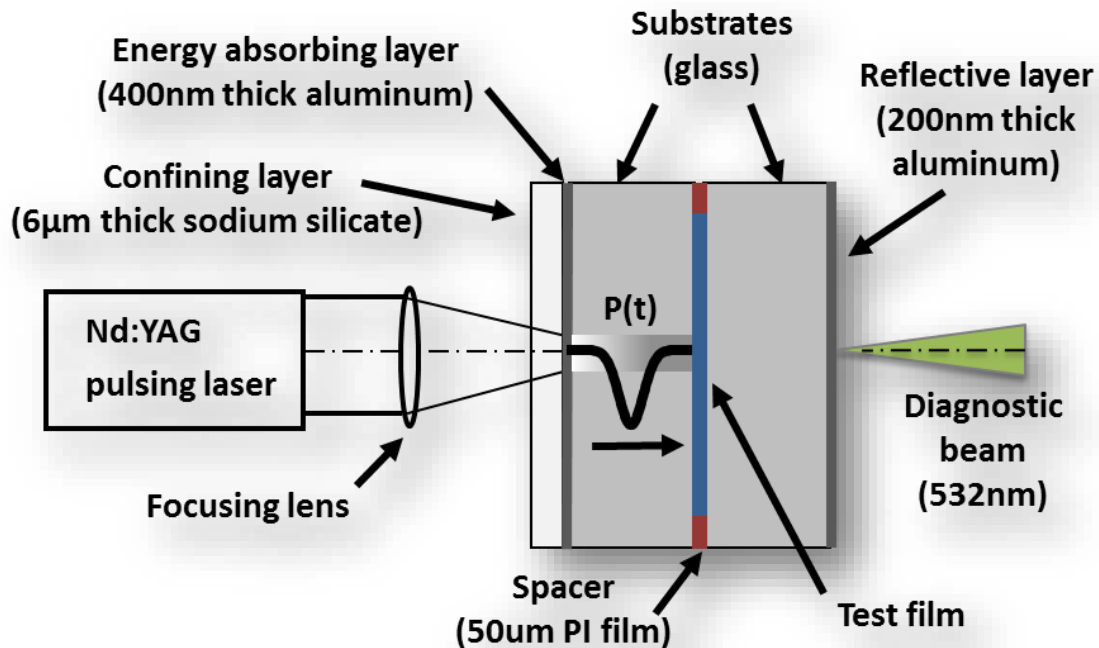
Figure 4.5 Schematic depiction of direct laser drive experimental set-up and specimen structure. (Copyright © 2015 American Chemical Society)

4.5.3 Laser-induced Shockwave Test Protocol

A schematic of the modified laser spallation set up is shown in Figure 4.5. Shockwaves are generated by impingement of a high-energy Nd:YAG pulsed laser (New Wave Tempest) on the 400 nm thick Al energy absorbing layer. Transfer of energy from the laser pulse leads to rapid expansion of the Al layer. The presence of the confining layer on top of the Al film causes a high amplitude compressive shock wave to propagate through the specimen. The YAG laser power and beam diameter were varied to systematically control the input laser fluence.

The out of plane displacement of the specimen surface was measured using a Michelson interferometer with a 532 nm laser diagnostic beam. A photodetector connected with 40GHz oscilloscope (LeCroy LC584 A) recorded the interference signal , which was converted to displacement and velocity history (as described previously by Wang and Gupta et al. [21,31] The pressure profile, P(t), was obtained from velocity history using conservation of momentum,

$$P(t) = \rho_0 \left(U_s(t) \right) * U_p(t) = \rho_0 \left(s + c U_p(t) \right) * U_p(t) \qquad (4.3)$$

where ρ_0 is initial material density, and $U_p(t)$ is particle velocity which is obtained from the measurement. Shock velocity, $U_s(t)$, is given by $s + c U_p(t)$ where s and c are fitted parameters from U_s - U_p Hugoniot of the aluminum substrate.
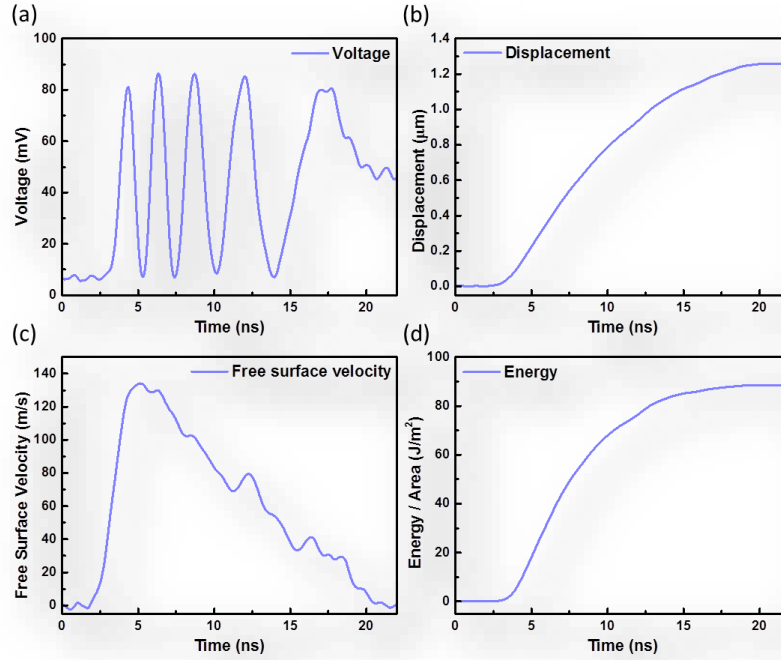

Figure 4.6 Representative interferometric data obtained from laser-induced shock wave test of a NIL5-4 sample : (a) photodetector fringe data captured by the oscilloscope, (b) displacement as a function of time from photodetector fringe data as described previously by Wang and Gupta et al. [21,31] *, (c) free surface velocity calculated from displacement, (d) energy/area calculated from Eq. (2). (Copyright © 2015 American Chemical Society)*

The energy per area, i.e. total transmitted energy, was calculated from the velocity history using conservation of energy and momentum,

$$J(t) = \frac{1}{2} \rho_0 \int_0^t \left(U_p(t) \right)^2 * \left(s + c U_p(t) \right) dt \qquad (4.4)$$

as previously described by Forbes.[27]

NIL sandwich specimens were also subjected to multiple shockwave impacts. For these experiments, the entire area of the energy absorbing layer of a NIL specimen was impacted multiple times with ND:YAG pulsed laser (2 mm spot sizes and laser fluence of

91 mJ/mm^2). Each 2mm impact spot was created with a 2.5mm center to center distance from adjacent impact spots across the entire specimen. After the energy absorbing aluminum layer was fully consumed, the shocked NIL layer was transferred to a new set of glass substrates with a pristine Al energy absorbing layer for a subsequent round of shock testing.

4.6 References

(1)   Nakagawa, A.; Manley, G. T.; Gean, A. D.; Ohtani, K.; Armonda, R.; Tsukamoto, A.; Yamamoto, H.; Takayama, K.; Tominaga, T. *J. Neurotrauma* **2011**, *28*, 1101–1119.

(2)   Courtney, A. C.; Courtney, M. W. *Med. Hypotheses* **2009**, *72*, 76–83.

(3)   Bahei-El-Din, Y. A.; Dvorak, G. J.; Fredricksen, O. J. *Int. J. Solids Struct.* **2006**, *43*, 7644–7658.

(4)   Grujicic, A.; LaBerge, M.; Grujicic, M.; Pandurangan, B.; Runt, J.; Tarter, J.; Dillon, G. *J. Mater. Eng. Perform.* **2011**, *21*, 1562–1579.

(5)   Gardner, N.; Wang, E.; Kumar, P.; Shukla, A. *Exp. Mech.* **2011**, *52*, 119–133.

(6)   Grujicic, M.; Pandurangan, B.; Bell, W. C.; Cheeseman, B. A.; Yen, C.-F.; Randow, C. L. *Mater. Sci. Eng. A* **2011**, *528*, 3799–3808.

(7)   Grujicic, M.; Pandurangan, B. *J. Mater. Sci.* **2012**, *47*, 3876–3889.

(8)   Arman, B.; Reddy, A. S.; Arya, G. *Macromolecules* **2012**, *45*, 3247–3255.

(9)   Bogoslovov, R. B.; Roland, C. M.; Gamache, R. M. *Appl. Phys. Lett.* **2007**, *90*, 221910.

(10)   Grujicic, M.; Pandurangan, B.; He, T.; Cheeseman, B. A.; Yen, C.-F.; Randow, C. L. *Mater. Sci. Eng. A* **2010**, *527*, 7741–7751.

(11)   Grujicic, M.; Snipes, J. S.; Ramaswami, S.; Yavari, R.; Runt, J.; Tarter, J.; Dillon, G. *J. Mater. Eng. Perform.* **2013**, *22*, 1964–1981.

(12)   Zhao, Y.; Hu, Z. *Chem. Commun.* **2012**, *48*, 2231–2233.

(13)   Song, X.; Hamano, H.; Minofar, B.; Kanzaki, R.; Fujii, K.; Kameda, Y.; Kohara, S.; Watanabe, M.; Ishiguro, S.; Umebayashi, Y. *J. Phys. Chem. B* **2012**, *116*, 2801–2813.

(14)   Ji, Y.; Shi, R.; Wang, Y.; Saielli, G. *J. Phys. Chem. B* **2013**, *117*, 1104–1109.

(15)   Canongia Lopes, J. N. A.; Pádua, A. A. H. *J. Phys. Chem. B* **2006**, *110*, 3330–3335.

(16)   Hettige, J. J.; Araque, J. C.; Margulis, C. J. *J. Phys. Chem. B* **2014**, *118*, 12706–12716.

(17)   Li, S.; Bañuelos, J. L.; Zhang, P.; Feng, G.; Dai, S.; Rother, G.; Cummings, P. T. *Soft Matter* **2014**, *10*, 9193–9200.

(18)   Atkin, R.; Warr, G. G. *J. Phys. Chem. B* **2008**, *112*, 4164–4166.

(19)   Zheng, W.; Mohammed, A.; Hines, L. G.; Xiao, D.; Martinez, O. J.; Bartsch, R. A.; Simon, S. L.; Russina, O.; Triolo, A.; Quitevis, E. L. *J. Phys. Chem. B* **2011**, *115*, 6572–6584.

(20)   Yang, K.; Tyagi, M.; Moore, J. S.; Zhang, Y. *J. Am. Chem. Soc.* **2014**, *136*, 1268–1271.

(21)   Wang, J.; Weaver, R. L.; Sottos, N. R. *Exp. Mech.* **2002**, *42*, 74–83.

(22)   Grady, M. E.; Geubelle, P. H.; Braun, P. V; Sottos, N. R. *Langmuir* **2014**, *30*, 11096–11102.

(23)   Grady, M. E.; Beiermann, B. A.; Moore, J. S.; Sottos, N. R. *ACS Appl. Mater. Interfaces* **2014**, *6*, 5350–5355.

(24)   Youssef, G.; Gupta, V. *Exp. Mech.* **2012**, *53*, 145–154.

(25)   Youssef, G.; Gupta, V. *Mech. Time-Dependent Mater.* **2011**, *16*, 317–328.

(26)   Gupta, V.; Argon, A. S.; Parks, D. M.; Cornie, J. A. *J. Mech. Phys. Solids* **1992**, *40*, 141–180.

(27) Forbes, J. W. In *Shock Wave Compression of Condensed Matter*; Springer, 2012; pp. 13–29.

(28) Hayes, R.; Imberti, S.; Warr, G. G.; Atkin, R. *Phys. Chem. Chem. Phys.* **2011**, *13*, 13544–13551.

(29) Zhao, Y.; Liu, X.; Lu, X.; Zhang, S.; Wang, J.; Wang, H.; Gurau, G.; Rogers, R. D.; Su, L.; Li, H. *J. Phys. Chem. B* **2012**, *116*, 10876–10884.

(30) Gardas, R. L.; Freire, M. G.; Caryalho, P. J.; Marrucho, I. M.; Fonseca, I. M. A.; Ferreira, A. G. M.; Coutinho, J. A. P. *J. Chem. Eng. Data* **2007**, *52*, 80–88.

(31) Gupta, V.; Argon, A. S.; Parks, D. M.; Cornie, J. A. *J. Mech. Phys. Solids* **1992**, *40*, 141–180.

CHAPTER 5

FACILE DESIGN AND SYNTHESIS OF THERMOPLASTIC IONIC ELASTOMER WITH FAST AUTOMATIC SELF-HEALING

5.1 Abstract

An intrinsic self-healing material that can repair itself without consuming healing agents or external energy would improve the material lifetime span, maintaining and energy cost, and environmental impact significantly. The combination of high modulus and intrinsic self-healing ability remains a key challenge in this area. The only few available examples of stiff intrinsic self-healing polymers involves expensive raw materials and intensive synthesis efforts, which partly compromise the motivation for intrinsic self-healing material. Here we design an ionically crosslinked network that is low cost, facile to synthesize and show stiff plateau modulus while still maintaining self-healing capability. By ionically associating a commercially available low T_g oligomer with multivalent organic cations, the resulting ionic network exhibit competitive plateau modulus. Thanks to the dynamic nature of ionic interaction, this ionic network is capable of releasing excessive stress and super-fast self-healing at room temperature. The low cost, facile synthesis, stiff modulus, and excellent stress-releasing and self-healing abilities make the ionic elastomer a unique system for future applications.

5.2 Introduction

The reprocessing and recycling of conventional rubber has been greatly limited by permanent covalent crosslinks. In terms of reprocessibility or self-healing ability, supramolecular rubbers provide approachable solutions based on the reversible nature of the bonds.[1–6] Specifically, H-bond based system has becomes very successful because of the feasibility of incorporating multiple H-bond donor/acceptors in monomers and excellent reversibility based on low bond energy of H-bonds. However, the low bond energy of H-bond also limit the mechanical properties of supramolecular polymers. As a

consequence, supramolecular elastomers usually have lower Young's modulus compared to covalent rubber. [2,3,7–9] To some extent, the lack of competitive mechanical properties compromises the potential application of self-healing supramolecular rubbers.

The selection of non-covalent interaction is a challenge for the goal of forming a stiffer supramolecular network while maintaining complete reversibility.[10–12] Compared with H-bonds, ionic interactions have a much wider range of bond energy. In addition, the bond energy of ionic interaction depends on the ion pairs and also the distance between cations and anions thus can be further fined-tuned with selections.[13] We propose to use ionic interaction as the crosslinking bond type to form a supramolecular network. We rely on small ions and short oligomer blocks rather than long polymers for higher density of crosslinks (lower molecular weight between crosslinks M_c), which is supposed to yield a better elastic modulus in the case of an ideal crosslinked highly elastic network. By crosslinking oligomeric anion with different types of cations, we have obtained a stiff supramolecular elastomer that we named ionic rubber (IR).

5.3 Synthesis of imidazolium and guanidinium-based ionic rubber

To synthesize an effective ionic network that exhibit rubbery mechanical properties without forming nano- or micro-crystallization requires appropriate ionic crosslink density.
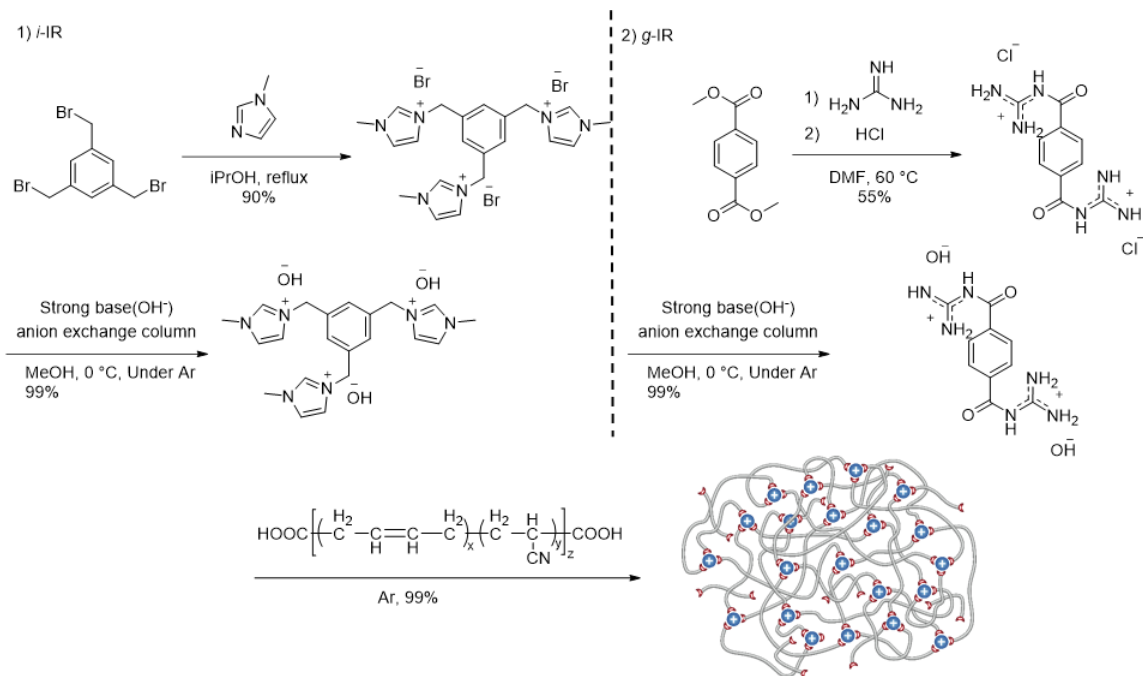

Figure 5.1 Synthetic route of tri-imidazolium cations and di-guanidinium cations and subsequent synthesis of ionic rubber

Inspired by the example of epoxy, we propose the use of a short polymer chain (oligomeric chain) and a small multivalent crosslinker. The use of relatively short polymer chain can ensure high ionic crosslink density as compared to the case of end-chelating long polymer chain where ionic crosslink plays a much weaker role than inter-chain VDW force. For this purpose, we have chosen a commercially available carboxylic terminated polybutadiene and polyacrylnitrile (CTBN) as the oligomeric anion. CTBN is a series of commercially available oligomers that are commonly used as tougher in epoxy industry. They are referred as "liquid rubber" because their glass transition temperatures are in the range from -70 ℃ to -50 ℃ and they appear as viscous liquids at room temperature. The terminating carboxylic acid groups can be easily incorporated into ion pairs with common cations. Since we will crosslink CTBN from both ends, the molecular weight of CTBN oligomer chain naturally becomes average molecular weight between crosslinks for the resulting networks. Typical CTBN comes at molecular weight from 3000 to 4000, which is below

or near its critical entanglement molecular weight but ideal in our case for the formation a stiff elastic network.

As the other part of ionic rubber, cations play the role of multivalent crosslinker. Naturally, the strength of ionic interaction is one critical parameter that determines the performance of the proposed ionic network. We proposed two kinds of small molecular crosslinker with discrete ionic bond energy. One is multivalent imidazolium cation and the other is multivalent guanidinium cation. Imidazolium-carboxylate is well-studied ionic interaction type in the area of ionic liquids that has weak to medium ionic interaction strength (bond energy ~ 30 kcal/mol).[14] Whereas guanidinium-carboxylic interaction is quite common in bio-macromolecules, specifically in protein-DNA interaction. It is a very strong hydrogen-bonding assisted ionic interaction (bond energy ~ 120kcal/mol).[15,16] A simple one-step synthetic pathway introduces desired imidazolium and guanidinium functional groups to a multivalent core. The halogen counter-anion was then replaced with hydroxide using a strong base type anion exchange column. *In situ* reaction with CTBN yields the mixture of desired ionic product and water. The materials were vacuum dried at elevated temperature for two days to drive off the remaining solvent and water. We name this new material ionic rubber, specifically, the imidazolium based ionic rubber (*i*-**IR**) and the guanidinium based ionic rubber (*g*-**IR**).

5.4 Thermal analysis

Thermogravimetric analysis (TGA) has shown well-defined weight loss process for cations and CTBN anions respectively. Specifically, the decomposition of both trimidaozlium cations and bisguanidinium cations has an onset temperature around 250 ℃. The onset temperature of main weight loss of crude CTBN and ionic rubber is around 350 ℃. Since we are coupling small molecule cation and oligomeric anion stoichiometrically, and molecular weight of oligomeric anion is considerably larger than small molecular cation, the actual content of cation crosslinker is less than 5% by weight. Considering the CTBN is a commercially available industry product, the cost of ionic rubber is favored in terms of the availability of raw materials.
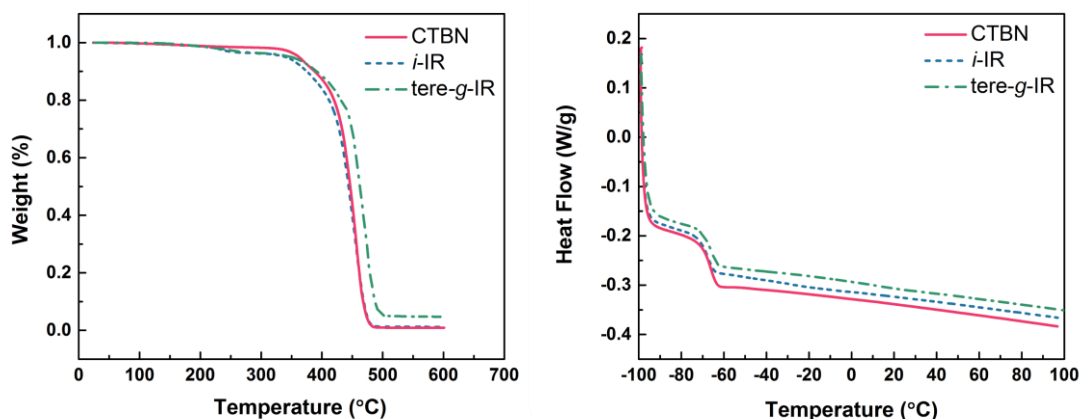

Figure 5.2 TGA and DSC trace of crube CTBN polymer and ionic rubber (i-IR and tere-g-IR). The TGA of iso-g-IR and tere-g-IR overlaps.

Differential scanning calorimetry (DSC) has been measured for both imidazolium and guanidinium ionic rubbers and as-received CTBN polymer. For the given type of CTBN, the measured T_gs are all around -64 °C. It's very clear that the imidazolium and guanidinium cations do not change the overall T_g of the ionic rubber. Unlike its counterpart in epoxy or other covalent crosslinking network, where crosslinks restricts chain mobility thus increases T_g, the ionic crosslinking at the end of oligomer does not change the T_g. This is because the amount of end groups is small compared with backbone repeating units. In this case, the influence of the ionically crosslinked end on the T_g is negligible.

5.5 Mechanical performance

The dynamic temperature sweep measurement of CTBN and ionic rubber show the dynamic storage modulus (G'), loss modulus (G") and tan δ plotted as a function of temperature at constant frequency 1Hz, Figure 5.3. The rheological properties of CTBN clearly showed its liquid nature at room temperature with G''>G'. Because of the low molecular weight, no noticeable rubbery plateau is present either. (Figure 5.3a) With addition of only 5% by weight of imidazolium cation, the rheological properties changes dramatically. (Figure 5.3b) For the *i*-**IR**, at very low temperatures (below T_g), the materials' rheological response is highly elastic with G'>G". At higher temperature, the rheological
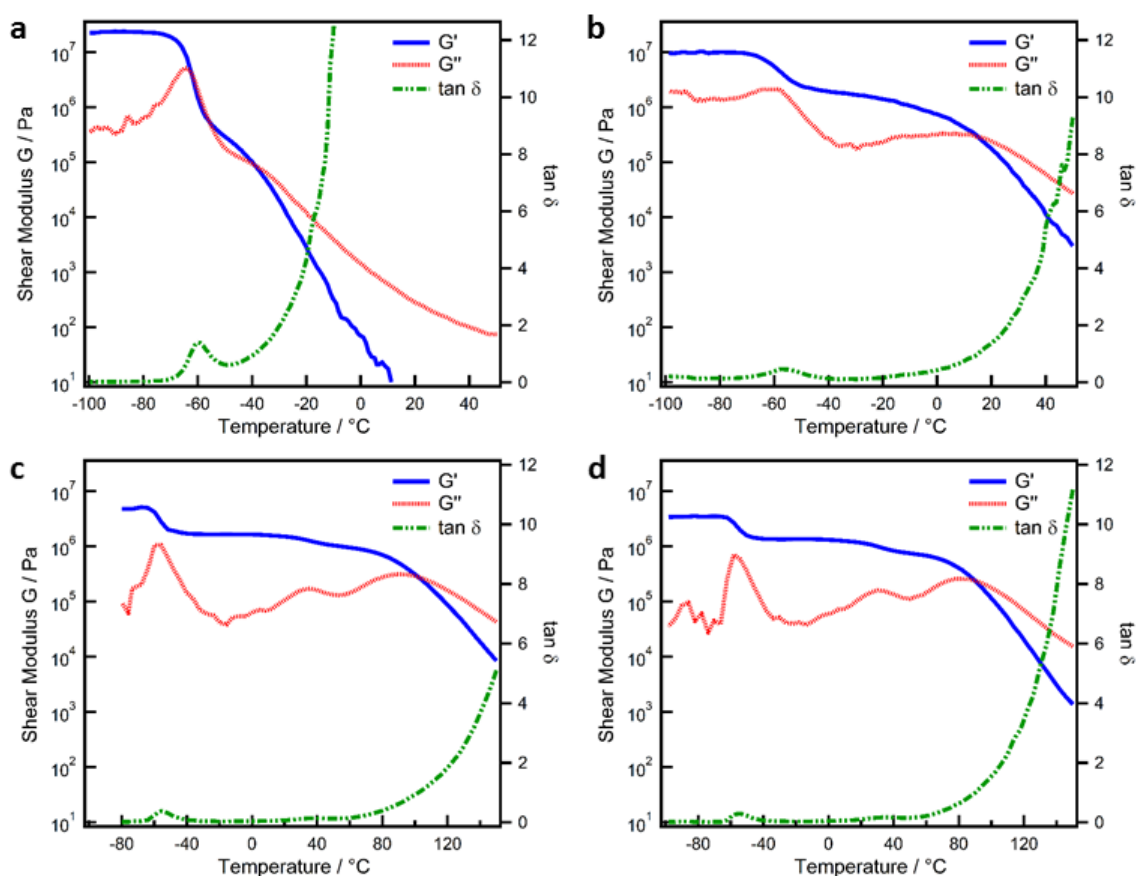

*Figure 5.3 Rheological temperature sweep measurements at 1Hz. **a**, as received CTBN "liquid rubber"; **b**, tri-imidazolium crosslinked ionic rubber; **c**, tere-bisguanidinium crosslinked ionic rubber; and **d**, iso-bisguanidinium crosslinked ionic rubber.*

response is predominantly viscous with G'<G". The existence of this regime means that

this crosslinked network is completely malleable either thermally or with the aid of solvent. The material undergoes a transition from rubbery behavior to viscous liquid-like behavior. The crossover temperature (T_c) of G' and G" is the solid-to-liquid transition temperature measured mechanically at the given frequency. For *i*-**IR**, the crossover temperature is 15 ℃, which is around room temperature. Between T_g and T_c, a well-defined rubbery plateau is observed in *i*-**IR**, having a storage shear modulus above 1 MPa. The high rubbery plateau modulus is well above common supramolecular elastomers that are based on H-bonding, ionic interaction and some reversible covalent bonds. It is even competitive with conventional permanent covalent rubber. For practical application around room temperature, the below-room temperature T_c for *i*-**IR** is still not satisfying. This is mainly due to the relatively weaker ionic linkage between imidazolium and carboxylate. In addition, peak of tan δ also indicates T_g. In all samples, the T_g from rheometer overlaps with DSC measurements.

We propose to use a stronger ionic interaction to increase the T_c of the resulting ionic network. Since we are not changing the molecular weight of CTBN, which is the average molecular weight between crosslinks of the rubber network, the resulting ionic rubber will have similar elastic modulus at the rubbery plateau. Rather, we are elevating the temperature at which the ionic network will collapse and goes into liquid state. The interaction between guanidinium and carboxylate is one of the strongest ionic interaction that involve carboxylate. As shown in Figure 5.3c&d, by incorporating the much stronger ionic interaction, the T_c is 102 ℃ for tere-*g*-**IR** and 90 ℃ for iso-*g*-**IR**. Just like our prediction, the modulus of g-IR is in the same range as i-IR, which is more or less determined by molecular weight of CTBN we used. The g-IR combines competitive elastic modulus at rubbery plateau and the complete reprocessibility if heated above its T_c.

5.6 Rate-dependent stress release

The ionic rubber network is capable of releasing internal stress at different strain rate. Figure 5.4 shows stress-strain curves that exhibit a highly rate-dependent behavior. Take **tere-*g*-IR** for example, when pulling fast at 0.3 s^{-1}, the ionic rubber resemble the

mechanical response of elastomer with more than 50% of strain at breaking point. While when pulling slowly at 0.075 s^{-1}, the ionic rubber first exhibits an elastic response and then the relaxation process starts to take over, resulting in a decrease of the internal stress despite increasing strain. Similar behavior is observed in **iso-*g*-IR** as well with lower modulus. Also, the strain rate for the onset of stress-relaxation process is material-specific. The **tere-*g*-IR** still exhibit some degree of stress relaxation before breaking even when pulled at a very fast rate 0.3 s^{-1}, the **iso-*g*-IR** show similar behavior at the rate of 0.075 s^{-1}. The rate-dependent stress-relaxation is not uncommon in polymers, but such sensitivity towards strain rate is hard to achieve from conventional covalent crosslinked rubber. This unique stress-releasing behavior is solely based on the dynamic nature of ionic crosslinks in the network. During the stretching of the material, the material is releasing the internal stress through the breakage of ionic crosslinks. If the strain rate is faster than the dynamics of stress-releasing, the material is going to fail at a lower strain point. If the strain rate is
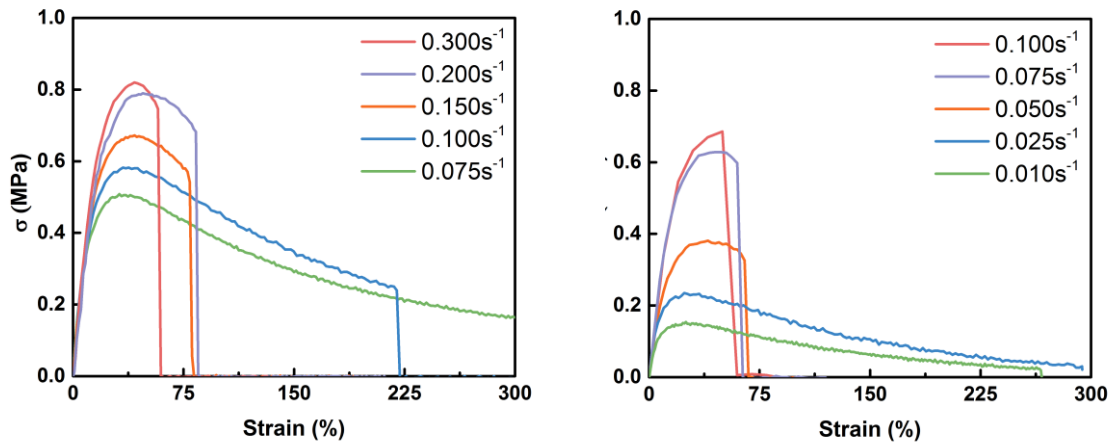

Figure 5.4 Stress-strain curve of tere-g-IR and iso-g-IR at different constant strain rate: at high strain rate, the ionic rubber is stiff; at low strain rate, the dynamic ionic interaction can release internal stress, leading to significant stress relaxation.

slower than the releasing of the stress, finally the internal stress in the material is going to be released thorough breaking the dynamic bonds and tends to go to zero before failure. To test the residual strain after moderate deformation, we have measured the remaining strain of **tere-*g*-IR** after a 50% and 100% strain loading followed by an immediate

5.7 Super-fast self-healing at room temperature

In contrast to covalent rubber, ionic rubber can self-heal at room temperature simply after the broken parts are put into contact. Compared with other supramolecular elastomer, the self-healing of ionic rubber does not require solvent, strong pressure and will complete within seconds or a few minutes. After being cut into pieces, the samples are
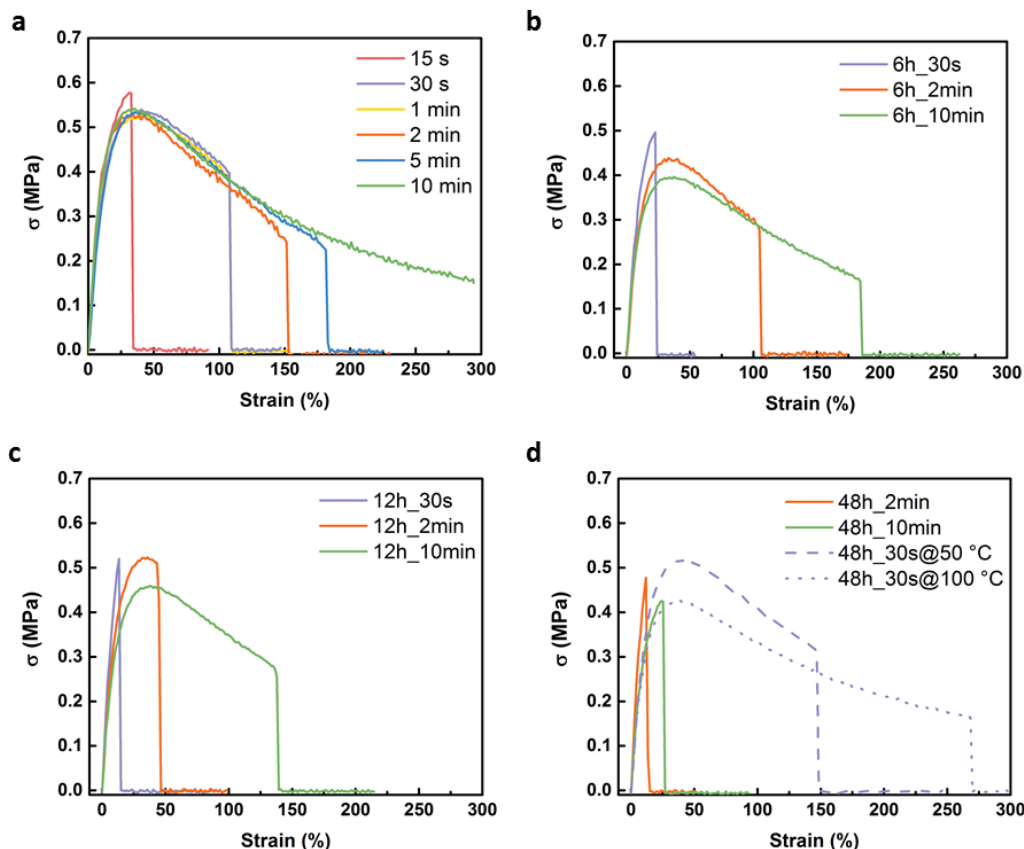

Figure 5.5 Fast self-healing at room temperature of iso-g-IR. Cut parts are brought into contact at room temperature (20 °C) immediately after being cut (within 5 minutes). Stress-strain curve of self-healed tere-g-IR at different healing time. The strain rate for all tests is 0.075 s⁻¹.

brought into contact at room temperature. The healed samples are able to recover the original shape, size and modulus. Figure 5.5a demonstrates the mechanical response of **tere-*g*-IR** after certain healing time after being put into contact immediately (within 5 minutes) after being cut. The material is able to sustain larger deformations and thus release stress further. Impressively, even after 15s, the ionic rubber can self-healing and fully

98

recover the modulus. The stress-strain curves superpose and show a larger deformation at break. After 10min, the sample is fully healed and sustain same damage as pristine sample.

The self-healing nature of the ionic rubber is also based on the dynamic nature of ionic interaction. The superfast self-healing of this material depends on two factors. First, the dynamic nature of ionic interaction plays the most important role. When two parts are put into contact, the smaller cation can diffuse throughout the interface and form new crosslinks with oligomeric anions. Second, the oligomeric anion itself has relatively fast dynamics at room temperature as well. As indicated by DSC result, the glass transition temperature of the ionic rubber is -64 ℃. At room temperature, the oligomeric anion is able to contribute to the self-healing result as well. As a consequence of both effects, the ionic rubber can achieve superfast self-healing even at room temperature.

Unlike other supramolecular self-healing materials, the healing of the ionic rubber does not depend on the free groups for self-healing mechanism. Rather, it is determined by the distance between the cut pieces and the diffusive motion of the ions. The ionic rubber does not suffer from the loss of free groups during waiting time when the cut pieces are separated. Theoretically, if the cut surface can sustain its original shape, ionic rubber should sustain its self-healing capability for however long the cut pieces are separated, because the dynamics of the ions is determined by temperature only. However, practically, after certain time, the self-healing efficiency is slowing down. Figure 5.5b&c show the material can still heal efficiently in a few minutes after a waiting time of 6h and 12h. However, after 48h of waiting time, the healing efficiency decreases significantly compared with the case in 6h and 12h. Still, after only 2 min of healing, the sample is able to sustain almost 25% strain before breaking point. The reason why the healing performance deteriorated over longer time is because the slight change of shape of the cut surface. We did observe the edge of the cut surfaces becomes more rounded after 48h of waiting time because of gravity and the fast dynamic nature of this material. This slight change of shape results in mismatch of cut surfaces and thus much bigger gap for ionic rubber to fill to achieve the self-healing. To confirm this mechanism, we did same healing experiment for 48h samples at 50 ℃ and 100 ℃. Not surprisingly, with much faster

dynamics at elevated temperature, the sample restore almost its complete mechanical strength within 30s for both cases.

5.8 Experimental section

5.8.1 Materials and methods

All chemicals were purchased from Aldrich as highest purity grade and used without further purification. All reactions were performed under nitrogen/argon atmosphere. NMR spectra were recorded on Varian Unity 400 NB, Varian VXR 500 and Varian Unity 500 NB spectrometer. High resolution electrospray mass spectra were obtained on a Micromass Q-Tof Ultima. Elemental analysis was obtained from Exeter Analytical CE 440 CHN Analyzer and PerkinElmer 2400 Series II CHN/O Elemental Analyzer and Thermo Scientific Orin Ion Selective Electrodes.

Carboxyl-Functional Polymers are carboxyl-terminated butadiene and butadiene-acrylonitrile copolymers (CTBN) was given generously by Emerald Performance Materials. We have requested three kinds of CTBN: Hypro 1300X13 CTBN, Hypro 1300X31 CTBN and Hypro 1300X8 CTBN. Their properties were listed in Table 5.1.

Table 5.1 Properties of CTBN polymers from Emerald Performance Materials

Product	% Acrylnitrile	Glass Transition, ℃	Acid Number	Molecular Weight	Functionality
Hypro™ 1300X13	26% acrylonitrile.	-39 ℃	32	3150	1.9
Hypro™ 1300X31	10% acrylonitrile,	-66 ℃	28	3800	1.9
Hypro™ 1300X8	18% acrylonitrile,	-52 ℃	29	3550	1.9

Rheometer Measurement. The rheological measurement was performed using TA Instruments AR-G2 Rheometer. The geometry used was 8mm aluminum plates and the testing method was temperature sweep in oscillation mode. The frequency of dynamic loading was 1Hz and the strain was 0.3%. During the testing procedure, the gap was controlled between 900-1200μm with active axial force adjustment. Temperature control was made using active cooling system and environmental test chamber.

Dried sample was transferred to aluminum plate on rheometer under nitrogen purge. Upon heating, the sample will turn into viscous liquid, which was easier to load correctly without any over/under filling or introducing any gas bubbles. After sample loading, a temperature sweep test (typical temperature range is -30~50 °C) was carried out. G' and G'' was obtained as a function of temperature. We used the cross point of G' and G'' to determine the crossover temperature.

5.8.2 Synthesis of triimidazolium and diguanidinium ionic rubber
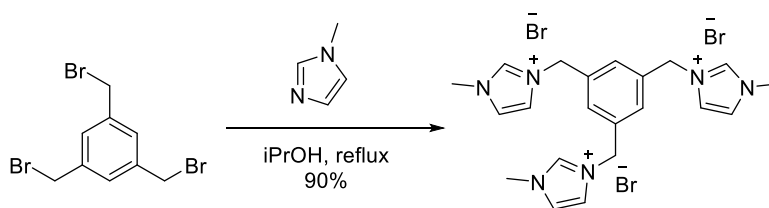
Tris(bromomethyl) benzene (20mmol) and 1-methylimidaozle (60mmol) was loaded into a schlenk flask protected with nitrogen, followed by adding 100mL isopropanol as solvent. The reactions were carried out under nitrogen atmosphere and at reflux temperature for 48 hours. The product was purified by recrystallization at 80 ℃ with ethanol and ethyl acetate.

3,3',3''-(benzene-1,3,5-triyltris(methylene))tris(1-methyl-1H-imidazol-3-ium) bromide

A off-white crystal was obtained after recrystallization. ^{1}H NMR (DMSO): δ 3.89 (s, 9 CH$_3$); δ 5.47 (s, 6, CH$_2$); δ 7.54 (s, 3, CH); δ 7.76 (s, 3, CH); δ 7.83 (s, 3, CH); δ 9.40 (s,

3, CH). ^{13}C NMR (D_2O): δ 36.68 (CH_3); δ 51.85 (CH_2); δ 123.06 (CH); δ 124.66 (CH); δ 129.28 (CH); δ 136.96 (CH); δ 137.54 (CH).
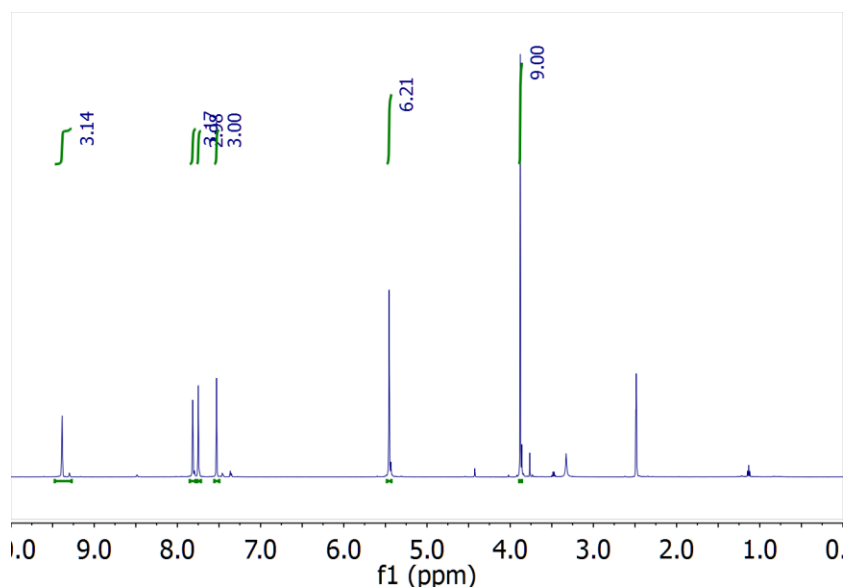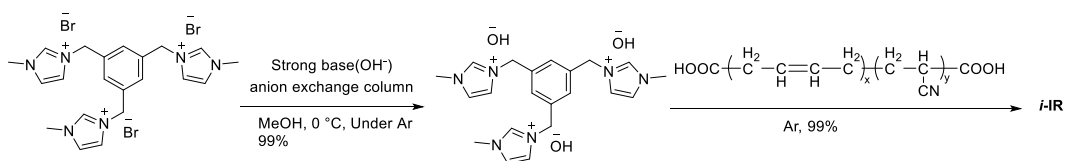

Figure 5.6 ^1H NMR spectrum of triimidazolium bromide salts.

The triimidazolium bromide salt was dissolved in methanol. The solution was added into an anion exchange column (Dowex® Monosphere® 550A UPW type 1 strong base anion exchange resin, preliminary elution and wash was carried out using methanol). In order to maximize the conversion of bromide anion into hydroxide anion, the column was run carefully and the eluent was protected under argon atmosphere. The eluent was reacted directly (*in situ*) with X31-CTBN in chloroform in ice bath. After the anion exchange column, the solution was evaporated. The sample was freeze-dried or dried under high vacuum at 80 °C for 48h. The materials were obtained at room temperature.
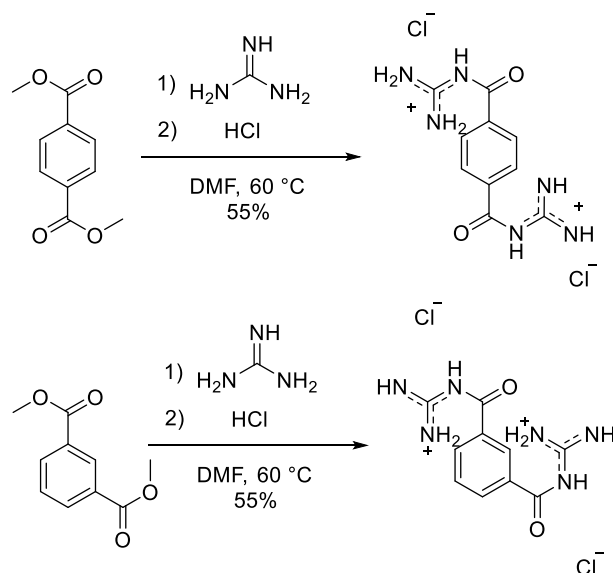
Synthesis of Iso/tere-guanidinium chloride salts

Guanidinium Hydrochloride (75mmol eq) was loaded into a schlenk flask, protected with nitrogen gas and dissolved in 75mL of Dimethylformamide (DMF). While protected under nitrogen gas, Sodium Hydroxide (100mmol eq) was slowly added at 0˚C. After five minutes following complete addition of NaH, the temperature was raised to room temperature (~21˚C). The reaction was carried out in Nitrogen atmosphere for 90 minutes. Following the duration of the synthesis of the Guanidinium cation, the product was filtered via vacuum filtration to rid the reaction of NaCl biproduct. Dimethyl Iso/Terephthalate (6mmol eq) was dissolved in 50mL of DMF and was added to the reaction and refluxed under nitrogen atmosphere at 60˚C. The reaction was carried out for 24 hours. The solvent was evaporated via rotary evaporation and the product was obtained via vacuum filtration. The solid cation was dried under high vacuum at 80˚C for 48 hours.

N1,N3-dicarbamimidoylisophthalamide

A fine white crystal was obtained after filtration.^{1}H NMR (DMSO) δ 7.16 (b, 4, NH₂); δ 7.36 (t, 1, CH); δ 7.95 (d, 2, CH); δ 8.48 (s, 2, NH); δ 8.75 (t, 1, CH). ESI MS: 249.09.
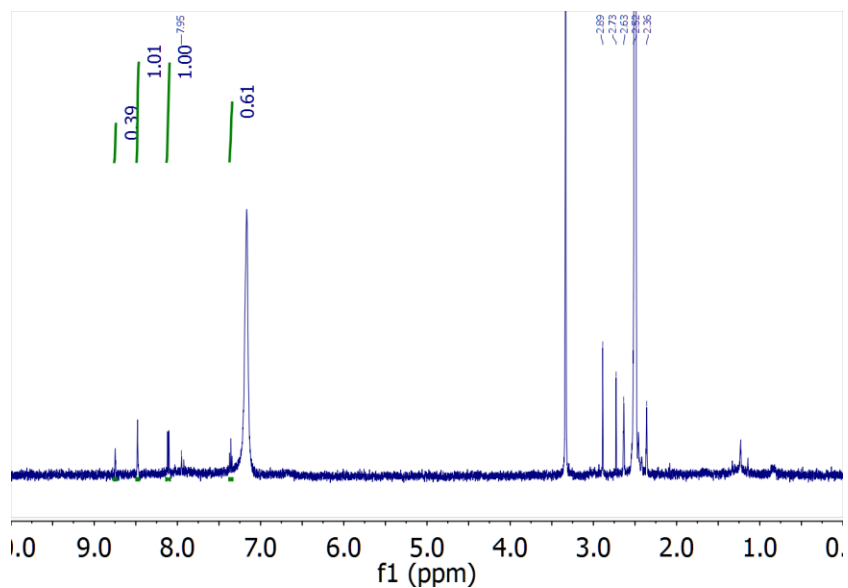
Figure 5.7 ^{1}H NMR spectrum of N1,N3-dicarbamimidoylisophthalamide.

N1,N4-dicarbamimidoylterephthalamide

A fine white crystal was obtained after filtration.^{1}H NMR (DMSO): δ 2.98 (s, 2, NH), δ 6.9-7.4 (b, 4, NH₂), δ 8.0 (d, 4, CH), δ 8.44 (s, 2, NH). ESI MS: 249.09.
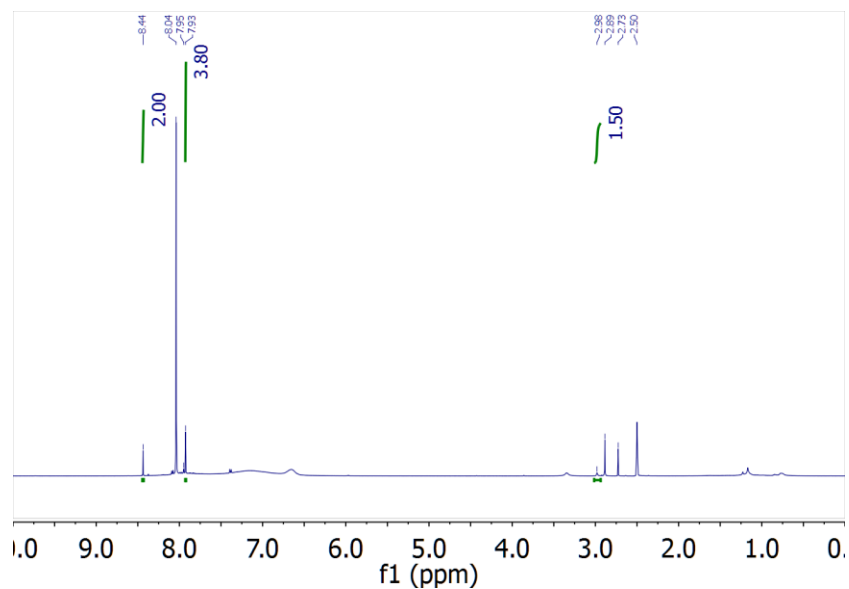

Figure 5.8 ^{1}H NMR spectrum of N1,N4-dicarbamimidoylterephthalamide.

Synthesis of Biguanidinium Iso/Terephthalate Ionic Rubber

Biguanidinium Iso/Terephthalate salt was dissolved in methanol and added to an anion exchange column (Dowex® Monosphere® 550A UPW type 1 strong base anion exchange resin, preliminary elution and wash was carried out using methanol). To maximize the conversion of the chloride anion into hydroxide anion, the column was run carefully and the eluent was protected under argon atmosphere. The eluent was reacted directly (*in situ*) with X31-CTBN in chloroform at room temperature (~21˚C). After completion of the anion exchange column, the solution was evaporated via rotary evaporator. The sample dried under high vacuum at 80 ˚C for 48h. The materials were obtained at room temperature.

5.8.3 Tensile stress experiment using loading frame

Tensile deformation of samples was accomplished using a bi-directional screw driven rail table, with both grips translating simultaneously in opposite directions, keeping the center of mass of the sample stationary. Honeywell Sensotech load cells with load capacity of 22 N was used to measure force in PMA and PMMA, respectively. For monotonic tensile testing, displacement control was used at stretch rate was 0.30 s^{-1}, 0.20 s^{-1}, 0.15 s^{-1}, 0.10 s^{-1}, 0.075 s^{-1}, 0.050 s^{-1}, 0.025 s^{-1}, 0.01s^{-1}. All components were controlled and coordinated using LabView software.

5.8.4 Self-healing experiment of ionic rubber

Self-healing tests were performed at room temperature (20 ˚C) by first cutting the sample using razor into two halves and bringing cut samples together and press for corresponding healing time. The pressure applied by hands was about 50kPa. For the samples that are tested after corresponding waiting time, the cut samples were kept for the waiting time and then pressed for respective healing time. Some healing tests were performed at elevated temperature (Figure 5.5d), for the healing time, the samples were placed in an oven with dedicated temperature. The healed samples were then tested by loading frame.

5.9 References

(1) Rybtchinski, B. *ACS Nano* **2011**, *5*, 6791–6818.

(2) Cordier, P.; Tournilhac, F.; Soulié-Ziakovic, C.; Leibler, L. *Nature* **2008**, *451*, 977–980.

(3) Chino, K.; Ashiura, M. *Macromolecules* **2001**, *34*, 9201–9204.

(4) Godeau, G.; Navailles, L.; Nallet, F.; Lin, X.; McIntosh, T. J.; Grinstaff, M. W. *Macromolecules* **2012**, *45*, 2509–2513.

(5) Burnworth, M.; Tang, L.; Kumpfer, J. R.; Duncan, A. J.; Beyer, F. L.; Fiore, G. L.; Rowan, S. J.; Weder, C. *Nature* **2011**, *472*, 334–337.

(6) Chen, Y.; Kushner, A. M.; Williams, G. A.; Guan, Z. *Nat. Mater.* **2012**, *4*, 467–472.

(7) Hettige, J. J.; Araque, J. C.; Margulis, C. J. *J. Phys. Chem. B* **2014**, *118*, 12706–12716.

(8) Lange, J.; Ekel, R.; John, N. A. S.; George, G. A. *In Structure and Properties of Glassy Polymers* **1999**, 258-271.

(9) Gao, G.; Karaaslan, M. a.; Kadla, J. F. *Macromol. Mater. Eng.* **2014**, n/a – n/a.

(10) Yoshida, M. *Chem. Rec.* **2010**, *10*, 230–242.

(11) Chen, W.; Sauer, J. a.; Hara, M. *Polymer (Guildf).* **2003**, *44*, 7729–7738.

(12) Aboudzadeh, M. A.; Muñoz, M. E.; Santamaría, A.; Fernández-Berridi, M. J.; Irusta, L.; Mecerreyes, D. *Macromolecules* **2012**, *45*, 7599–7606.

(13) Yang, K.; Tyagi, M.; Moore, J. S.; Zhang, Y. *J. Am. Chem. Soc.* **2014**, *136*, 1268–1271.

(14) Tsuzuki, S.; Tokuda, H.; Hayamizu, K.; Watanabe, M. *J. Phys. Chem. B* **2005**, *109*, 16474–16481.

(15) Schlund, S. Quantifying Non-covalent Interactions – Rational in-silico Design of Guanidinium-based Carboxylate Receptors, Julius-Maximilians-Universität Würzburg, 2007.

(16) Sapse, A. M.; Russell, C. S. *Int. J. Quantum Chem.* **1984**, *26*, 91–99.